**NTNU – Trondheim**
Norwegian University of
Science and Technology

# HISC in Super Duplex Stainless Steels

A study of the relation between
microstructure and susceptibility to hydrogen
induced stress cracking

Kjetil Andersen

Chemical Engineering and Biotechnology
Submission date: June 2013
Supervisor: Jarle Hjelen, IMTE
Co-supervisor: Roy Johnsen, IPM
Per Giltvedt, Aker Solutions
Jim Stian Olsen, Aker Solutions

Norwegian University of Science and Technology
Department of Materials Science and Engineering

# Preface

The present thesis is submitted to the Norwegian University of Science and Technology as part of the requirements of the Master's degree programme Chemical Engineering and Biotechnology at the Department of Materials Science and Engineering. Professor Jarle Hjelen and Professor Roy Johnsen have supervised the work together with Ph.D. Jim Stian Olsen and Chief Engineer Per Giltvedt at Aker Solutions ASA.

I would like to express my gratitude to all my supervisors for their efforts in guiding me during this work. Professor Roy Johnsen has shared his experience with HISC testing and given great feedback throughout the semester. Professor Jarle Hjelen has taught me a lot regarding SEM operation and microstructural analysis with EBSD. Ph.D Jim Stian Olsen and Per Giltvedt initiated this project last year and gave me the opportunity to work with the exciting field of HISC. The knowledge that the results are usable in practice has been a great motivational factor. Thank you all for many interesting and useful discussions.

I would also like to acknowledge the help I have received from the staff at SINTEF Materials and Chemistry. I would like to thank Nils-Inge J. Nilsen for helping me with many practical challenges in the laboratory and Ann-Karin Kvernbråten for making the hydrogen measurements for the present thesis.

Finally, I would like to thank all my great co-students for making these past 5 years wonderful and memorable.

**Declaration**

*I hereby declare that the present thesis is a product of own work which has been executed independently and in accordance with the rules and regulations of the Norwegian University of Science and Technology.*

Kjetil Andersen
June 12. 2013, Trondheim

# Abstract

Testing of susceptibility to hydrogen induced stress cracking (HISC) in two 25% Cr Super Duplex Stainless Steels (SDSS) has been carried out. These were a forged material and a hot isostatically pressed (HIP) material with austenite spacing 51.5 $\mu$m and 12.9 $\mu$m, respectively. The tests were carried out on both smooth and notched samples by stepwise increasing load in Cortest proof rings on hydrogen pre-charged samples until fracture. The fracture surfaces were examined in scanning electron microscopes (SEM) and the hydrogen contents were measured. The microstructures of the materials were examined with the electron backscattered diffraction technique (EBSD) and assessed in relation to the results from the HISC testing.

The results indicated that both SDSS materials are prone to HISC and that the HIP material has a higher threshold for HISC. The fracture surface on samples of both materials showed features indicating reduced ductility from HISC. The HIP samples indicated ductile fracture in the centre, implying that hydrogen influence was primarily in close proximity of the sample surfaces. This observation, and considerably higher hydrogen content measured in the forged material, indicates slower hydrogen diffusion in the HIP material than in the forged material.

The results obtained were discussed against the literature reviewed and compared to the requirements in DNV-RP-F112. Indication of low temperature creep was observed on smooth samples by relaxation of the load determining ring deflection. The results from smooth samples indicated a threshold for HISC fracture (after one day of low temperature creep) at 112.6% $\pm$ 3.9% of yield strength (YS) and 104.8% $\pm$ 3.1% for HIP and forged material, respectively. No ring relaxation occurred for the notched samples. Therefore the results from these samples indicated higher threshold for HISC than the smooth samples, namely at 117.1% $\pm$ 2.2% and 113.8% $\pm$ 2.2% of YS for HIP and forged samples, respectively.

# Sammendrag

Tester for følsomhet for hydrogen-indusert spenningsprekking (HISC) av to 25% Cr Super Duplex rustfrie stål (SDSS) er utført. Et smidd materiale og et "Hot Isostatically Pressed" (HIP) materiale med austenitt avstand ("austenite spacing") på henholdsvis 51.5 $\mu$m og 12.9 $\mu$m ble undersøkt. Testingen ble utført ved stegvis økende last til brudd i Cortest testringer av både glatte og kjervede prøver etter forhåndsoppladning med hydrogen. Bruddflatene ble undersøkt i scanning elektron mikroskop (SEM) og hydrogenmålinger ble gjennomført. Materialenes mikrostruktur ble analysert ved bruk av EBSD (teknikk basert på diffraksjon av tilbakespredte elektroner i SEM) og vurdert i forhold til HISC resultatene.

Resultatene indikerte at begge SDSS materialene er utsatt for HISC, men at HIP materialet har en høyere terskel enn det smidde materialet. Bruddflatene indikerte redusert duktilitet på prøvene av begge materialer. HIP prøvene viste tegn til duktilitet sentrert på bruddflaten som indikerer at hydrogenet hadde hovedsaklig påvirket materialet nære overflaten. Disse observasjonene, samt betydelig lavere hydrogeninnhold i HIP materialet, indikerer saktere hydrogendiffusjon i HIP materialet enn i det smidde materialet.

HISC resultatene er diskutert i forhold til litteratur og DNV-RP-F112. På de glatte prøvene ble indikasjoner av siging ved romtemperatur observert ved at den lastbestemmende sammentrykningen i ringene ga etter for oppspenninger ved høy last. For glatte prøver indikerte resultatene terskel for HISC etter en dags siging ved 112.6% $\pm$ 3.9% og 104.8% $\pm$ 3.1% av flytespenning for henholdsvis HIP og smidd materiale. De kjervede prøvene indikerte høyere terksel for HISC tilsvarende 117.1% $\pm$ 2.2% og 113.8% $\pm$ 2.2% av flytespenning for henholdsvis HIP og smidd materiale ettersom siging ikke ble observert her.

# Contents

# Acronyms

**Ag/AgCl** Silver/Silver Chloride reference electrode

**BCC** Body-Centered Cubic

**CI** Confidence Index

**CP** Cathodic Protection

**Cr** Chromium

**CTOD** Crack Tip Opening Displacement

**DNV** Det Norske Veritaes

**DSS** 22% Cr Duplex Stainless Steel

**EBSD** Electron Backscattered Diffreaction

**FCC** Face-Centered Cubic

**FE** Finite Element

**HAZ** Heat Affected Zone

**HEDE** Hydrogen Enhanced Decohesion

**HELP** Hydrogen Enhanced Local Plasticity

**HIP** Hot Isostatically Pressed

**HISC** Hydrogen Induced Stress Cracking

**IPF** Inverse Pole Figure

**IQ** Image Quality

**Mo** Molebdenum

**NACE** National Association of Corrosion Engineers

**Ni** Nickel

**SD** Standard Deviation

**SDSS** 25% Cr Super Duplex Stainless Steel

**SENB** Single Edge Notched Bend

**SEM** Scanning Electron Microscope

**RA** Reduction in Area

**RT** Room Temperature

**RP** Recommended Practice

**SIMR** Swedish Institute for Materials Research

**SMYS** Specified Minimum Yield Strength, typically 450 MPa for DSS and 550 MPa for SDSS[1]

**SCE** Saturated Calomel reference electrode

**SSRT** Slow Strain Rate Testing

**TWI** The Welding Institute

**UTS** (Ultimate) Tensile Strength

**YS** Yield Strength, similar to 0.2% offset proof stress

**WA** Workshop Agreement

# Chapter 1

# Introduction

## 1.1 Historical background

Super Duplex Stainless Steels (SDSS) are materials which comprise an extraordinary combination of mechanical properties, corrosion resistance and relatively low cost. Due to these features, the subsea industry has found use for it in many applications. There have, however, been incidents of cracking of components made from these materials[2]. In service, the SDSS components are exposed to the cathodic protection (CP) system of the subsea installation. This leads to hydrogen evolution on the steel surface which can diffuse into the component. The hydrogen reduces the strength and ductility of the materials and makes them prone to brittle cracking when too high loads are applied. This process in known as hydrogen induced stress cracking (HISC). HISC in SDSS is by now (2013) a well-known challenge for the subsea industry and decades of research has resulted in design guidelines like DNV Recommended Practice F112 (DNV-RP-F112). The guideline is the present day industry solution to avoid HISC in SDSS as it gives instructions on amount of allowable load applied to SDSS components exposed to CP[3].

## 1.2 Motivation

The susceptibility of SDSS materials to HISC is influenced by various aspects both related to environment and material quality. The latter has been shown to be closely related to microstructure inherent from production method[4]. DNV-RP-F112 therefore distinguish between fine and coarse grained material based on whether the austenite spacing is less or more than 30 $\mu$m, respectively. Hot isostatically pressed (HIP) material falls into the category of fine grained material. HIP material typically has austenite spacing far less than 30 $\mu$m, and studies have shown that HIP material is far more resistant to HISC than materials with coarser microstructure[5, 6]. This resistance have by some been suggested

as high enough for the risk for HISC to be negligible[7]. The current version of DNV-RP-F112 was issued in 2008 and the requirements in it were assumed to be conservative[3]. The industry has therefore encouraged further work on this matter.

## 1.3 Aim of this work

The primary goal of this work is to determine the relative susceptibility of HIP and forged SDSS to HISC. The test method used in this context can also give indications to threshold values against HISC for the materials. It is known that microstructure has an influence on HISC susceptibility and therefore an analysis of the microstructure of the materials is to be carried out by means of the electron backscattered diffraction (EBSD) technique. After fracture, both fracture surface analysis in a scanning electron microscope (SEM) and hydrogen measurements are to be carried out. These different parts are all related to the primary goal stated above and should give clear indications to HISC susceptibility.

# Chapter 2

# Theoretical background

There are three factors which have to be in place in order to get hydrogen-induced stress cracking (HISC). These are hydrogen, stress and susceptible material, as illustrated in figure 2.0.1 [8]. The first three sections in this chapter aims to explain how these three factors appear in reality and how they interact to cause detrimental effects. Next, the literature studied as background for this work is reviewed with focus on possible influences on HISC and the following ways to avoid it. Finally, the different methods of microstructural analysis employed in this work is explained.

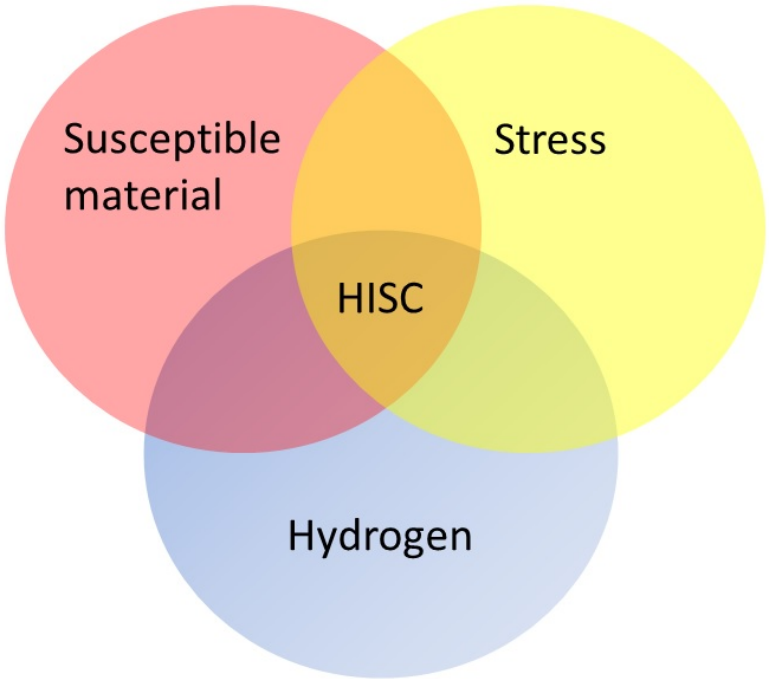


**Figure 2.0.1:** The figure illustrates the three factors which constitute HISC.

## 2.1 Hydrogen source

There are different sources of hydrogen, including general corrosion and unintended galvanic corrosion. The main sources are from the cathodic protection (CP) system on the surface and from welding. The hydrogen source relevant for the current discussion is CP systems. This section aims to explain how hydrogen is developed on the metal surface from the CP, including the electrochemistry behind the phenomenon[9, 10].

### 2.1.1 The electrochemistry of corrosion

The starting point in explaining hydrogen evolution on steel surface is the electrochemical reactions which constitute corrosion. Unlike other chemical reactions, electrochemical reactions involve a transfer of electric charge by electrons. Corrosion can always be split into two parts. These are a reduction reaction where a negative charge is gained, and an oxidation reaction where the species loose a negative charge. When the half-cell reactions are combined the overall reaction appears, where the charge loss and -gain have cancelled each other out. This is illustrated below with oxidation-, reduction- and overall reaction in equations 2.1a, 2.1b and 2.1c, respectively. Here, M is an arbitrary metal and n is the number of electrons ($e^-$) transferred[11].

$$M \rightarrow ne^- \qquad +M^{n+} \tag{2.1a}$$

$$nH^+ + \quad ne^- \rightarrow nH_{2(g)} \tag{2.1b}$$

$$nH^+ + \quad M \rightarrow nH_{2(g)} \quad +M^{n+} \tag{2.1c}$$

The equations above make out the corrosion of a single metal. As these are electrochemical reactions, there will be a range of electrochemical potentials at which the thermodynamic parameters enable the half-cell reactions to take place. These are represented in an Evans diagram, shown to the left in figure 2.1.1 with a red line representing the oxidation of metal and a blue for hydrogen evolution. This kind of diagram shows the range of potentials (E) where the half-cell reactions are possible at and what rate they will occur at, measured in current (I). The intersection of the red line (oxidation) and the blue line (reduction) gives the corrosion potential ($E_{corr}$) and rate of corrosion($I_{corr}$)[11].
The situation changes when two dissimilar metals are in electric contact as one will be more noble (i.e. higher corrosion potential, metal M in figure 2.1.1) and the other will be less noble (active metal N). Assuming only one oxidation- and one reduction reaction per metal, we now have four half-cell reactions. The governing laws of electrochemistry dictate that the potential will stabilise at an $E_{couple}$ where the total rate of oxidation equal the total rate of reduction. This is graphically represented to the right in figure 2.1.1.

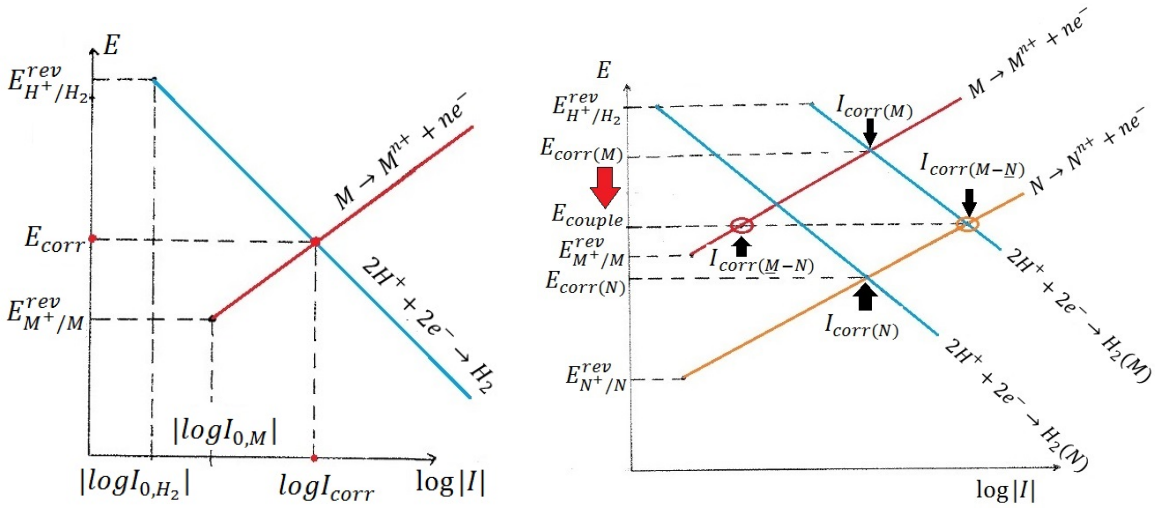


**Figure 2.1.1:** Evans diagrams from [11] and modified. The diagram to the left for corrosion of single metal (M), with oxidation as red line and reduction as blue line. The diagram to the right shows galvanic corrosion with oxidation of noble metal (M) as red line and of active metal (N) as orange line. The red arrow implies the drop in potential from corrosion potential of M to the coupling potential.

When the potential is lowered from $E_{corr(M)}$ to $E_{couple}$ (shown by a red arrow in figure 2.1.1), the rate of corrosion of M is reduced to the level indicated by the red circle in the figure. The opposite happens for the active metal (N) and the rate of corrosion increases to the level indicated with an orange circle in the figure. This type of corrosion is known as galvanic corrosion, and can have detrimental effects when not intended[11].

### 2.1.2 Cathodic Protection

Cathodic protection (CP) utilize the effect galvanic corrosion has on the more noble metal. If the active metal has a low enough potential, $E_{couple}$ will be low enough to obliterate the corrosion of M. This process is also called cathodic polarization. Since the corrosion rate of the active metal will increase in order to reduce the corrosion of the more noble metal, it is often referred to as sacrificial anode in the CP system. As already stated, the oxidation- and reduction reaction(s) have to occur at the same rate and in the case of reduction of hydrogen, this will be produced on the surface of both metals. As shown in figure 2.1.1 the hydrogen evolution will be higher on the more noble metal - which in the case relevant for the current discussion would be the steel surface[11, 8].
Cathodic protection is used as protection against corrosion on the surfaces exposed to seawater on subsea installations. Aluminium and zinc alloys are less noble than steels and are therefore commonly used as sacrificial anodes. A potential of -800 $mV_{Ag/AgCl}$ is generally accepted as protective of carbon- and low-alloy steels[12]. The cathodic

polarization varies depending on distance from anodes and anode material. For design purposes the potential is about -1050 $mV_{Ag/AgCl}$ and -1030 $mV_{Ag/AgCl}$ in seawater for aluminium and zinc anodes, respectively[13], but can range between -800 $mV_{Ag/AgCl}$ and -1100 $mV_{Ag/AgCl}$.

### 2.1.3 Hydrogen formation

Equation 2.1b is an example and a simplification of the reduction reaction on the metal surface. Hydrogen can be formed from CP by the two reactions as shown in equations 2.2a and 2.2b, depending on environment. In these equations □ represent an available site on the surface and $H_{ads}$ is an atomic hydrogen which is adsorped. The $H_{ads}$ has not yet diffused into the atomic lattice, but that is one of the alternatives and can be written as equation 2.2c. Otherwise it will form gaseous hydrogen and leave the surface as shown in equations 2.2d and 2.2e[10].

$$H_2O + e^- + \square \leftrightarrow H_{ads} + OH^- \tag{2.2a}$$

$$H^+_{aq} + e^- + \square \leftrightarrow H_{ads} \tag{2.2b}$$

$$H_{ads} \rightarrow H_{abs} \tag{2.2c}$$

$$H^+ + e^- + H_{ads} \leftrightarrow H_2 + \square \tag{2.2d}$$

$$H_2O + e^- + H_{ads} \leftrightarrow H_2 + OH^- + \square \tag{2.2e}$$

The detrimental effects that can follow from hydrogen absorped into the atomic lattice is reviewed in section on HISC mechanisms.

## 2.2 Super Duplex Stainless Steels

Duplex Stainless Steels and Super Duplex Stainless steels are highly alloyed steels which were developed to combine high corrosion resistance, strength and toughness to a reasonable cost. Duplex Stainless Steels have 22% Cr, but is often cited to include the higher alloyd 25% Cr Super Dupex Stainless Steels. Throughout this report, the term Duplex Stainless Steel (DSS) is used for 22% Cr steels alone (typical UNS grades S31803 and S32205) while Super Duplex Stainless Steels (SDSS) is used for the 25% Cr steels (typical UNS grades S32550, S32505, S32750 and S32760)[1, 14, 3].

### 2.2.1 Metallurgy

Both DSS and SDSS have a two-phased microstructure consisting of approximately equal amounts of austenite islands ($\gamma$) embedded in a ferritic ($\alpha$) matrix. The distribution of the two phases should be as close to 50/50 as possible to achieve better corrosion- and mechanical properties. Both chemical composition and heat treatment is critical in order to obtain and maintain this microstructure. Welding is therefore especially challenging. As implied above, a large fraction of Chromium (Cr) is added to these alloys. In addition, Nickel (Ni) and Molebdenum (Mo) have critical purposes. In pure iron, only ferrite is a stable phase at room temperature and the austenite is stable at an interval of higher temperatures. Alloying elements have different solubility in the phases and can function as stabilizer of a phase. By adding austenite stabilizing elements like Nickel and Manganese, the austenite region is displaced and opened to lower temperatures. By adding enough of these elements, the austenite phase can be completely or partially preserved down to room temperature. Other elements, like Cr and Mo, stabilize the ferrite phase and act in the opposite way by narrowing the area where austenite is formed. The effect of Cr is altered by the presence of Ni and actually make it easier to preserve austenite down to room temperature. The microstructures possible by adding $\gamma$- and $\alpha$-stabilizers can be summarized with the elements' relative influence, given as Ni-equivalent and Cr-equivalent, in a Scheaffler diagram as seen in figure 2.2.1.

Cr, Mo and Ni have other purposes than influencing the microstructure. Chromium is added to make steels "stainless" in amounts of at least 12%. Cr causes a self healing passive oxide layer to appear on the steel surface in the presence of oxygen. Molybdenum increases the corrosion resistance by easing the formation of the passive layer and toughening it. Nickel also increase corrosion resistance in many acidic environments and makes the oxide layer re-passivate more easily[15, 16].

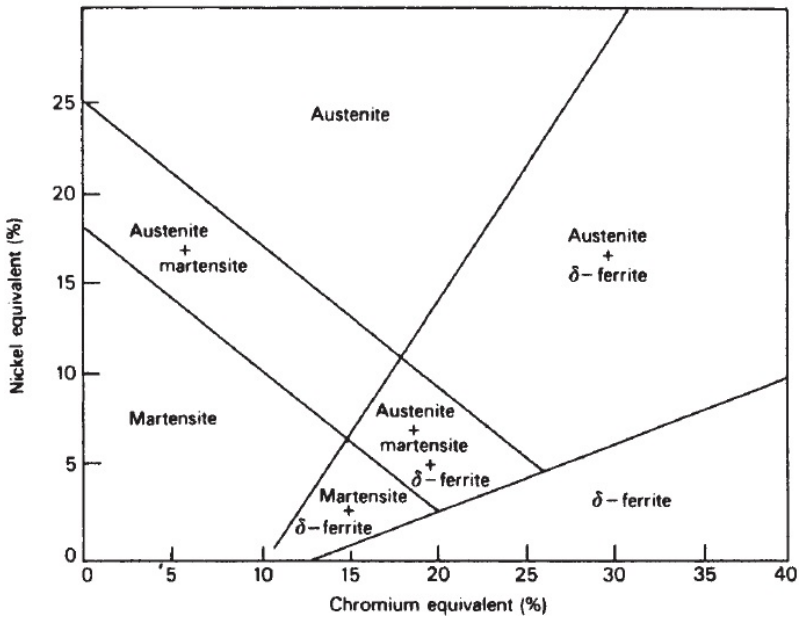


**Figure 2.2.1:** Image from [16] showing the microstructures achievable for steels with Cr-equivalent and/or Ni-equivalent elements in a Schaeffler diagram.

The combination of phases are important for the present study. The ferrite phase has a body-centred cubic (BCC) structure which is less closely packed than the ausitenite phase, which has a face-centred cubic (FCC) structure. Interestingly, the more closely packed austenite phase (FCC) has larger holes in the structure than the ferritic BCC structure. These features have implications for hydrogen diffusion and solubility. The diffusion rate of hydrogen is much faster in ferrite compared to austenite, while the solubility of hydrogen is higher in austenite[16, 14, 17].

### 2.2.2 Production methods

There are various production methods for components made from SDSS. Cast material without further processing show unfavourable microstructural features which yield poor mechanical properties. Also, the special two-phase microstructure of DSS and SDSS makes the program for heat treatment critical. Most conventional methods involve processing of cast material such as to bar stock or extrusion to tubes. The production method (along with chemical content) determine the microstructure of the finished product. Through the different steps of the process one can achieve smaller grain size, which is highly favourable. The differences that can be obtained in different bars by only varying the diameter is shown in figure 2.2.2. Due to the Hall-Petch effect metals will get increased yield strength and toughness with smaller grains. Other properties such as ductility and ductile-to-brittle transition temperature is also known to improve for many materials. Another notable aspect of production method that is the isotropy or anisotropy

that follows. The effect production has on isotropy is also easily seen in figure 2.2.2. In the literature reviewed for the present work, it is also clear that production method and microstructure of SDSS has implications for the susceptibility to HISC.[15, 18]

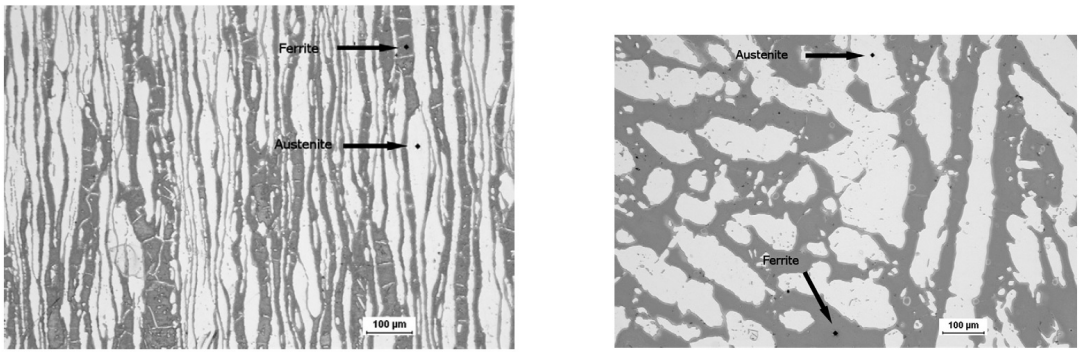


**Figure 2.2.2:** Images from [19] showing the microstructure of a small diameter bar to the left and from a large diameter bar to the right.

Hot isostatic pressing (HIP) is a newer production method for metal components. In the process, metal powder is hot isostatically pressed (HIP'ed) in the solid state to fully dense components. The HIP technique is used both for brazing and cladding or to production of near net shape components. The advantages of HIP material over forgings includes reduction in welding and machining and superior mechanical properties[20, 21].

## 2.3 HISC in SDSS

There are various materials prone to HISC such as untempered marteniste and, relevant for this project, Duplex- and Super Duplex Stainless Steels. On the large scale HISC is recognised by reduction of ductility and brittle cracking. The mechanism behind the change from ductile to brittle behaviour is subject for discussion and research. These matters are the focus in this section, which will consider HISC fracture in SDSS solely.

### 2.3.1 Deformation and fracture

Deformation of metals are generally categorised as elastic and plastic (inelastic). Elastic deformation is reversible and is, on the atomic level, stretching of the crystal lattice. This happens at stresses up to a certain level, the yield stress (often occurs at strain about 0.5%), where the deformation becomes plastic and permanent. Plastic deformation is for metals movement of dislocation through the atomic structure[18]. It has been shown that HISC cracks often starts in the ferrite phase and that the austenite phase in many cases acts as a crack stopper. This effect has been seen by post fracture analysis, as shown in figure 2.3.1[19, 22, 6].

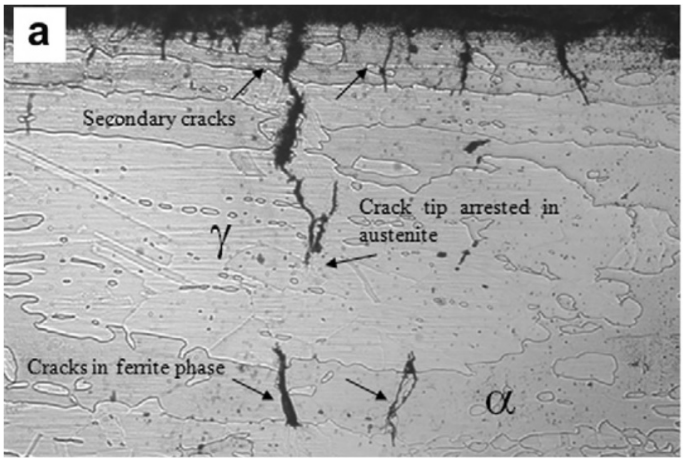


**Figure 2.3.1:** Optical micrograph from [22] showing cracks due to hydrogen embrittlement arrested in austenite phase and propagation in the ferrite.

Plasticity is central in relation to fracture mode. The difference between brittle and ductile fracture can be seen on fracture surfaces, as well as in mechanical properties. There are three general fracture mechanisms in metals; cleavage fracture, intergranular fracture and ductile fracture. The latter represents fracture with a high degree of plasticity, where necking occurs when ultimate tensile strength (UTS) is exceeded. Here, fracture happens by void nucleation, growth and finally coalescence. These voids are visible on the fracture surface and gives it a characteristic dimpled structure as seen in figure 2.3.2. A common

macroscopic feature in ductile fractures is cup-and-cone surfaces. This feature comes when a triaxial stress state is produced in the center of the specimen during necking. This promotes voids which upon coalescence gives a penny-shaped flaw in the middle. The outer ring is exposed to lower hydrostatic stress and has fewer voids before the centre flaw appears. Afterwards, deformation bands are produced in the 45° angles from tensile direction and numerous smaller voids form and cause final fracture. The fractured surfaces therefore appear with one surface shaped as a cup and the other as a cone[23].

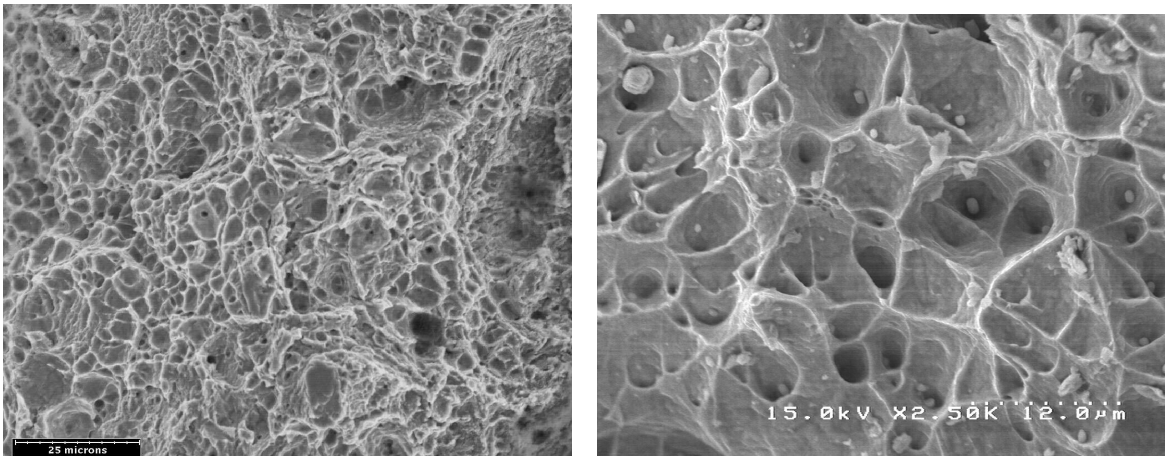


**Figure 2.3.2:** Images from [24, 25] showing dimpled surfaces after ductile fracture in a metal.

Both cleavage fracture and intergranular fracture are types of brittle fracture. With cleavage fracture the crack propagates through the grains. The crack follow the direction of most favourable orientation in the grain and therefore changes direction each time a grain boundary is crossed. This type of fracture is typically seen in HISC cracks with cleavage through the ferrite phase. The fracture is recognised by a multifaceted surface, where each facet correspond to a grain. Also, so-called "river patterns" is commonly observed on each facet, indicating point of fracture origin in the grain. Both these features are observed in the image to the right in figure 2.3.3[3, 23].

Intergranular fracture is, as the name implies, crack propagation along the grain boundaries. This fracture mechanism is less common and happens when the grain boundaries are more favourable for crack growth than transgranular cleavage. It is included here because environmentally assisted cracking is one of the situations at which intergranular fracture can occur. On the fracture surface it is often possible to see the grains along the path of the fracture as seen in the image to the left in figure 2.3.3[23].

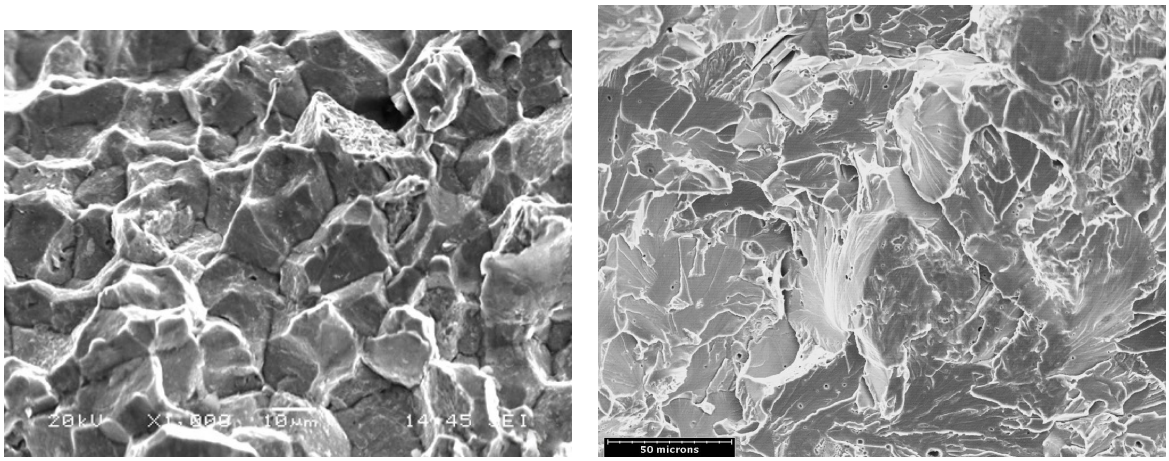


**Figure 2.3.3:** Images from [26] showing intergranular fracture to the left and cleavage fracture to the right.

In a publication by Olden et. al. [27] it was stated that transgranular cleavage in the ferrite and ductile tearing of the austenite are typical features on fracture surfaces from HISC fracture in duplex stainless steel. It was also pointed out that secondary cracking indicates stepwise cracking. The images in figure 2.3.4 are from the publication where the mixture of the fracture modes can be seen to the left and secondary cracks to the right.

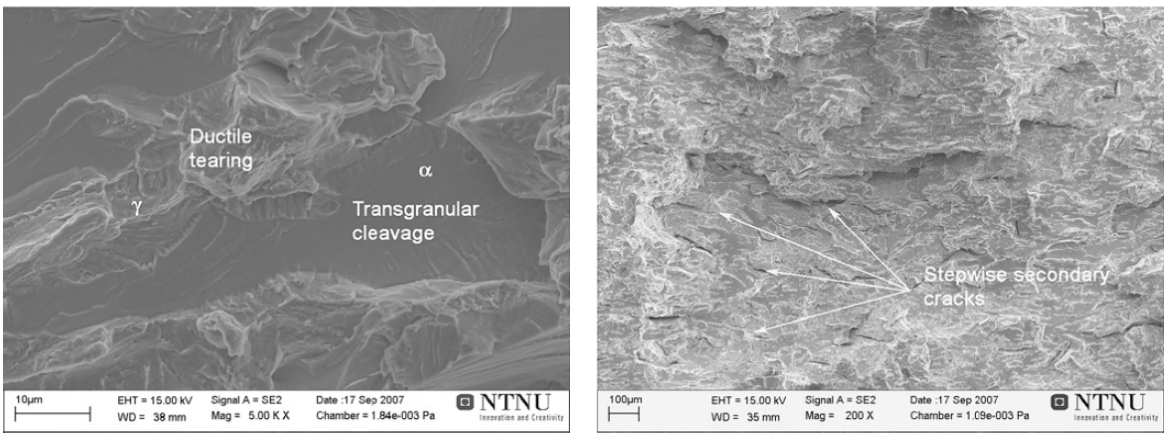


**Figure 2.3.4:** Images from [27] showing the fracture surfaces from HISC testing on SDSS with mixture of fracture modes and secondary cracks.

### 2.3.2 Hydrogen in SDSS

Because of the microstructure of SDSS, the diffusion of hydrogen is $10^4$ to $10^5$ times slower in austenite than in ferrite. This implies that the diffusion in SDSS manly takes place in ferrite phase, even though the diffusion in ferrite in SDSS is considerably slower

than in plain ferrite steel. This is due to tortuous diffusion paths caused by austenite islands which make the paths longer and also create trap sites for the hydrogen along the way. Trapping reduces the amount of diffusible hydrogen and slows down the overall diffusion rate. The microstructure therefore has consequences for hydrogen diffusion as both diffusion length and trapping is influenced by the shape and size of the austenite islands. By this theory, fine, dispersed, austenite islands would result in slower overall diffusion than coarse structure with larger gaps between the austenite islands. The solubility of hydrogen is about 1000 times greater for austenite than for ferrite. The austenite can therefore have a high hydrogen content without the crack resistance being reduced appreciably. The ferrite phase can resolve very little hydrogen and seldom contains more than 10 ppm hydrogen, but even at very low hydrogen content ferrite is prone to brittle cracking. Since cracking initiates at the surface and in the ferrite phase, whether this value should be employed as input variable for hydrogen level at outer surface for modelling has been discussed in literature[28]. In the publication, 40 ppm was employed, while another publication used 30 ppm.[9, 27] As seen in figure 2.3.1 a microcrack at the surface may not be a critical event as it can be arrested in the austenite. On the other hand, a process of stepwise cracking until final fracture must also be considered. From the field of fracture mechanics it is known that a crack subjected to plane opening stress yields a local stress and strain field ahead of the crack tip as seen in figure 2.3.5. The figure shows that the stress reaches a maximum a distance ahead of the crack tip. Because of dilation of the lattice, hydrogen will diffuse to the the cites of increased hydrostatic stress. From finite element (FE) modelling the resulting effect is seen in figure 2.3.5 where the hydrogen concentration ahead of a crack tip is depicted over time[9, 28].

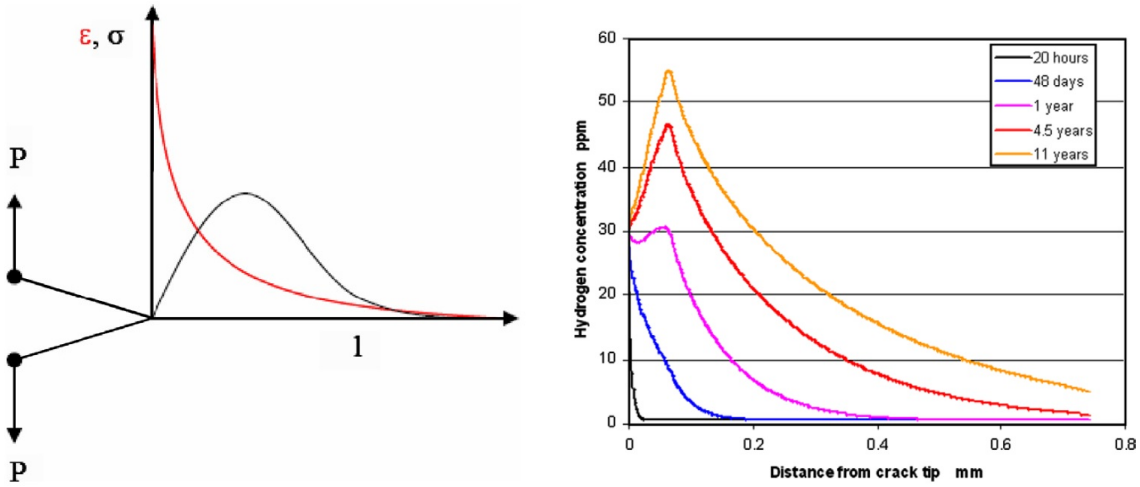


**Figure 2.3.5:** Graphics from [9] showing the stress($\sigma$)- and strain($\epsilon$) field ahead of a crack tip to the left and the resulting increase of hydrogen concentration over time to the right.

The input variables behind the results shown to the right in figure 2.3.5 was a surface hydrogen concentration of 30 ppm and a temperature of 4 $^{\circ}\mathrm{C}$. The situation changes if the bulk material is pre-charged with hydrogen[28], as the bulk concentration would rise. The diffusion coefficient can be described by the Arrhenius equation, given in equation 2.3. Here, $E_A$ is the activation energy, R is the gas constant and T is temperature. From the relation it is clear the higher temperature give larger diffusion coefficient, which in turn yields faster diffusion[9].

$$D = D_0 \cdot exp(-E_A/RT) \tag{2.3}$$

### 2.3.3 HISC fracture mechanism

There are several theories on the mechanism of HISC. Two of the most cited ones are called hydrogen-enhanced decohesion and hydrogen-enhanced localized plasticity. Both models involve a local accumulation of hydrogen in a stressed area, but imply that hydrogen influences the possible deformation mechanisms in different ways[9].
Hydrogen-enhanced decohesion (HEDE) is one of the oldest models to describe embrittlement in metals due to atomic hydrogen. The interstitial hydrogen cause dilatation of the atomic lattice. This lowers the cohesive strength and thereby lowers the energy barrier for cracking. In this way the barrier for for either cleavage plane or grain boundary decohesion decreases.
Hydrogen-enhanced local plasticity (HELP) implies that the movement of dislocations is eased by the presence of atomic hydrogen. The movement of dislocations compete with obstacles such as stress fields from other dislocations. The hydrogen shield these stress fields and ease the path of the dislocations. This creates a local softening which result in microvoid coalescence along the planes of reduces shear strength. Therefore, the HELP model is said to cause local softening which is seen as embrittlement macroscopically.
The mechanism behind HISC is subject to research in both material testing and mechanical analysis with tools like finite element (FE) modelling. In combining material testing with mechanical analysis, one is able to comment on the validity of the models for the HISC mechanism as done in reference [17]. A fracture mechanics model which completely describes the stress and strain behaviour in the process zone affected by hydrogen has not yet (2009) been recognized[27]. It has also been pointed out in literature that a combination of the two fracture mechanisms could likely be in effect, i.e. HEDE dominates in the ferrite while HELP rules in austenite.[9, 28, 17]

## 2.4 Previous HISC testing

A literature review was completed as background for the experimental work in the present thesis and for comparison of the results obtained. The literature focused on has been in relation to HISC in the same class of materials tested here, namely SDSS from various production methods. The testing reviewed comprises dead-weight testing, slow strain rate testing (SSRT), crack tip opening displacement (CTOD) testing, 4-point bending and incremental constant load. The latter testing method is of highest relevance for the present work.

### 2.4.1 Materials and austenite spacing

The influence production methods have on susceptibility to HISC is closely related to microstructural features such as ferrite content, austenite spacing and grain size. The preference of these features in relation to HISC has been observed to be lower ferrite content, smaller austenite spacing and smaller grain size. In these relations the ranking of production method shown in figure 2.4.1 applies.[5, 3]

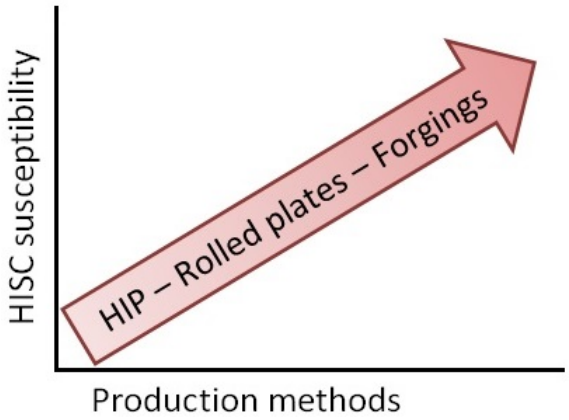


**Figure 2.4.1:** Graphic showing the relation between production method and susceptibility to HISC.[5]

The ranking above is reflected in DNV-RP-F112, where HIP material and rolled plates are categorized as better material quality than forgings[3]. In an article from 2007 it was stated that the risk for HISC is negligible in HIP material because of the uniform fine microstructure[7]. This view on the resistance against HISC for certain SDSS materials has also been stated by others[29].

In the Foinaven investigation, it was found that the cracked forged SDSS hubs exhibited a very large grain size, precipitation of carbo-nitrides and grain orientation through the thickness of the hub. Testing of a pipe material with fine grain size and no carbo-nitrides showed a much higher resistance to cracking under similar environments. Various test

methods were used in the small scale testing, with results as shown in figure 2.4.2. As is shown in the figure, the investigation concluded with that the SDSS material had a threshold strain level of 0.5% total strain. In using this strain threshold, residual strain in the material has to be accounted for in the design process. The Foinaven investigation found a maximum residual strain level of 0.25% on the external surface of the cracked area on the material which had failed before the investigation. An earlier publication had suggested higher resistance to HISC for SDSS material. The low threshold value found in the investigation was therefore evaluated as possibly due to the reduced resistance which follows the grain size and -orientation of the particular hub tested[2].

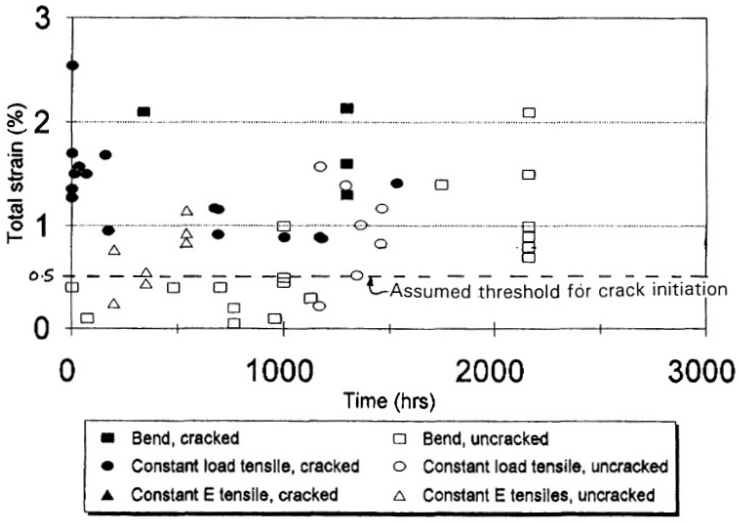


**Figure 2.4.2:** Graph from [2] showing all small scale test results from the publication with an assumed threshold for crack initiation.

In a publication by Kivisäkk, it was mentioned previous HISC testing on SDSS with use of constant load using dead weights. Here, specimens from a large diameter bar passed at 84% of the yield strength (austenite spacing of approx. 42 $\mu$m) while specimens from an extruded tube (austenite spacing of between 9.4 $\mu$m and 16.1 $\mu$m) showed no cracking at 130% of the yield strength [19].

Another study tested materials of quite similar austenite spacing. HIP and forged SDSS (and DSS) with average austenite spacing of 14 $\mu$m and 49 $\mu$m, respectively, were studied by single edge notched bend (SENB) testing for 30 days in HISC favouring environment. It was reported that no cracking was observed for CTOD levels lower than 0.08 mm and only slight cracking at 0.08 mm for HIP materials. The forged SDSS showed significant cracking at CTOD above 0.03 mm and no cracking below CTOD of 0.016 mm[5].

Kivisäkk and Holmquist have previously (publ. 2001) tested DSS and SDSS for HISC both as annealed and 20% cold worked material at 90% of tensile strength. Both constant load and slow strain rate testing (SSRT) were done with samples coupled to Zinc in syn-

thetic seawater at 80 °C. From the constant load tests, no failures were observed after the testing time of 500 hours. The cold worked samples were tested by SSRT and compared to a reference sample which was tested in synthetic seawater at 80 °C, i.e. samples coupled to Zinc vs. uncoupled samples. For the DSS, ratios of elongation between 0.91 and 0.95 were obtained while the SDSS samples achieved ratios of 0.81 and 0.85. No secondary cracks were observed on the cracked samples. In the same publication, reference to two earlier studies are made, one from the Swedish Institute for Metals Research (SIMR) and one from AB Sandvik Steel. The latter reported that UNS S32750 (SDSS) was immune to hydrogen embrittlement, while the study from SIMR reported a very low degree of brittle behaviour with a ratio of about 90% (reference not known). The Kivisäkk and Holmquist study reported that the SDSS material is not immune, but that there is no risk of HISC when the material is not plastically strained during service[29].

A proceeding from the Offshore Mechanics and Arctic Engineering conference in 2004 of Woollin presented results of HISC testing comprising a range of both DSS and SDSS materials including pipe, plate, forging, bar, weld and simulated heat affected zones (HAZ). The small scale testing was done by constant load with dead weights. For all materials tested in this study cracking initiated at stresses between 87% and 104% of the yield stress, while propagation of the cracks happened at normalised stresses between 92% and 138%. These results were correlated to austenite spacing of the materials and were presented graphically as shown in figure 2.4.3. Fine "secondary" austenite between the larger austenite grains was ineffective at blocking propagation of the HISC cracks. From the results in the publication, there was no distinction between DSS and SDSS in terms of susceptibility to HISC[4].

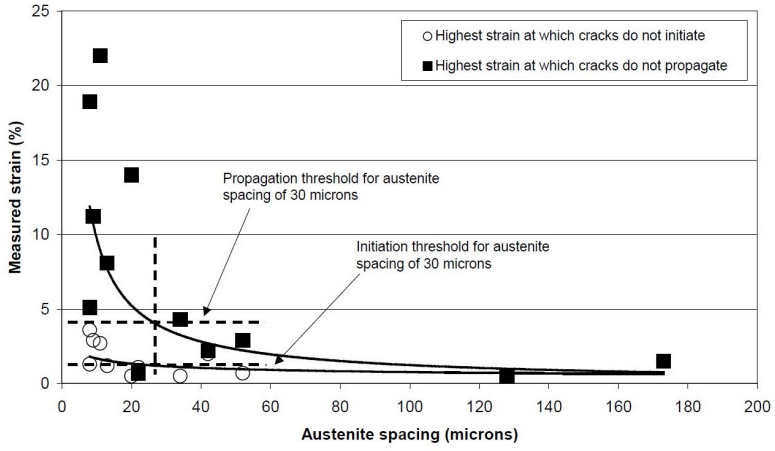


**Figure 2.4.3:** Graph from [4] showing correlation between austenite spacing and threshold for crack initiation and -propagation.

A more resent publication of Lauvstad et. al. [6] focused on the increased resistance

of HIP material against HISC and the effects of various testing parameters. The testing comprised SSRT of forged and HIP SDSS in 3.5% NaCl solution at various temperatures and pressures. The main finding was an improved resistance towards HISC for HIP vs. forged SDSS. The fracture strain ratios achieved from SSRT in 3.5% NaCl at 4 °C with CP potential to SSRT test in air at room temperature were 0.51 and 0.26 for HIP and forged material, respectively. Improved resistance was also seen in pre-charged samples, with ratios of 0.35 and 0.16 for HIP and forged material, respectively.

### 2.4.2 Low temperature creep

Low temperature creep, or cold creep, is time dependant plastic deformation which can happen when materials are subjected to (relatively high) loads over a period of time. This effect is generally associated with high temperature applications, but has been shown to apply during room-temperature testing for SDSS. A study prior to Foinaven estimated that the effects of creep begins to be evident at strains about 0.15%. The effect was shown in the Foinaven investigation report with the deleterious effect that can follow, see figure 2.4.4[2, 19].

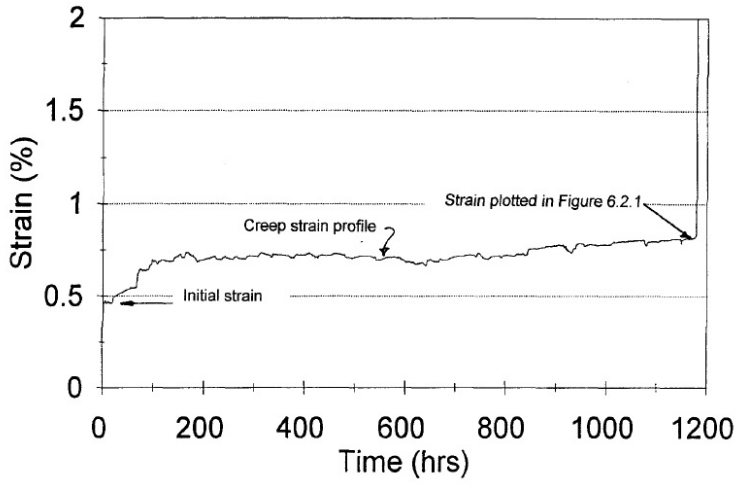


**Figure 2.4.4:** Graph from [2] showing strain profile from a constant load test with development from initial strain to failure.

Kivisäkk did further work on the matter of low temperature creep in 2010. He found a difference in creep behaviour for products with fine and coarse microstructure as the coarser material showed creep at lower load levels than the fine grained material. The testing of material from a bar showed more creep than similar tests of extruded tube material. The study concluded that room temperature creep is needed to promote HISC, but even if creep is present HISC does not necessarily occur[19].

### 2.4.3 Testing parameters

#### Hydrogen content

Since hydrogen is a prerequisite for HISC, related testing involves ways to ensure hydrogen present on the sample surface. The hydrogen concentration in the bulk material, however, depend on numerous factors. The direct effect of hydrogen content was tested by Zakroczymski et al. by SSRT. Different hydrogen contents were achieved by charging the specimens in different solutions. The results showed clear relations between hydrogen content and degree of embrittlement as seen in figure 2.4.5[30].

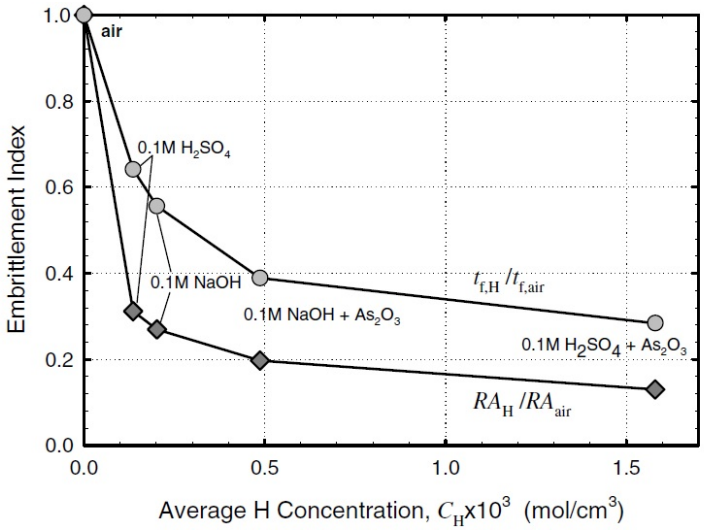


**Figure 2.4.5:** Graph from [30] showing relation between hydrogen content and embrittlement measured as time to failure ratio (during SSRT) and reduction in area ratio(RA).

It is clear from the observations above that ensuring correct hydrogen concentration in samples is important for the HISC testing to correspond to operating conditions. The article demonstrated how different hydrogen contents can be achieved by different testing media. The highest hydrogen content was achieved with $0.1MH_2SO_4$ solution + $As_2O_3$, while testing to correspond to the sub sea environment is typically done by artificial/synthetic seawater or 3.5% NaCl solution[30].

The hydrogen content affects the strength and hardness of the different phases in SDSS. Prasad, Kain and Roychowdhury did testing of microhardness of the phases in relation to hydrogen charging. They found that the ferrite was harder than the austenite before pre-charging, while after pre-charging it was the opposite relation with significantly larger increase in hardness for the austenite phase than the ferrite phase[31].

In the testing of pre-charging by Lauvstad et al. (see section on pre-charging later) it was found that the bulk hydrogen concentration was significantly higher in the forged material than the HIP material after same treatment[6].

### Calcareous deposits

When cathodic protection is applied in seawater, calcareous deposits of $CaCO_3$ and $Mg(OH)_2$ can form on the steel surface depending on applied potential and composition of the seawater. These deposits can have a beneficial effect in terms of reduced current required from the CP system. Ou and Wu[32] found that the hydrogen absorption is also reduced by a barrier effect of the deposits. There has been observed a reduction in hydrogen embrittlement when applied potential decreases from -1000 $mV_{SCE}$ to -1200 $mV_{SCE}$ in artificaial seawater which was attributed influence of calcareous deposits[33]. These effects could give an extra diffusion barrier in the case of damaged/non-existing coating but should not be relied on. To keep the testing parameters conservative and avoid the possible influence of these effects during testing 3.5% NaCl solution can be employed instead of synthetic/artificial seawater.[6]

### Pre-charging

Another aspect of ensuring sufficient amount of hydrogen in the samples during HISC testing is use of pre-charging. There is some dispute in the literature on how effective pre-charging is. Testing by Lauvstad et. al. showed an increased bulk concentration of hydrogen after 30 days pre-charging at room-temperature. Both fracture strain ratio and RA ration were lower for pre-charged samples than as-received samples. All these effects were more pronounced for forged material(18.1 ppm) than the HIP material(11.1 ppm)[6]. Kivisäkk and Holmquist, on the other hand, found no influence of pre-charging on the test results even though the method of pre-charging had earlier been found to yield 80 ppm hydrogen in the samples[29]. Lauvstad et al. pointed out, on the basis of these and other tests of pre-charging, that the charging conditions of the subsequent testing may be important for the significance of the pre-charging.

### Cathodic polarization

The shift in potential is normally to about $-1000mV_{SCE}$ [1] to $-1100mV_{SCE}$[29, 4]. The testing done by TWI in [4] showed a trend of higher threshold for cracking with less negative potentials, see figure 2.4.6. The article reported that no cracks were formed at $-700mV_{SCE}$ and only a few at $-800mV_{SCE}$ when approaching UTS. The graph show clear increased susceptibility to cracking at $-900mV_{SCE}$ and lower.

[1] SCE and Ag/AgCl are types of reference electrodes which give potentials which are virtually equivalent ($mV_{SCE} \approx mV_{Ag/AgCl} + 20mV$ [34]) [12].

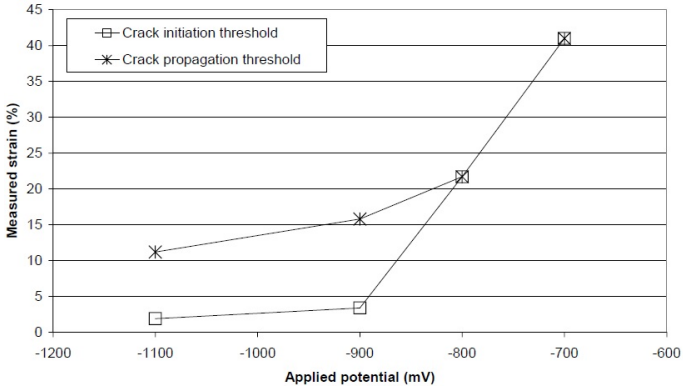


**Figure 2.4.6:** Graph from [4] showing relation between measured strain versus applied potential.

### Temperature and pressure

Lauvstad et al. also did testing on the effect of temperature and pressure. Temperature is an important parameter as it influences both diffusion of hydrogen and the thermodynamic driving force of the electrochemical mechanisms behind HISC. They found that increasing temperature had a modest impact on the elongation during HISC testing, as shown in figure 2.4.7. Even at 80 °C, secondary cracking was observed along with reduced elongation and RA ratio[6].

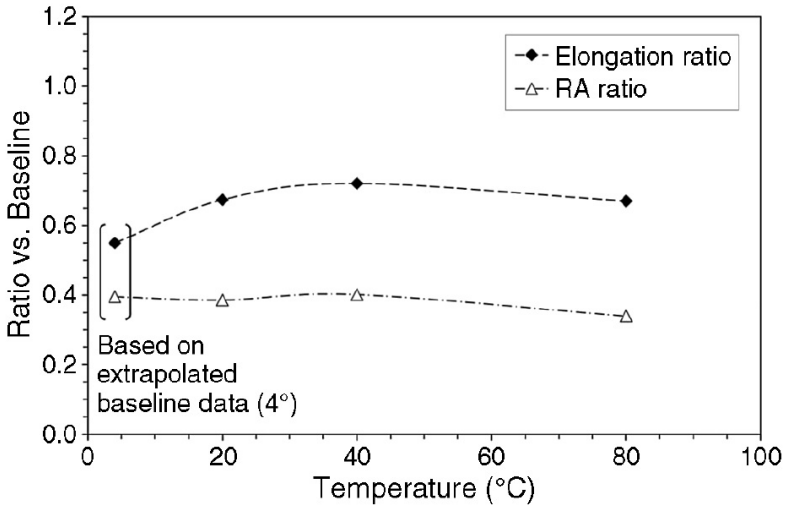


**Figure 2.4.7:** Graph from [6] showing test results of effect of temperature with air at test temperature as baseline value. SSRT of as-recieved HIP material in 3.5% NaCl at -1050 $mV_{SCE}$.

Subsea installations are placed at increasing depths which implies increasing pressure, and so the effect pressure has on HISC resistance has been subject to research. SSRT comparing 1 bar and 100 bars pressure showed little influence of pressure which were difficult to comment[6]. Long term tests has shown a somewhat lower resistance at 100 bars than at 1 bar with a marginally higher hydrogen concentrations in the material[35].

### 2.4.4 Stepwise loading

In relation to a joint intelligence project, stepwise increased loading was compared to loading directly to final load. The results from this testing gave similar critical loads whether the samples were loaded directly or stepwise to critical load[36].

### 2.4.5 Shakedown

As part of the Foinaven investigation, a sample was pre-strained to 5% total strain in the fully ductile condition and then in the embrittled condition loaded to a stress of 600 MPa. This sample showed no low temperature creep nor any crack initiation in 1000 hours. This demonstrates the effect called "shakedown" which has been recognised as a means to counteract HISC by increasing the elastic behaviour, hence lower plastic deformation and reduce the effect of creep. For the beneficial effect of shakedown to arise, the initial load must be higher than the future operational load and must be applied in the same direction[2].
Another article show that cold work gives other effects than shakedown. The study was regarding the influence of pre-straining of SDSS by experiments using cathodic charging in acid solution to achieve hydrogen embrittlement. The results indicated that the degree of embrittlement depend on level of cold work as increasing cold work resulted in reduction of elongation to failure.[22]

## 2.5 Design against HISC

HISC is the result of hydrogen, stress and susceptible material. Take away either one of these factors and HISC will be avoided. Although SDSS does not need CP against seawater, the CP systems are needed to protect other parts of subsea installations. Consequently the question often comes down to how much stress can be applied to the SDSS parts. This question has been focus on for decades of research, which has resulted in different design guidelines proposed and/or used by the offshore industry. This section will review some of these. Although the focus here is susceptible material vs. stress, other aspects of design against HISC will also be addressed.
In 2004 two draft guidelines were issued, one by NORSOK and the other by DNV. The work with the NORSOK guideline was meant as a "quick fix" solution based on the industry practice and experience with the material. At the time of issue (October 2005) it was anticipated that a standard or recommended practice would take replace it, and so it was issued as a Workshop Agreement (M-WA-01). The DNV guideline became the recommended practice (DNV-RP-F112) used in the industry. A summary of the design requirements in DNV-RP-F112 follow, but first proposed recommendations from two other studies are reviewed[36, 37, 3]

### 2.5.1 Foinaven Super Duplex Materials Cracking Investigation

The proceedings to the 1999 Offshore Technology Conference regarding the Foinaven Super Duplex Materials cracking investigation was made in response to one of the first major incidents of HISC in the offshore industry. In response to the cracking, a major multi-discipline investigation was commissioned where a set of acceptance criteria for the SDSS components in the field was developed. These were used on the BP Amoco Foinaven Field, and was later used as benchmark for further testing and development of design guidelines. It was assessed that cracking would not occur if either of these criteria was met[2]:

- The area was shielded from the CP system. This could be achieved by the combination of a high quality paint system and an encapsulation of the area.
- The future operational stress would not exceed the threshold for crack initiation which was found to be 0.5% total strain (i.e. roughly the same as yield stress). The total strain had to include measured residual stresses which in the case of the hubs in question was 460 MPa which is equal to a strain of 0.25%.
- Sufficient shakedown had been caused by a hydrostatic strength test.

### 2.5.2 OMAE Conference Proceedings from TWI

Although not recognised as a standard for design against HISC, the 2004 conference proceedings from Woollin (TWI) include recommendations for the subsea industry on the subject. Theses recommendations are summarised here:

- As DSS and SDSS materials are susceptible to HISC, exposure to potensials more negative than -850mV$_{SCE}$ should be avoided. If this is not practicable then the materials should be designed to be under displacement control rather than load control.

- For parts under load control exposed to -1000mV$_{SCE}$ to -1100mV$_{SCE}$, the recommendation is to limit the total strain to less than 0.5%. For materials with austenite spacing smaller than 30$\mu$m or potentials between -850mV$_{SCE}$ to -950mV$_{SCE}$, this limit may be relaxed to 0.75% or even 1% strain but qualification testing would be required. For small scale testing, dead-weigth tensile loading is recommended (unless it can be shown that the component would be subjected to displacement control).

- For welds, crack propagation was found preferentially from the HAZ, but crack initiation was favoured in the lower (proof) strength area of either HAZ, parent metal and weld metal. For welded parts, the total global strain is recommended to be lower than 0.5%, and for parts with coarser microstructures (austenite spacing $\geq$30 $\mu$m) a lower limit might be appropriate[4].

### 2.5.3 DNV Recommended Practice F112

This guideline is a comprehensive document which cover all aspects during design of DSS and SDSS components exposed to CP. The design requirements presented there involve both material quality and instructions for mechanical modelling and so a complete review is not appropriate for the current discussion. The design criteria in DNV-RP-F112 is divided into stress criteria and strain criteria where design according to either criteria is satisfactory. The following considerations apply for both sets of criteria:

- Material quality is characterized as coarse or fine grained material. The latter can be assumed for HIP material, weld material, rolled plates with wall thickness less then 25 mm, pipes and tubes made by extrusion, seamless rolling and drawing. Other materials qualify as "fine grained" if austenite spacing is measured to less than 30 $\mu$m. Fine grained material is graded with a material quality factor $\gamma_{HISC}$=100%, and coarse grained material is graded $\gamma_{HISC}$=85%.

- Residual stresses is to be evaluation near girth welds unless a complete heat treatment of the component is done. Within a distance $L_{res}$ from the weld centreline, residual stresses is estimated to $\epsilon_{res}$=0.25% except for at weld toes where the estimate is $\epsilon_{res}$=0.15%.

### Linear elastic stress criteria

The linear elastic stress criteria are expressed in percent of specified minimum yield stress (SMYS, max. 450 MPa for DSS and 550 MPa for SDSS in DNV-RP-F112) and consist of two stress limits, both of which shall be met. These are for membrane stress and for membrane + bending stress as given in equations 2.4a and 2.4a, respectively.

$$\sigma_m \leq \alpha_m \times \gamma_{HISC} \times SMYS \quad \text{(2.4a)}$$

$$\sigma_{m+b} \leq \alpha_{m+b} \times \gamma_{HISC} \times SMYS \quad \text{(2.4b)}$$

$\alpha_m$ for membrane stress is defined as 80% everywhere which gives maximum membrane stresses of 80% or 68% of SMYS for fine and coarse grained microstructure, respectively. For the current discussion where welds are not considered (considering requirements outside $L_{res}$ only), $\alpha_{m+b}$ is either 90% to 100% depending on presence of stress raisers. The maximum membrane+bending stress then become 100% and 85% of SMYS for fine and coarse grained material, respectively, when no stress raisers are present. With stress raisers present, the maximum membrane + bending stress is 90% and 76.5% of SMYS for fine and coarse grained material, respectively.

### Non-linear strain criteria

The strain criteria depends on distance from surface of the material, material quality and distance from welds (inside/outside $L_{res}$). When considering areas out of $L_{res}$ as for the stress criteria the allowable strain within 5% of the wall thickness from any surface is 0.30%. Outside 5% of the wall thickness, the allowable strain is 1.00% and 0.60% for fine and coarse grained material, respectively.

### Other notes

In addition to the design criteria above, some other notes from DNV-RP-F112 are worth mentioning. Coating shall generally not be the only means against HISC, but use of high integrity coating may give rise to higher utilization of the materials. If coating is used as a barrier for hydrogen ingress, a comprehensive review of all factors influencing the reliability of the coating must be carried out. Regarding imposed stresses, both momentary loads and pure compressive stresses alone can be disregarded in terms of HISC[3].

## 2.6 Microstructural examination

### 2.6.1 The EBSD technique

Scanning electron microscopes (SEM) use a beam of electrons instead of visible light to develop images of the sample of interest. When the electrons hit the sample surface a range of signals are developed, some of which come from backscattered electrons. A certain amount of these have interacted with the crystal lattice. The directions and planes of the lattice cause diffraction of the electrons into cone formations according to Bragg's law. These cones illuminate on a phosphorous screen which is close enough to the sample so that the part of the cone appear as line (called Kikuchi lines), see image to the left in figure 2.6.1. In this way, the Kikuchi lines consistute a diffraction pattern which contain all data of the crystal lattice of the sample at the given point, see image to the right in figure 2.6.1. The electron backscattered diffraction (EBSD) technique use this feature to scan an area on the sample and collect diffraction patterns from each point on the surface in the area. This information can later be analysed to give information of the microstructure of the sample [38, 39].

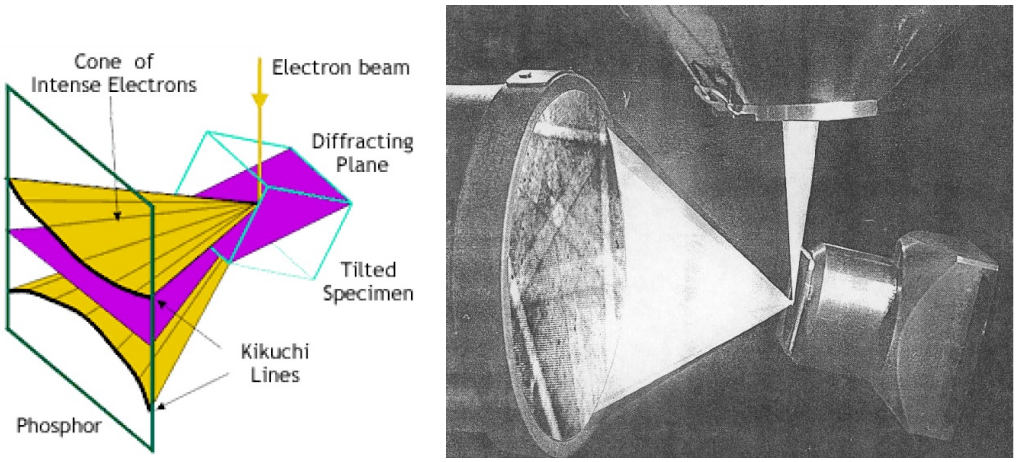


**Figure 2.6.1:** Images illustrating how EBSD patterns are developed and recorded in the SEM. The image to the left (from [40]) shows how incoming electron beam is diffracted into Kikuchi lines. The image to the right (from [41]) shows how the Kikuchi lines make out a diffraction pattern.

### 2.6.2 Sample preparation and EBSD settings

The electrons that create the diffraction patterns interact with the outer 50 nm of the surface only, and so having a very smooth sample surface is critical. This can be achieved with combinations of different instruments such as ion sputtering, electrochemical polishing and plasma cleaning. The surface preparation is material specific and a certain

amount of trail and error is necessary for each new material. Other parameters to obtain good diffraction patters are specimen-to-screen distance, working distance, electron beam voltage, scanning speed etc.[38, 42]

### 2.6.3 Indexing

The centreline of the diffraction bands (Kikuchi lines) represent a plane in the crystal structure, and each line crossing give an axis in the lattice. In this way, diffraction patterns hold information on the crystal structure and orientation at each point during scanning. Good diffraction patterns contain several lines and the scan typically comprise on the order of $10^5$ patterns. To ease the job of indexing these scans, the software use Hough transformation to convert each Kikuchi line in the pattern into a point which is easier to detect. The lines detected are compared to a database of crystal structures and a voting scheme is employed to give the most probable indexing. During this process, a set of quality parameters are set for each pattern:

- Confidence Index (CI): This parameter comes directly from the voting scheme mentioned above as the indexation of highest probability is compared to the second most probable. The CI range from 0 to 1, where higher CI indicates higher confidence. Tests on an FCC material showed that a CI of 0.1 was correctly indexed in 95% of the time.

- Image Quality (IQ): After the Hough transformation, the points developed are evaluated after intensity and are measured as image quality.

- Fit: This parameter give the average angular deviation of the Kikuchi lines from the indexed orientation.

To sum up, good diffraction patterns yield high CI, high IQ and low Fit values.

### 2.6.4 Analysis

From all EBSD scans, a variety of images and plots can be produced. The EBSD images relevant for this work are given below.

- Inverse pole figure (IPF) maps: The area scanned is reproduced with each point assigned a color. This color correspond to the inverse pole figure shown in figure 2.6.2 and relate to the orientation of the crystal lattice compared to the normal axis on the sample surface. The color would therefore be the same for orientations which are only distinguished by rotation around the normal axis. One way to know for

certain that an area of similar color represents a grain is to rotate the viewing angle so that a second IPF map is produced. The IPF maps do not distinguish between phases if all points are included. Alternatively, either phase can be left out to view the orientation of either one phase alone.

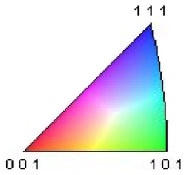


**Figure 2.6.2:** The image show the inverse pole figure (IPF) which the IPF maps relates to. The IPF is similar for the austenite and the ferrite phase.

- Phase maps show phases as different colors. Points indexed as ferrite is red and austenite is green.
- Pole figure plots: Every orientation relates to three 100 axes and the pole figure plots include a point in the plot for each of these axes. All orientations are represented in a circle by three points. These plots can therefore give information on texture and degree of isotropy in the microstructure given that a representative area is evaluated. Clusters in the plot represent either large grains or repeating orientations (texture), i.e. dominant planes and directions. Random orientation in the area evaluated is seen as an uniform pole figure plot.

An option when EBSD maps and plots are developed is to exclude points of low CI value (least dependable points) such as along grain boundaries. The downside of CI partitioning is that points that happen to have low quality even though it is within a grain are also filtered off. To avoid this, the clean-up function "Grain CI standardization" can be applied. This function assigns all points within a grain the highest CI value in that grain. A partition with a lower CI value for filtering will, after this clean-up, include points with similar orientation as the other points within the grain[42].

### 2.6.5 EDS

X-ray signals are also among the signals in the SEM. Energy-dispersive spectroscopy (EDS) is a method of analysing the chemical composition of samples by means of the X-ray signals that come from detectable energies. EDS can be used in different ways and the function relevant for the current project is to qualitatively analyse the an area on the sample for chemical species present. As for the EBSD technique, EDS scans are better and more reliable for flat, polished samples. In order to get reliable and quantitative results, a homogeneous and flat place must be analysed. [38].

# Chapter 3

# Materials and experimental methods

The experimental work in this project had two purposes which relate to each other; finding susceptibility to HISC and characterising the microstructure of the materials. By including a microstructural analysis, the results from the HISC tests could be discussed with a better background regarding microstructural properties of the materials.

## 3.1 Material

For the experimental work carried out in this project, material from two different suppliers and manufacturing methods of Super Duplex Stainless Steels (SDSS) were provided from Aker Solutions ASA. One material was produced by Hot Isostatic Pressing (HIP), and the other was produced by forging. The HIP material and the forged material was of grade UNS S32550 and UNS S32760 respectively, with chemical composition as given in table 3.1.1 [43, 44]. Mechanical data and results from microstructural analysis from suppliers and third parties are given in table 3.1.2 [43, 44, 45]. In data for the forged material in this table are from test pieces taken in a longitudinal direction from locations at 1/2 thickness. Images of the HIP and forged material is shown in figure 3.1.1 with sample location sketched on the pieces.

**Table 3.1.1:** Chemical composition of Super Duplex materials.

| Material | C | Si | Mn | P | S | Cr | Ni | Mo | Cu | W | N |
|---|---|---|---|---|---|---|---|---|---|---|---|
| HIP | 0.016 | 0.44 | 1.32 | 0.012 | 0.003 | 25.9 | 6.4 | 3.21 | 1.78 | 0.02 | 0.25 |
| Forged | 0.023 | 0.29 | 0.53 | 0.027 | 0.001 | 24.92 | 6.96 | 3.58 | 0.59 | 0.5 | 0.233 |

**Table 3.1.2:** Data from testing and measurements of materials.

| Material | Yield strength (YS) [MPa] | Tensile strength (UTS) [MPa] | Elongation [%] | Charpy [J] | Ferrite [%] | Austenite spacing [$\mu$m] |
|---|---|---|---|---|---|---|
| HIP | 594 | 850 | 34.4 | 41 | 46.0 | 12.9 |
| Forged | 559 | 766 | 41.8 | 100 | 46.7 | 51.5 |

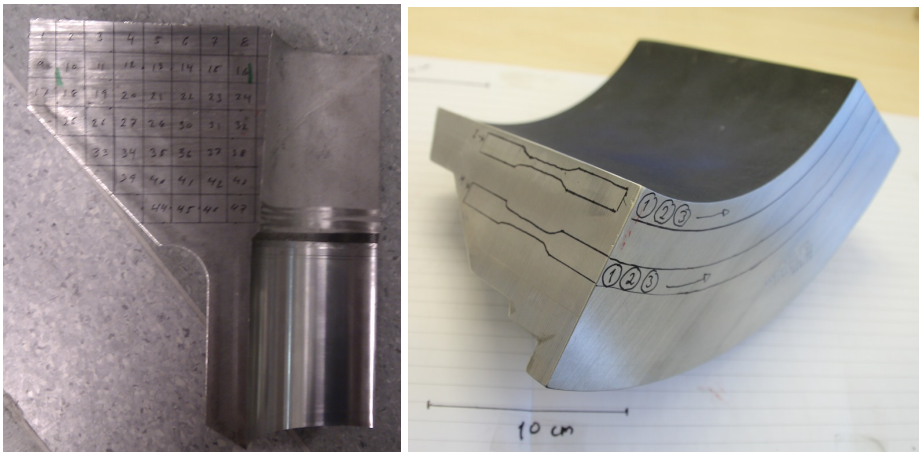


**(a)** HIP material **(b)** Forged material

**Figure 3.1.1:** Pictures of SDSS material with placement for samples sketched on parts. Samples from the centre of the forged part were tested in the this work.

## 3.2 Tensile testing

The HISC testing was to be related to the yield stress of the material. Mechanical properties from the material were available from suppliers and third party tests, but these data were from samples cut from unknown locations and of unknown dimensions. The stress-strain curves were also necessary to relate the results to strain. It was therefore decided to collect new stress-strain curves. For the forged material, the tensile samples were taken from a similar location from the forging as the samples for the HISC tests (same distance from inner and outer diameter). The cutting and machining of the samples for both tensile testing and HISC testing was done by the workshop for fine mechanics at the university. The locations on the material from which the specimens were cut from locations seen in figure 3.1.1. The dimensions for the samples are shown in figure 3.2.1 along with the MTS810 100kN tensile test machine used. The tensile tests were done with staff at the Department of Materials Science and Engineering. From the HIP material, two samples for tensile testing were prepared and tested while from the forged material, three samples were tested. For both materials, the data from the curves with the lowest value for yield strength were used for calculation related to the HISC testing.

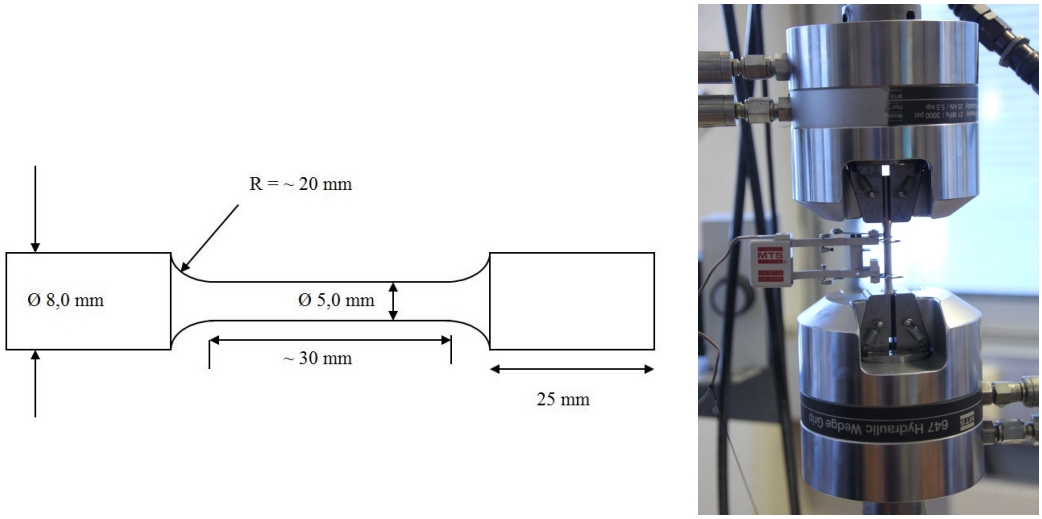


**Figure 3.2.1:** The sketch to the left shows the dimensions of the stress-strain samples, and the image to the right show the tensile testing machine with a sample inserted.

## 3.3 HISC testing

### 3.3.1 Test matrix

The materials were exposed to HISC favouring environment and stressed with incrementally increased applied load. For both materials 10 samples were prepared for HISC testing, 5 of which were smooth. The other 5 samples had a circumferential 0.25 mm deep V-notch, with $60°$ angle[1], machined in the middle of the thin section. The drawing for smooth HISC samples is shown, along with machined samples from HIP material, in figure 3.3.1.

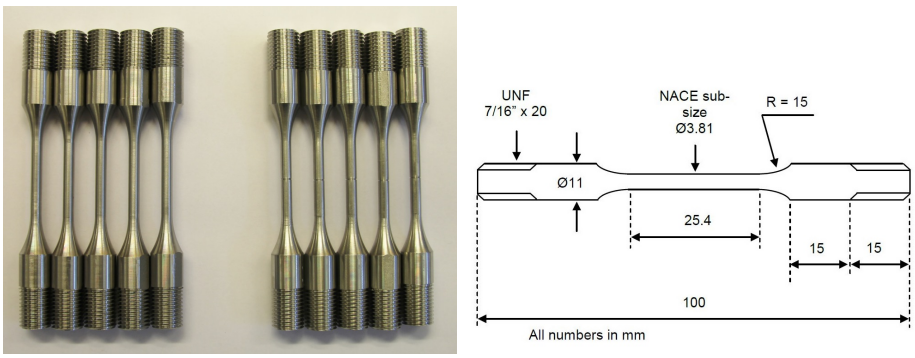


**(a)** HISC samples, smooth samples to the left and notched to the right.

**(b)** Drawing showing the dimensions for smooth HISC samples.

**Figure 3.3.1:** Images showing the HISC sample drawing and machined samples.

[1]The inner radius of the V-notch from machining was 0.072 mm.

The test matrix consisted of three consecutive steps with the following conditions. To simulate cathodic protection from sacrificial anodes in seawater, the samples were exposed to an impressed potential of -1050 $mV_{Ag/AgCl}$ in a 3.5% NaCl solution during all three steps. A summary of the three stages are given in table 3.3.1.

**Table 3.3.1:** The table comprises the most important parameters for the HISC testing for the three stages that the testing consisted of.

| Timeline | Stage 1<br>Hydrogen charging | Stage 2<br>Constant load | Stage 3<br>Increasing load |
|---|---|---|---|
| Duration | $\geq$ 10 days | $\geq$ 10 days | Until fracture |
| Media | 3.5% NaCl | 3.5% NaCl | 3.5% NaCl |
| Polarization | -1050 $mV_{Ag/AgCl}$ | -1050 $mV_{Ag/AgCl}$ | -1050 $mV_{Ag/AgCl}$ |
| Temperature | 80 °C | RT | RT |
| Stress state | Unstressed | 86% of YS | Day before + 4% of YS |

1. Firstly, the samples were pre-charged with hydrogen at elevated temperature. The temperature was held at 80 °C, and the water level was controlled and adjusted daily to keep the solution at correct NaCl concentration. The samples were held in this condition for at least 10 days. An image of the set-up for the hydrogen charging and a sketch of the electrical set-up is shown in figure 3.3.2.

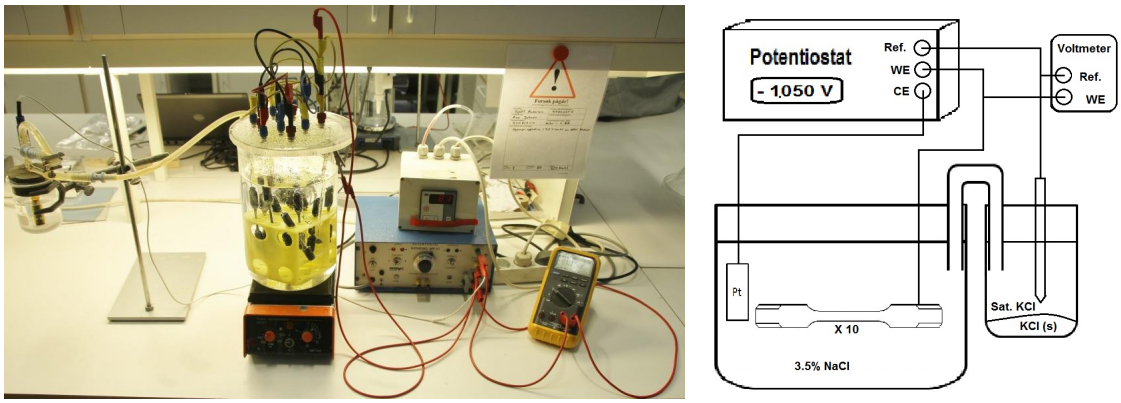


**Figure 3.3.2:** The image to the left shows the set-up for hydrogen pre-charging and the sketch to the right shows the corresponding electrical set-up.

2. After the pre-charging, the samples were put in individual containers exposed to similar environment, but at room temperature. While exposed to this HISC favouring environment, the samples were loaded in tension to 86% of the yield strength and left in this condition for at least 10 days[2]. The electrical set-up was equivalent

[2]Low-temperature creep was not accounted for during step 2. The stress each sample was subjected to therefore reduced during the 10 days.

to during pre-charging.

3. The final step of the testing was incrementally increasing loads on the samples. From the load level after step 2, the load was increased with stress corresponding to 4% of the yield stress once a day until fracture. During this step, the day-to-day low-temperature creep was incorporated in the loading. The equipment used for step 2 and 3 is shown in figure 3.3.3.

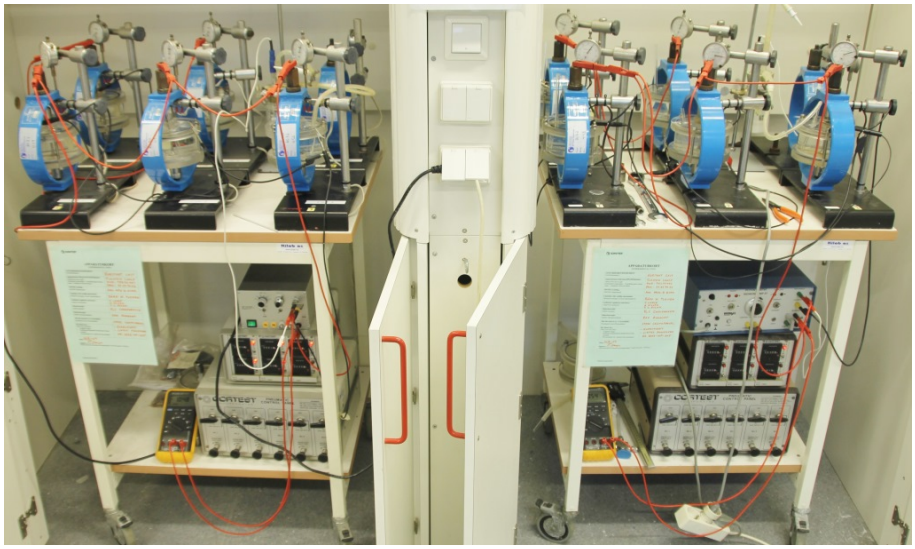

**Figure 3.3.3:** Image showing the equipment used for HISC testing.

### Incidents during testing

During the pre-charging of the first round of tests, which was with the HIP material, the threaded area of the samples were covered by pieces of heat shrink tubing to prevent hydrogen charging of these parts. The outer layer of the tubing material dissolved and deposited on the sample surfaces. The charging was braked twice for maintenance where the samples were cleaned with distilled water and ethanol and the deposited material was removed by careful polishing with sandpaper with 500 grit[3]. The first day of pre-charging of the HIP material, the electrical circuit was broken and the 10 days were counted after stable system was restored. Due to difficulties in compressing one ring (proof ring 3111), extra greasing was applied to the threads of the fastening nut before the second (forged samples) round of testing.

[3]These brakes for maintenance lasted less than 20 minutes.

### 3.3.2 Cortest Proof Rings

Cortest proof rings are equipment for material testing against stress corrosion cracking in $H_2S$ environment (in accordance with NACE TM-01-77 test standard) and HISC testing. It is operated by compressing the ring manually with the material sample inserted. When compressed, the ring exerts a stress state of uniaxial tension and the deflection in the ring decide the load. There are 12 of these proof rings in the SINTEF laboratory (purchased in 1993 and 1995), 6 of which are designed for less load and so larger ring deflection correspond to the same load of the other 6 rings. The deflection-to-load relation is linear and each ring is accompanied by an individual calibrated conversion chart used to calculate ring deflection. The stress calculations were based on the area of the most narrow cross section, i.e. in the notch for the notched samples. Further details about the calculation is given in the Appendix A along with an example. An image of a Cortest Proof Ring is shown in figure 3.3.4 with important features marked. The sample (A in figure 3.3.4) is inserted into a transparent container (B) which in turn is placed and fastened inside the proof ring. The actual loading is done by measuring the outer diameter of the ring at the places indicated by red arrows. The rough measurement is done by the dial indicator (F) and fine tuning with a digital caliper. The load is derived from amount of yield stress (e.g. 86% initially) and the area of the most narrow cross-section. The ring deflection is obtained by turning a fastening nut (C) with a wrench (D), while holding the sample static by another wrench (E). The container was then filled with 3.5% NaCl solution and the system is connected to an electric circuit. The time to failure is monitored (G) for each ring.[46]

### 3.3.3 HISC results

After fracture, the outer diameter of the rings were measured and compared to the last diameter of the ring measured before fracture. This gave the deflection in the ring which were used for obtaining the stress (and strain) values for "Fracture" in the result part. The outer diameter was also compared to the last ring diameter of which the sample had not fractured after one day. This diameter was used to derive "No-fracture" values[4]. These calculations were similar to the calculations of ring deflection[5]. The ring deflection at fracture/no-fracture was used to find the load applied to the samples with a spread sheet from the conversion charts. The spread sheets (and the conversion charts) has been used many times since acquisition, and is of unknown accuracy. A load cell, seen in figure 3.3.4, was therefore used to verify the results. The load cell used was a type MP1 basic

[4]NOTE: This value is derived from the ring diameter after one day, i.e after low-temperature creep.
[5]More on calculations on ring deflection in Appendix A.

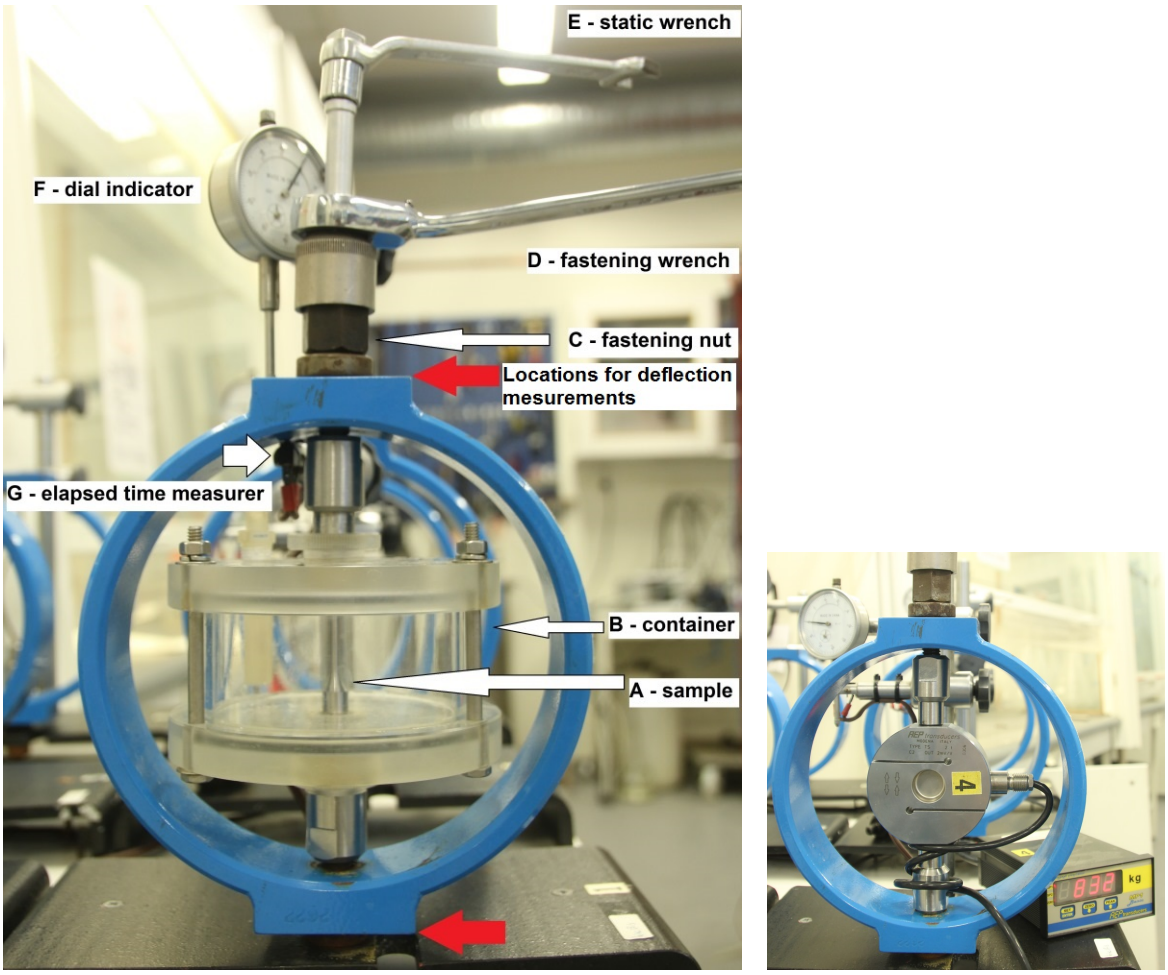


**Figure 3.3.4:** The image to the left show a Cortest proof ring with the most important features indicated. The image to the right show the load cell inserted.

from AEP transducers. The load cell was inserted in the proof ring and load was applied as if the load cell was a sample. The ring deflection at fracture/no-fracture was used to compress the ring to diameter corresponding to each value from the testing. This was conducted three times for each value of the results and the *lower load measured* was used for further analysis.

## 3.4 Hydrogen measurements

Four of the HISC samples were tested by staff at SINTEF Materials and Chemistry for hydrogen content after fracture. These were two HIP samples and two forged samples, one notched and one smooth of each. Before the hydrogen measurements, the samples were contained in a freezer (at approx. $-19\,^{\circ}\mathrm{C}$) after fracture to limit loss of hydrogen due to diffusion at room temperature. For the measurements, pieces of the region near

the fracture surface including the fracture surface were cut from the HISC samples. The pieces weighted from 0.6176 g to 0.7375 g. The hydrogen measurements were done with melt extraction in a JUWE Laborgeräte GMbH H-mat 225. In the process $CO_2$ and $H_2$ gas is released from the sample. Nitrogen is used as carrier gas as thermal conductivity is measured and compared to a reference gas flow of hydrogen gas. The change in thermal conductivity over time is proportional to hydrogen content and is used to detect the amount of hydrogen from the sample with an accuracy of 0.001 ppm[47].

## 3.5 Fracture surface examination

A selection of fractured samples were inspected in Scanning Electron Microscopes (SEM). For the examination, a FESEM Zeiss Ultra 55 Limited Edition and a LVFE SEM Zeiss Supra 55 VP were used. From each material one sample from the tensile testing, two notched samples and two smooth samples from the HISC testing were inspected. Different methods of preparation were used. Approx. 1 cm long part of the fractured piece was cut off and rinsed in acetone. Next, the piece was cleaned in an ultrasonic bath for 10 minutes. Bot distilled water and acetone were tested as medium in the ultrasonic bath. Finally, the sample was rinsed with ethanol and air dried. The SEM was operated with a voltage of 15 kV and the secondary electron detector was used to inspect the surfaces.
After the features on the fracture surface of the HIP samples were revealed, EDS analysis was employed to determine amount of Chromium in different parts of the surface. One of the smooth HIP samples was used for this purpose. The SEM was operated in principally the same settings, but the working distance was reduced to 10 mm. The EDS analysis was done with the LVFE SEM Zeiss Supra 55 VP.

## 3.6 Microstructural examination

For microstructural examination, suitable pieces of material were cut from the materials. From the forged material, the piece was cut from similar distance from inner and outer diameter of the forging as the samples for the HISC tests. EBSD scans of the forged material were made of two surfaces on the piece to correspond to the cross-section and in the longitudinal direction of the HISC samples. "Longitudinal" scans were made of the piece oriented so the horizontal direction of the EBSD maps presented was lengthwise on the forging and the vertical direction along the thickness direction. The EBSD was conducted with a FESEM Zeiss Ultra 55 Limited Edition attached to a NORDIF UF-1000 EBSD detector. Scans of 100 $\mu$m $\times$ 100 $\mu$m and 200 $\mu$m $\times$ 200 $\mu$m areas were done, as well as 1000 $\mu$m $\times$ 1000 $\mu$m areas on the forged material.

### 3.6.1 Sample preparation and SEM settings

The settings for the SEM during EBSD scanning are listed in table 3.6.1. Different sample preparations were tested and the combination that gave best scans and was used to produce most of the scans presented in this report is given below.

1. Grinding with decreasing roughness; 80 - 320 - 800 - 1200 grit.
2. Mechanical polishing with decreasing roughness; 6 $\mu$m - 3 $\mu$m - 1 $\mu$m.
3. Ion sputtering with a Hitachi IM-3000 Flat Milling System with settings; 30 minutes, 75$^\circ$ tilt, 4 kV, flowrate 0.07 cm$^3$/min, rotation mode 2 and eccentricity 0.
4. Plasma cleaning with a Fischione Instruments Model 1020 for 5 minutes.

**Table 3.6.1:** The table lists the most important SEM settings for the EBSD scans.

| Parameter | Value |
|---|---|
| Acceleration voltage [kV] | 20 |
| Working distance [mm] | Approx. 20 |
| Tilt angle | 70$^\circ$ |
| Max. aperture [$\mu$m] | 300 |

### 3.6.2 Indexing and analysis

The indexing was carried out with the software TSL OIM Data Collection 5.32 and the analysis was done with OIM Analysis 6. The indexing was set to identify the patterns as either ferrite or austenite. Parameters set for the Hough transformation and for clean-up are given in table 3.6.2 and table 3.6.3, respectively.

**Table 3.6.2:** The table lists the settings for indexing of EBSD scans.

| Parameter | Setting |
|---|---|
| Hough type | Classic |
| Hough Resolutions | Low |
| Convolution Mask | Medium $9 \times 9$ |
| Minimum Peak Magnitude | 5 |
| Minimum Peak Distance | 15 |
| Peak Symmetry | 0.5 |
| Vertical Bias | 0 % |
| Binned Pattern Size | 120 |
| Theta Step Size | $1^\circ$ |
| Rho Fraction | 95 % |
| Peak Count Max./Min. | 7/3 |

**Table 3.6.3:** The table lists the settings for clean-up by Grain CI Standardization.

| Parameter | Setting |
|---|---|
| Grain tolerance angle | 5 |
| Minimum grain size | 5 |
| Grain must contain multiple rows | On |

The maps and plots presented are partitions with CI $\geq$ 0.05 of EBSD scans after the clean-up above. The values of CI, IQ and fit are from before clean-up.

# Chapter 4

# Results

## 4.1 Tensile testing

The results from the tensile testing carried out in this project is given in table 4.1.1. The data from the samples with the lower value for yield strength (sample 2 and 3 in table 4.1.1) were used for design of experiment and post-testing calculations. The stress-strain curves obtained from these samples is shown in figure 4.1.1.

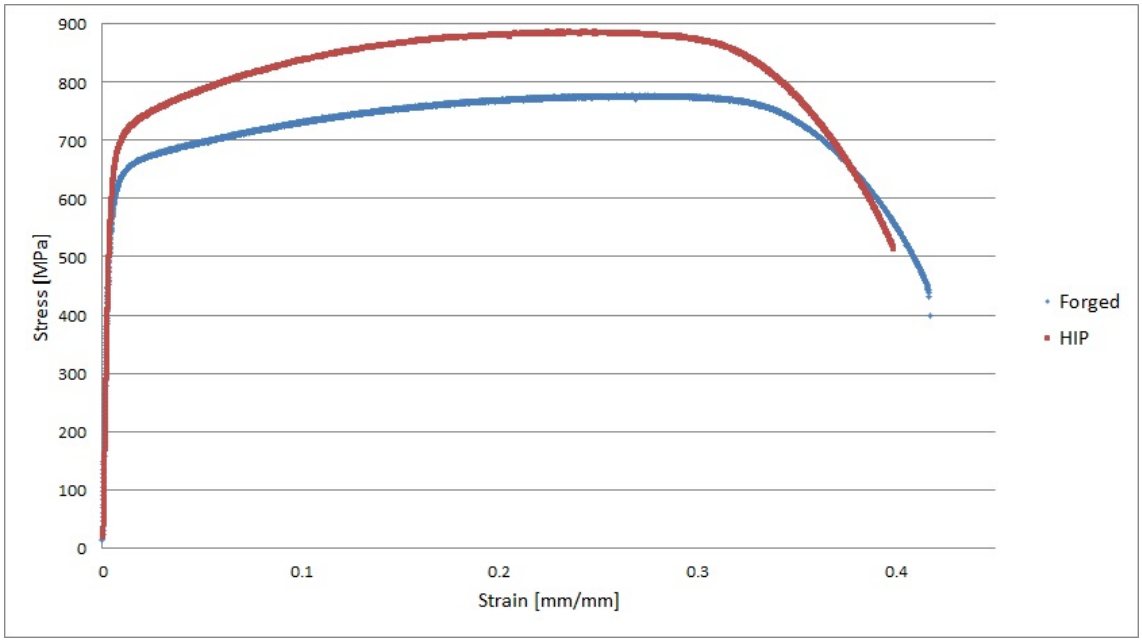


**Figure 4.1.1:** The graphs show the stress strain curves for the materials from the tensile testing.

**Table 4.1.1:** Results from the tensile testing conducted in the project.

| Material | Sample | Modulus [GPa] | Yield strength YS [MPa] | Tensile strength UTS [MPa] | UTS/YS | Elongation [mm/mm] |
|---|---|---|---|---|---|---|
| HIP | 1 | 170.4 | 667.3 | 891.4 | 133.6 % | 35.3% |
| | 2 | 184.5 | 653.3 | 888.5 | 136.0 % | 39.8% |
| Forged | 3 | 172.6 | 581.3 | 777.1 | 133.7 % | 41.7% |
| | 4 | 176.5 | 589.8 | 782.4 | 132.7 % | 42.9% |
| | 5 | 176.8 | 589.2 | 780.3 | 132.4 % | 42.6% |

## 4.2 HISC tests

### 4.2.1 Remarks from operator

- There were incidences indicating low temperature creep which had to be accounted for during the HISC tests. The first observation was that the measured outer diameter of the HISC rings had increased during the 10 days of step 1. This happened for one notched and three smooth samples of the HIP material along with all smooth samples from the forged material (no notched samples). This observation has seemingly two possible causes, where one is inaccuracy in measurement. The other is elongation of the samples during the 10 days, a process know as low temperature creep. The two possible causes were not possible to distinguish, so the incrementally increasing stress during step 3 were calculated using the outer ring diameter *after* the first 10 days (of step 2) as the baseline value. The other incident was during step 3 of the tests (incrementally increasing load). The operator experienced relaxation in ring deflection from one day to the next on smooth samples which was from 0.02 to 0.05 mm. This corresponds to approximately 5% to 11% of YS according to the conversion charts and even more with the load cell measurements, as seen in table 4.2.2. The loading was therefore made using the outer diameter of the ring after last loading as baseline value. Any potential low temperature creep would thereby be incorporated in the loading. The effect became more pronounced as the load corresponded to stresses much higher than the yield stress of the material and was noteworthy more pronounced for the HIP material than the forged material.

- The loading of smooth samples from HIP material required a larger motion of the fastening wrench during the final increments of loading than the forged samples, i.e. evident larger straining for the HIP samples.

- One of the proof rings (ring 3111) for the notched samples was harder to compress than the other rings.

### 4.2.2 Stress measurements

The results from each sample of the HISC tests are given as a "No-fracture" value and a "Fracture" value as explained in the chapter on experimental methods. This procedure gives a larger gap between no-fracture and fracture values for the samples where the effect described above (potential low temperature creep) was most pronounced. The actual diameter of the most narrow cross section on the HISC samples diameter varied from 3.74 mm to 3.87 (- 0.5 mm for the notched samples) as seen in the Appendix B.

#### Conversion charts

The ring deflection at fracture/no-fracture was used with the conversion charts from Cortest to calculate the load applied. This load was then related to the yield strength of each material and given in table 4.2.1. Here, time to fracture (in hours) after last loading is included and D.L. stands for "During Loading".

**Table 4.2.1:** Results from the HISC testing at fracture and before fracture in % of yield strength calculated from the Cortest conversion charts along with time to fracture. D.L. stands for during loading and SD is standard deviation.

| Sample | Forged | | | | HIP | | | |
|---|---|---|---|---|---|---|---|---|
| | Test | No fracture | Fracture | Time [h] | Test | No fracture | Fracture | Time [h] |
| Smooth | F1 | 95.1 % | 107.2 % | 0.75 | H1 | 103.4 % | 109.9 % | D.L. |
| | F2 | 88.0 % | 99.5 % | D.L. | H2 | 103.4 % | 113.7 % | D.L. |
| | F3 | 90.1 % | 106.8 % | 0.17 | H3 | 104.6 % | 115.5 % | D.L. |
| | F4 | 89.8 % | 94.8 % | 17.2 | H4 | 96.0 % | 111.1 % | 2.9 |
| | F5 | 94.4 % | 108.2 % | 0.25 | H5 | 96.7 % | 104.0 % | D.L. |
| Average | | 91.5 % | 103.3 % | | | 100.8 % | 110.8 % | |
| SD | | 3.1 % | 5.9 % | | | 4.1 % | 4.4 % | |
| Notched | F6 | 106.4 % | 110.0 % | 1.7 | H6 | 112.2 % | 116.7 % | 1.4 |
| | F7 | 110.5 % | 114.2 % | 1.3 | H7 | 109.8 % | 114.4 % | 8 |
| | F8 | 96.7 % | 100.4 % | 0.33 | H8 | 93.1 % | 96.5 % | 0.5 |
| | F9 | 106.5 % | 110.1 % | 2.5 | H9 | 107.8 % | 113.4 % | 1.6 |
| | F10 | 104.1 % | 107.9 % | 6.6 | H10 | 110.1 % | 113.5 % | 2 |
| Average | | 104.8 % | 108.5 % | | | 106.6 % | 110.9 % | |
| SD | | 5.1 % | 5.1 % | | | 7.7 % | 8.2 % | |

#### Load cell

After reviewing the data from the conversion charts, it was decided to verify the results with a load cell. As with the conversion chart, the data on ring deflection was used with the load cell and the results were related to the yield strength. The results found with the load cell is given in table 4.2.2 and in more detail in Appendix B.

**Table 4.2.2:** Results from the HISC testing at fracture and before fracture in % of yield strength by using a load cell along with time to fracture. D.L. stands for during loading and SD is standard deviation.

| Sample | Forged | | | | HIP | | | |
|---|---|---|---|---|---|---|---|---|
| | Test | No fracture | Fracture | Time [h] | Test | No fracture | Fracture | Time [h] |
| Smooth | F1 | 106.2 % | 119.3 % | 0.75 | H1 | 114.3 % | 120.6 % | D.L. |
| | F2 | 103.6 % | 116.2 % | D.L. | H2 | 117.3 % | 129.8 % | D.L. |
| | F3 | 100.0 % | 118.2 % | 0.17 | H3 | 114.3 % | 126.2 % | D.L. |
| | F4 | 107.3 % | 112.3 % | 17.2 | H4 | 109.4 % | 123.3 % | 2.9 |
| | F5 | 107.2 % | 118.8 % | 0.25 | H5 | 107.9 % | 115.2 % | D.L. |
| Average | | 104.8 % | 117.0 % | | | 112.6 % | 123.0 % | |
| SD | | 3.1 % | 2.9 % | | | 3.9 % | 5.6 % | |
| Notched | F6 | 112.4 % | 115.2 % | 1.7 | H6 | 117.8 % | 122.1 % | 1.4 |
| | F7 | 117.0 % | 120.6 % | 1.3 | H7 | 116.0 % | 121.5 % | 8 |
| | F8 | 102.4 % | 106.0 % | 0.33 | H8 | 98.3 % | 101.8 % | 0.5 |
| | F9 | 113.5 % | 117.2 % | 2.5 | H9 | 114.8 % | 120.3 % | 1.6 |
| | F10 | 112.5 % | 116.0 % | 6.6 | H10 | 119.8 % | 123.5 % | 2 |
| Average | | 111.5 % | 115.0 % | | | 113.3 % | 117.8 % | |
| SD | | 5.5 % | 5.5 % | | | 8.6 % | 9.0 % | |

As is seen when comparing table 4.2.1 with table 4.2.2, the loads derived from the spread sheet were consistently lower what the load cell measured. Due to higher confidence in the load cell (evaluated in the "Discussion" chapter), values from the load cell were used for further analysis and discussion. It is also clear from the tables that test sample F8 and H8 which both used proof ring 3111 showed consistently lower values compared to the other rings. For these reasons, the further analysis was done both with and without the samples from ring 3111. For comparison of averages and standard deviations, the data on notched samples from table 4.2.2 is reproduced without the data from ring 3111 in table 4.2.3. The results from the load cell with and without data from proof ring 3111 are shown graphically with standard deviations in figures 4.2.1 and 4.2.2.

**Table 4.2.3:** Results from the HISC testing of the notched samples without data from proof ring 3111 in % of yield strength by using a load cell along with time to fracture. D.L. stands for during loading and SD is standard deviation.

| Sample | Forged | | | | HIP | | | |
|---|---|---|---|---|---|---|---|---|
| | Test | No fracture | Fracture | Time [h] | Test | No fracture | Fracture | Time [h] |
| Notched | F6 | 112.4 % | 115.2 % | 1.7 | H6 | 117.8 % | 122.1 % | 1.4 |
| | F7 | 117.0 % | 120.6 % | 1.3 | H7 | 116.0 % | 121.5 % | 8 |
| | F9 | 113.5 % | 117.2 % | 2.5 | H9 | 114.8 % | 120.3 % | 1.6 |
| | F10 | 112.5 % | 116.0 % | 6.6 | H10 | 119.8 % | 123.5 % | 2 |
| Average | | 113.8 % | 117.3 % | | | 117.1 % | 121.8 % | |
| SD | | 2.2 % | 2.4 % | | | 2.2 % | 1.3 % | |

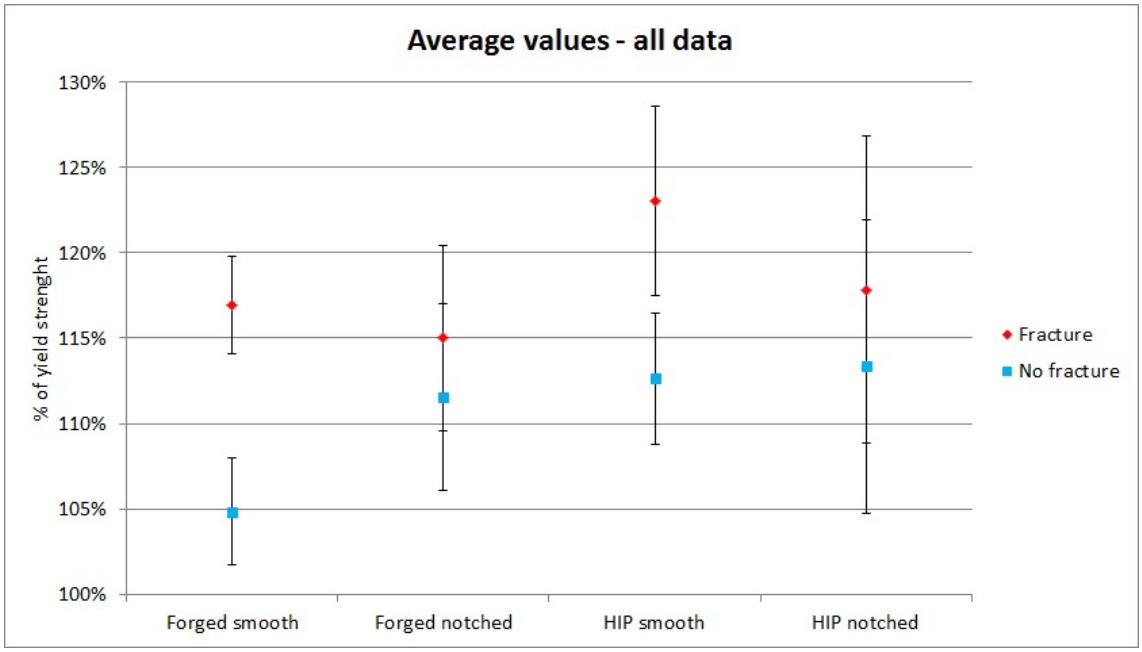


**Figure 4.2.1:** The graph shows the average stress at which the samples fractured and last load without fracture (no fracture).

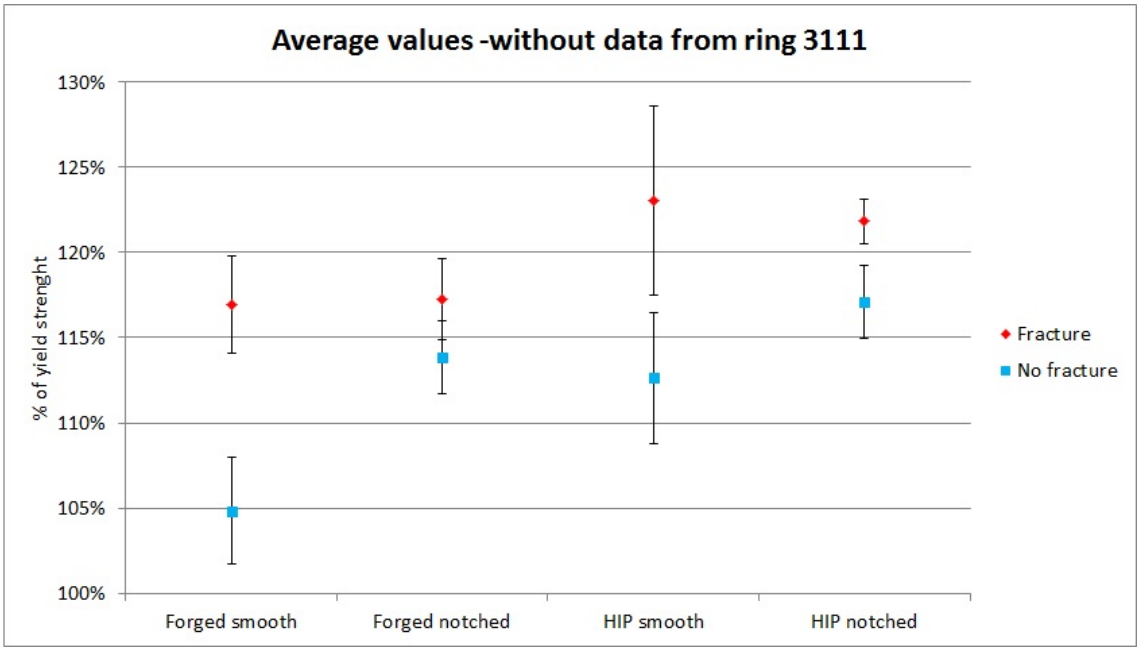


**Figure 4.2.2:** The graph shows the average stress at which the samples fractured and last load without fracture (no fracture), without the samples from proof ring 3111.

The fracture and no-fracture values can be compared to the austenite spacing given in the supplier documentation. This is shown in figure 4.2.3 for the smooth samples and in figure 4.2.4 for the notched samples. The data from ring 3111 is not included in figure 4.2.4

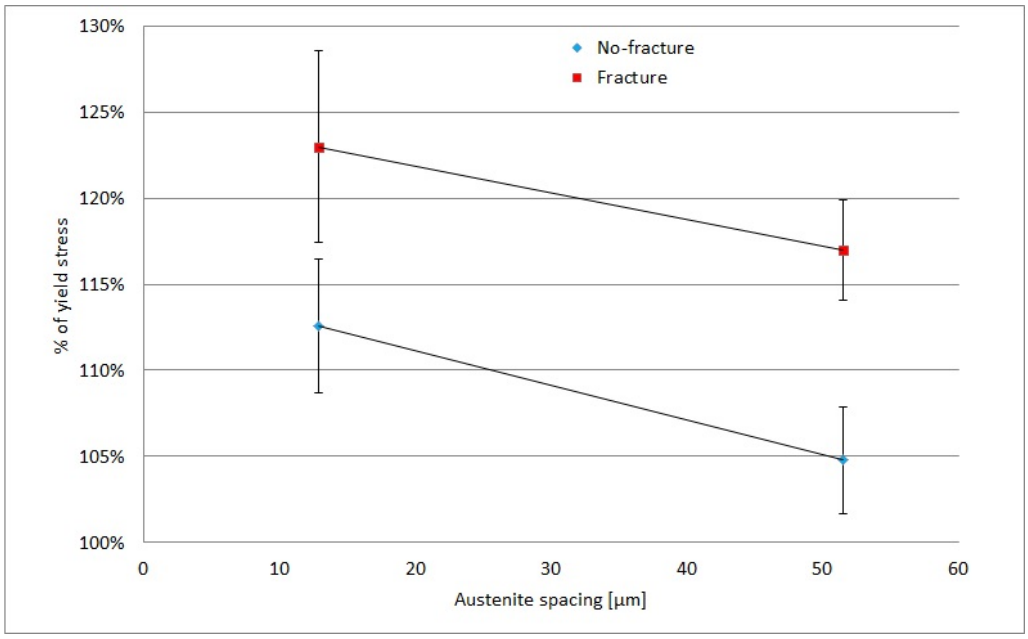


**Figure 4.2.3:** The graph shows the average stress at which the smooth samples fractured and last load without fracture (no fracture) related to austenite spacing [$\mu$m] of the materials.

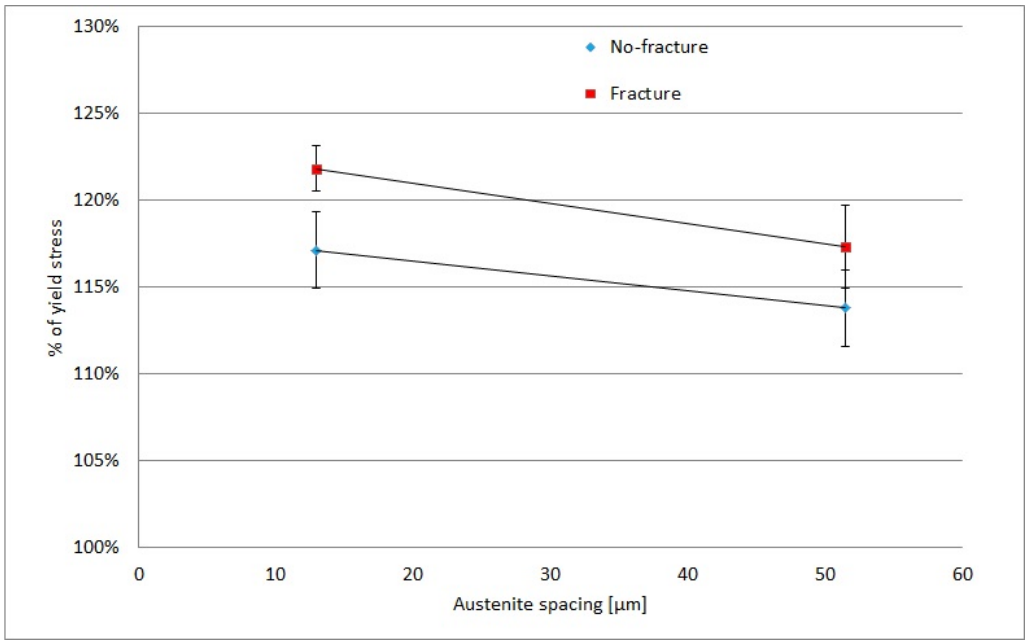


**Figure 4.2.4:** The graph shows the average stress at which the notched samples fractured and last load without fracture (no fracture) related to austenite spacing [$\mu$m] of the materials. The samples from proof ring 3111 are not included from the dataset in this graph.

### 4.2.3 Strain values

After reviewing the results on load at fracture from the HISC testing the data was converted to strain values. This was done by interpolation of the stress values with the points on the stress-strain curves from the tensile testing. These results are given in table 4.2.4 and is shown graphically in figure 4.2.5.

**Table 4.2.4:** The table shows average strain values derived from stress values in table 4.2.2 by interpolation on the stress-strain curves. Values from notched samples both with and without data from proof ring 3111 are presented. SD stands for standard deviation.

| Sample | | Forged | | HIP | |
|---|---|---|---|---|---|
| | | No-fracture | Fracture | No-fracture | Fracture |
| Smooth | Average | 0.69 % | 3.29 % | 1.74 % | 6.24 % |
| | SD | 0.11 % | 1.35 % | 0.66 % | 2.28 % |
| Notched | Average | 1.58 % | 2.84 % | 2.99 % | 4.95 % |
| all data | SD | 0.92 % | 1.80 % | 1.64 % | 2.57 % |
| Notched | Average | 1.83 % | 3.37 % | 3.62 % | 6.04 % |
| not 3111 | SD | 0.85 % | 1.57 % | 0.99 % | 0.90 % |

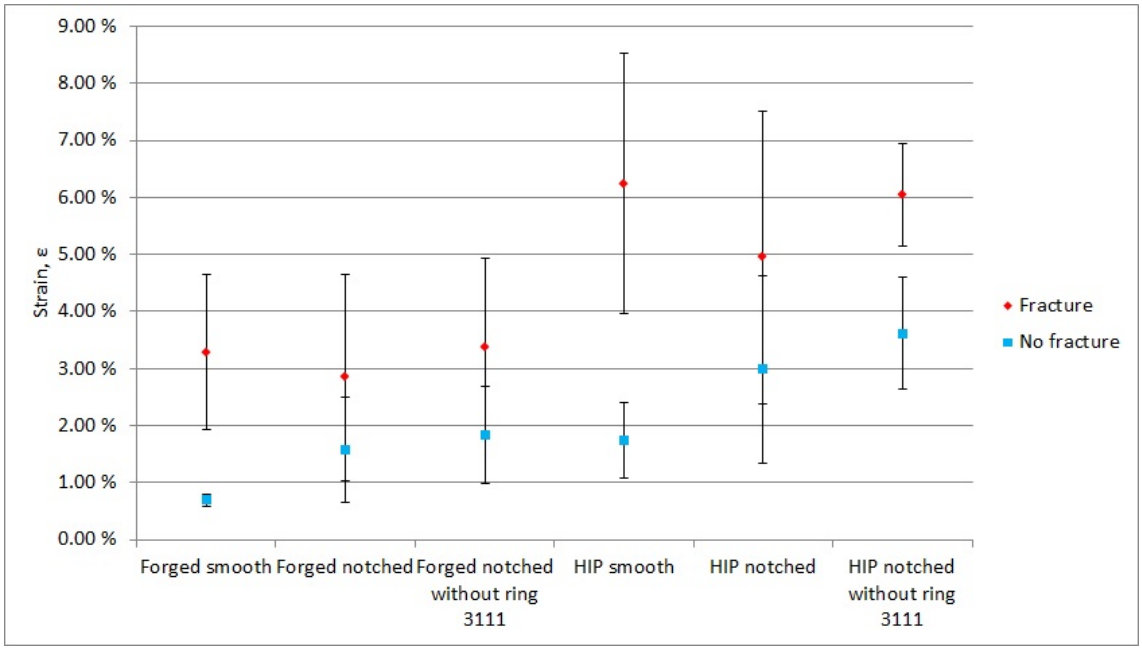


**Figure 4.2.5:** The figure show the average strain at fracture and no-fracture. The data is converted from stress values by interpolation on the stress-strain curves.

### 4.2.4 Hydrogen measurements

The amount of hydrogen measured (ppm) in the samples after HISC testing is shown in the table presented in figure 4.2.6[47].

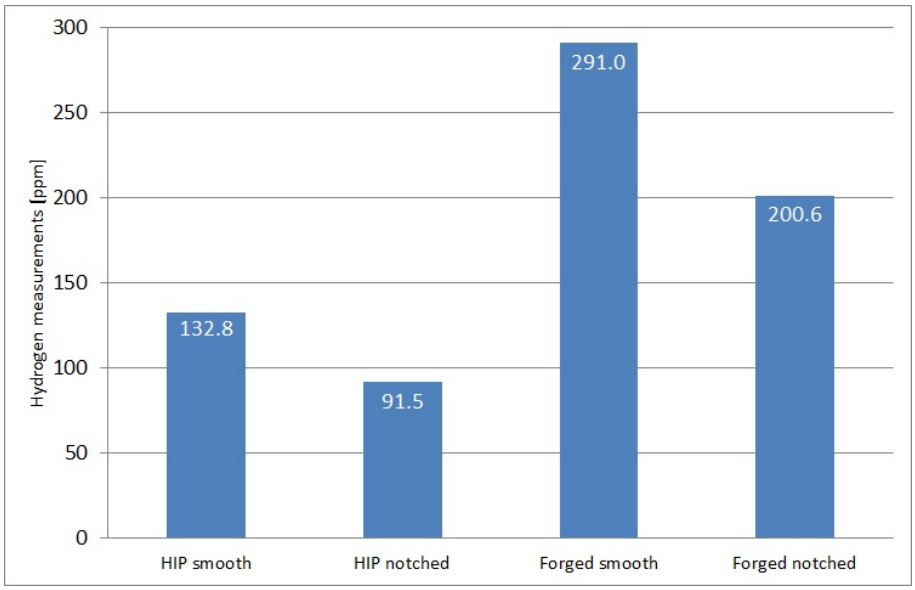


**Figure 4.2.6:** The graph shows the hydrogen measurements of both notched and smooth samples from each material after the HISC testing.

The following observations are done from the results presented in figure 4.2.6:

- The forged samples contained more than twice ($\times 2.19$) the amount in the corresponding HIP samples.
- For both materials, the smooth samples contained 1.45 times the amount of hydrogen in the notched samples.

## 4.3 Fracture surface examination

### 4.3.1 Tensile testing samples

The samples from the tensile testing, both HIP and forged showed necking before final fracture and a typical cup and cone macroscopic structure. An photography of this is seen in figure 4.3.1 and overview images from the SEM is seen in 4.3.2 and 4.3.4 for the HIP and forged material, respectively. The examination in the SEM revealed a dimpled surface over the entire surface for both materials, but the structures of the surfaces were different as the forged material had deeper voids than the HIP material. These features can be seen in figure 4.3.3 for the HIP sample, and figure 4.3.5 for the sample of forged material.

**Figure 4.3.1:** The image show samples from the tensile testing. Sample from HIP material is to the left and from the forged material is to the right.

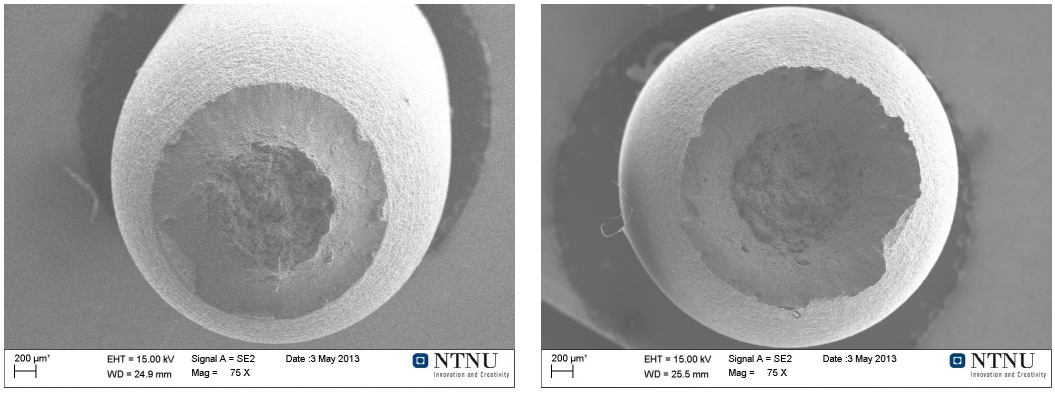


**Figure 4.3.2:** SEM images show the fracture surface from the tensile testing sample of HIP material.

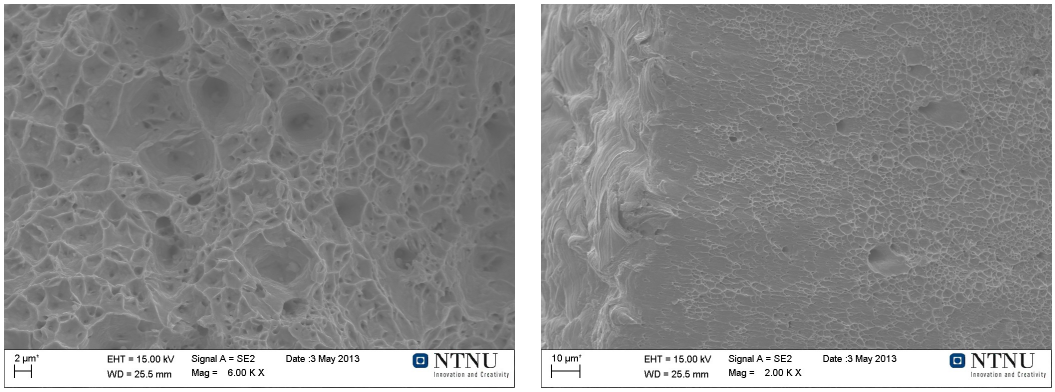


**Figure 4.3.3:** Higher magnification SEM images from HIP tensile samples. From the centre of the sample and at the edge to the left and right, respectively.

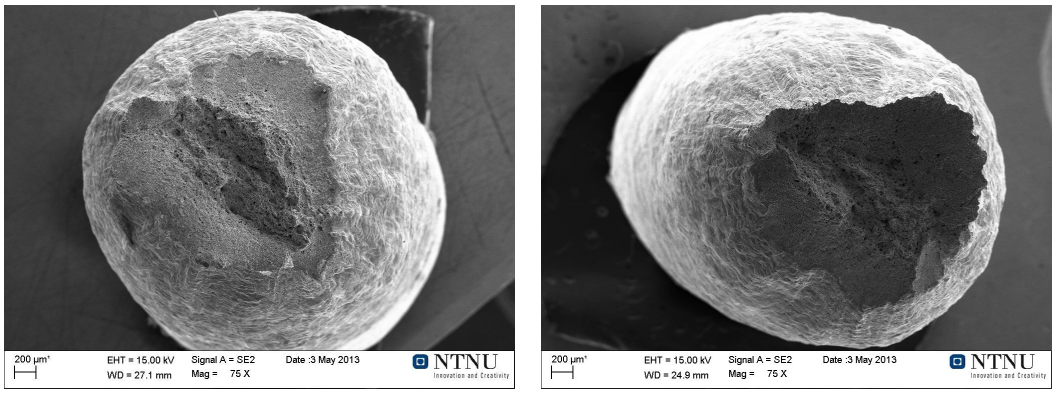


**Figure 4.3.4:** SEM images show the fracture surface from the tensile testing of forged material.

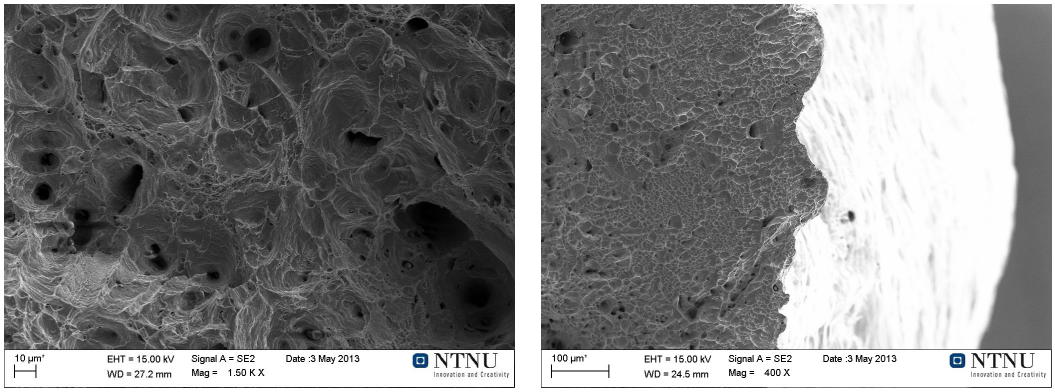


**Figure 4.3.5:** Higher magnification SEM images from forged tensile samples. From the center of the sample and at the edge to the left and right, respectively.

### 4.3.2 HISC samples - HIP material

All four HIP samples examined in the SEM, both notched and smooth, had clearly different fracture surfaces along the edge compared to the centre. This is seen in figure 4.3.6 and figure 4.3.7 for a notched and a smooth sample, respectively. A red line is drawn in the images indicating where the change from the surface at the edge to the centre is seen.

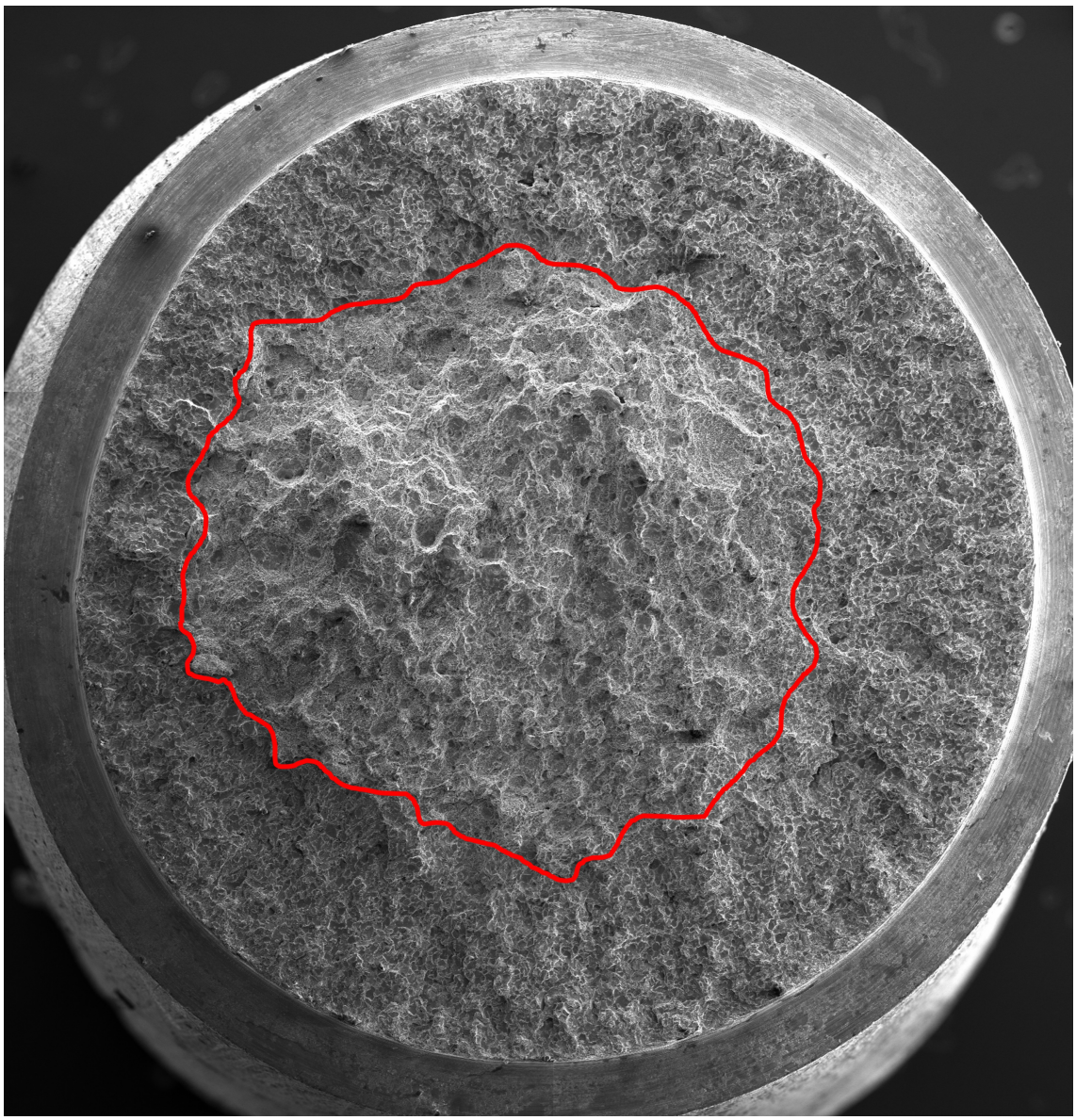

**Figure 4.3.6:** The image shows the fracture surface on a notched HIP sample after the HISC testing with a red line indicating an observed change in surface features.

The line indicating the transition from outer to inner surface features was easier to draw for the notched sample than the smooth sample as the fracture surface at the edge of the smooth sample (in the upper part in figure 4.3.7) showed a mixture of the two surface features. The smooth sample also shows deformed outer surface (up to the left in figure

4.3.7) but no clear necking as observed on the samples from the tensile testing.

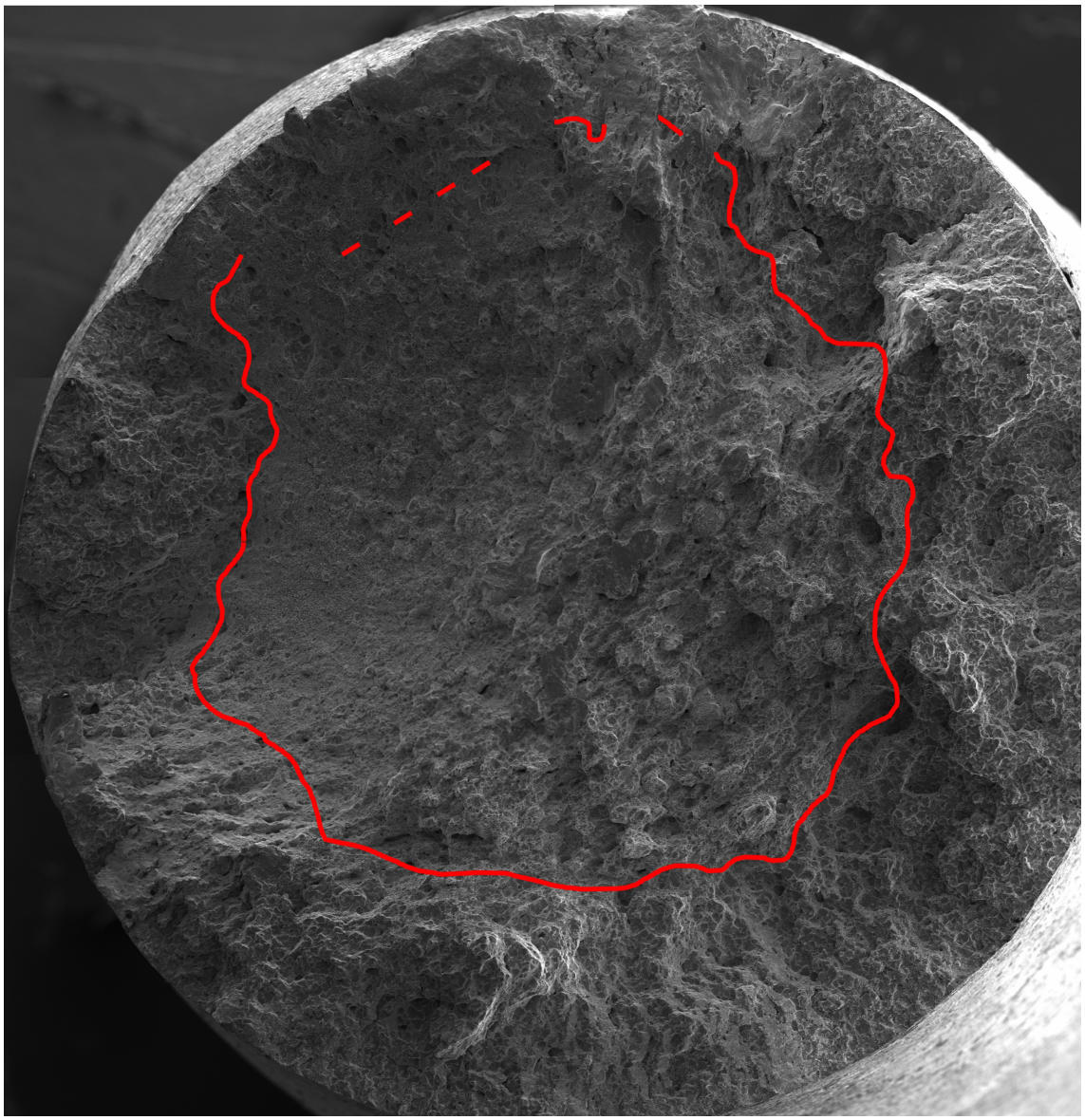

**Figure 4.3.7:** The image shows the fracture surface on a smooth HIP sample after the HISC testing with a red line indicating an observed change in surface features.

As seen in the images above, the width of the outer ring varied between 0 $\mu$m to 700 $\mu$m, but mainly between 300 $\mu$m to 500 $\mu$m. The fracture surface on the outer ring along the edge was not dimpled but consisted mainly of multifaceted surfaces, as seen in figure 4.3.8. The texture on each facet varied from quite smooth to quite rough. Lines across the facets were visible and were random in areas and seemingly organised in various manners other places. In some places the lines were aligned side by side while in other places running out from points of origin. The area marked in figure 4.3.8 is seen at higher magnifications in figure 4.3.9.

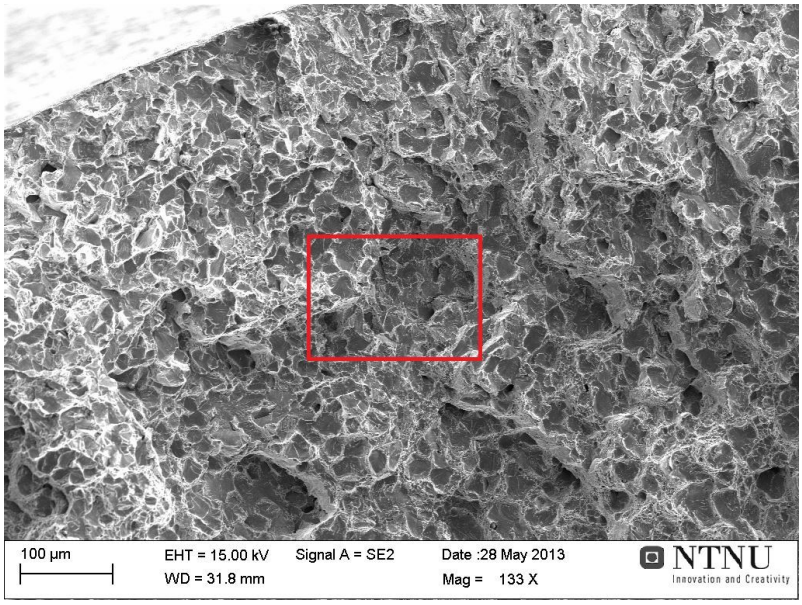


**Figure 4.3.8:** The image shows the fracture surface along the edge of a smooth HIP sample after the HISC testing.

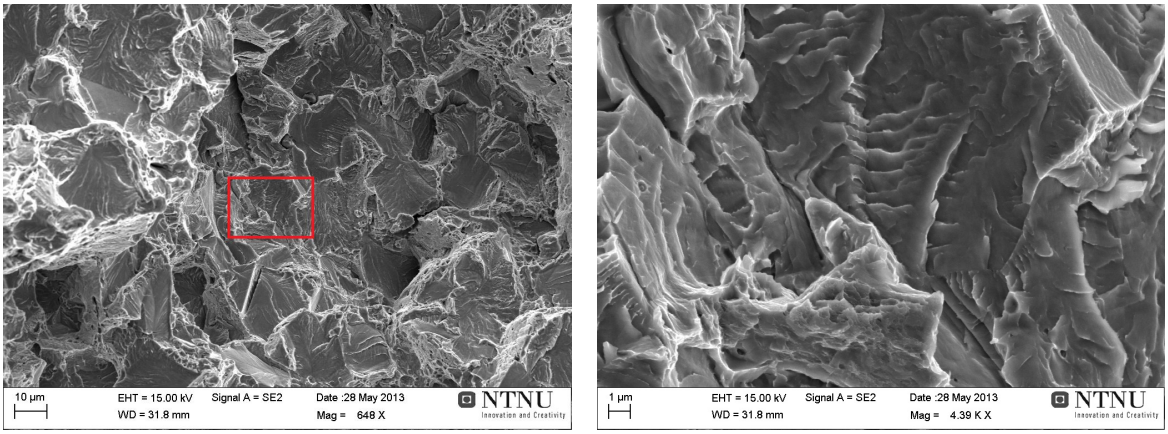


**Figure 4.3.9:** The image to the left shows the area marked in figure 4.3.8, and the image to the right is the area marked in the image to the left.

The fracture surface near the centre of the HIP samples consisted mainly of dimpled structure, but also with smaller areas with more smooth surfaces. An overview image is seen in the left image in figure 4.3.10 and the area marked there is seen in the image the right in figure 4.3.10. Here, the smooth areas described is seen down to the left and up in the middle.

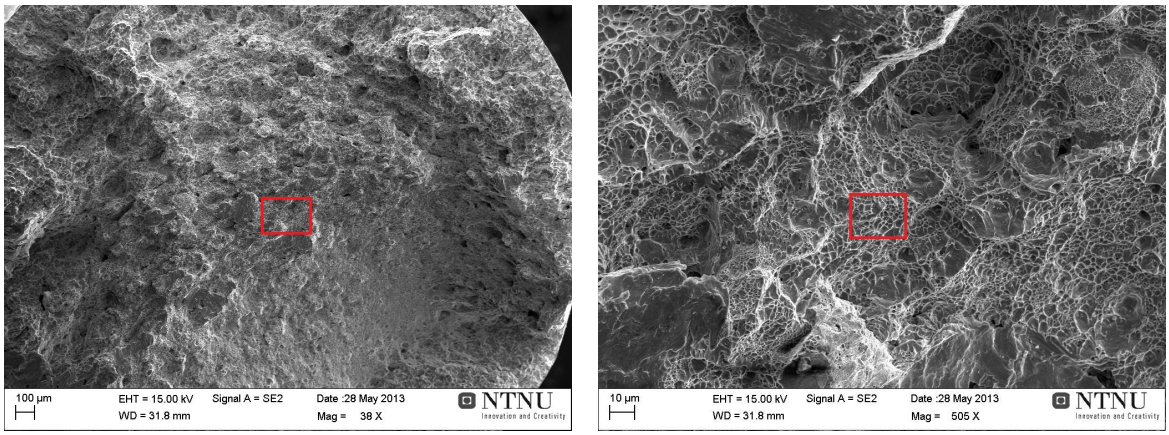


**Figure 4.3.10:** The image to the left shows the fracture surface in the middle of a smooth HIP sample after the HISC testing, and the right image show the region marked in the image to the left.

The area marked in the image to the right in 4.3.10 is seen in 4.3.11 at a higher magnification.

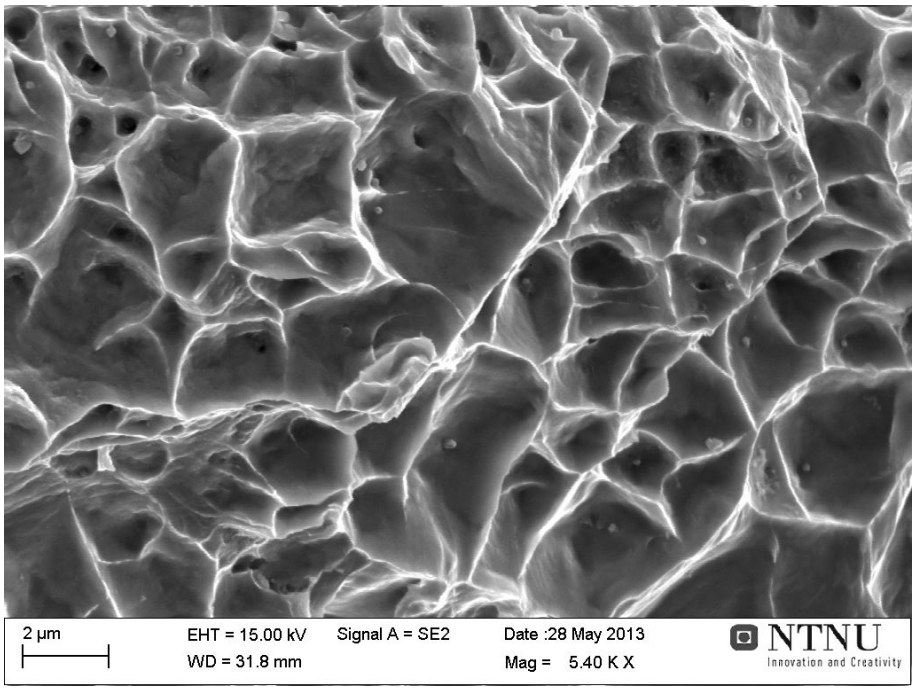


**Figure 4.3.11:** The image shows the area marked in the image to the right in figure 4.3.10.

In the transition zone between outer and inner part of the surface, a mixture of surface characteristics was observed. An image of the transition zone is shown in figure 4.3.12, with an area where the surface is dimpled is marked to the left and an area closer to the edge to the right.

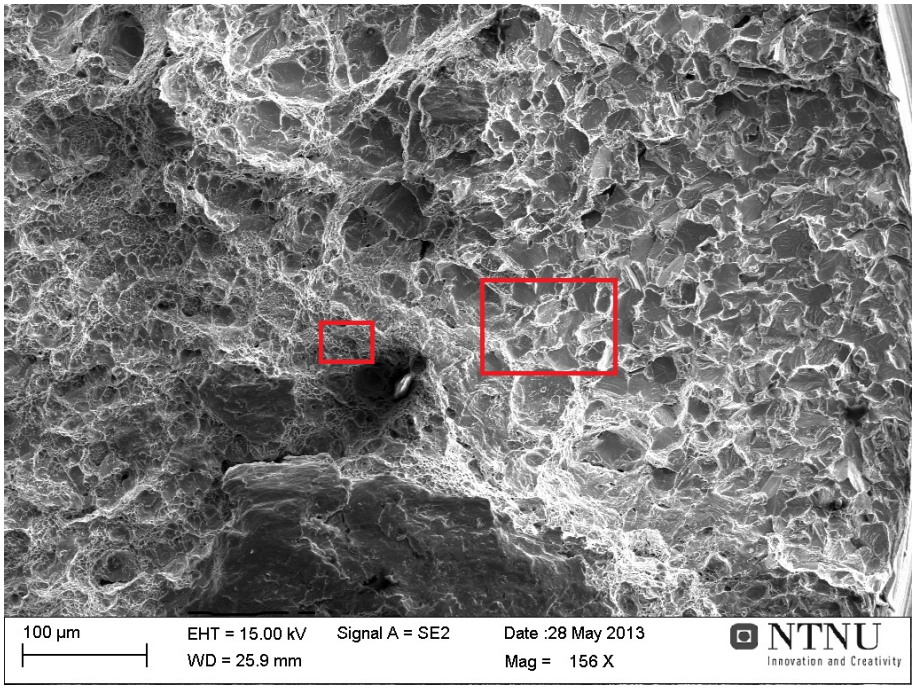


**Figure 4.3.12:** The image show the transition from outer(to the right) to inner(left) parts of the fracture surface of a smooth HIP sample after the HISC testing.

Images from the areas marked in 4.3.12 are seen in figures 4.3.13 and 4.3.14 for the inner and outer areas, respectively. The image to the right in 4.3.14 show the lines on the surface aligned side by side which were noted above.

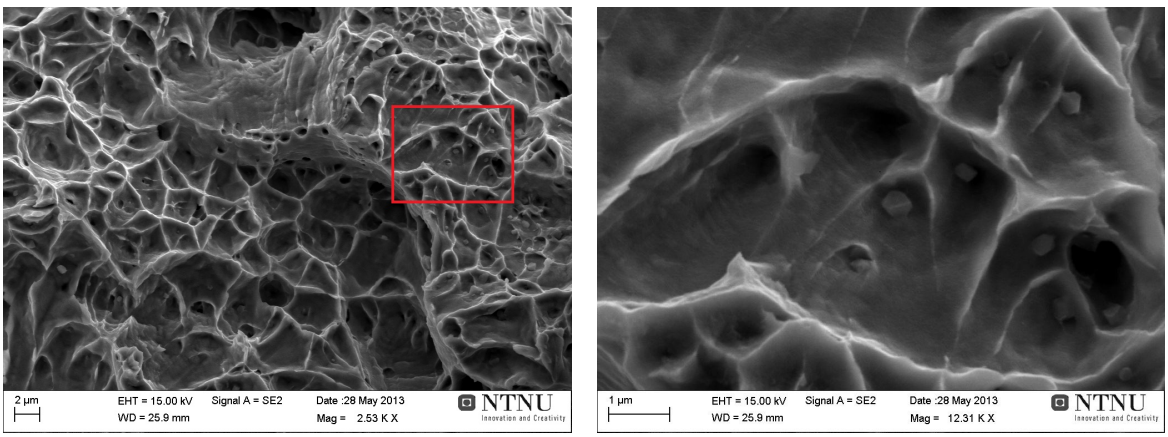


**Figure 4.3.13:** The images show the dimpled surface closer to the centre of the sample shown in figure 4.3.12. The left image is from the region marked to the left in figure 4.3.12 and the right image is the region marked in the left image.

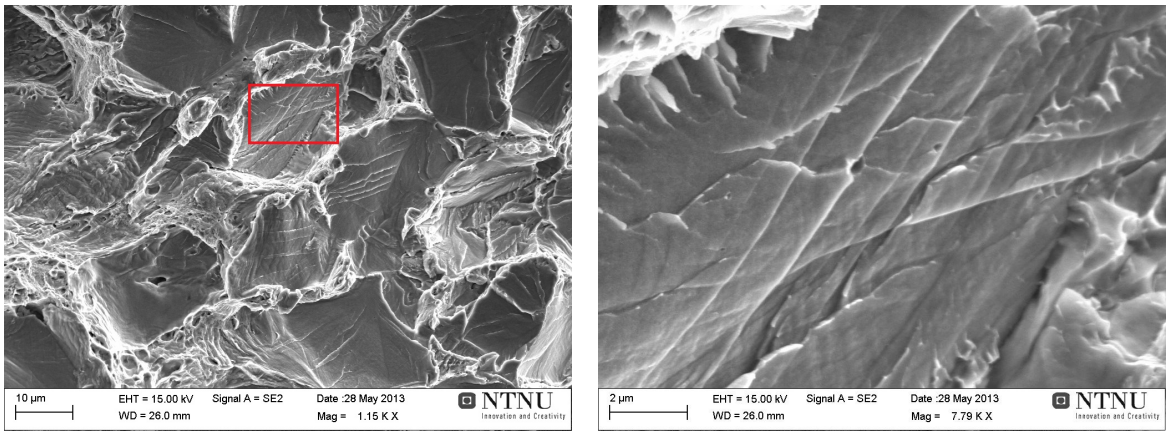


**Figure 4.3.14:** The images show the surface closer to the edge of the sample shown in figure 4.3.12. The image to the left is from the region marked to the right in figure 4.3.12 and the right image is the region marked in the left image.

Cracking along the sides was observed on all the smooth samples. An image of this is shown in 4.3.15.

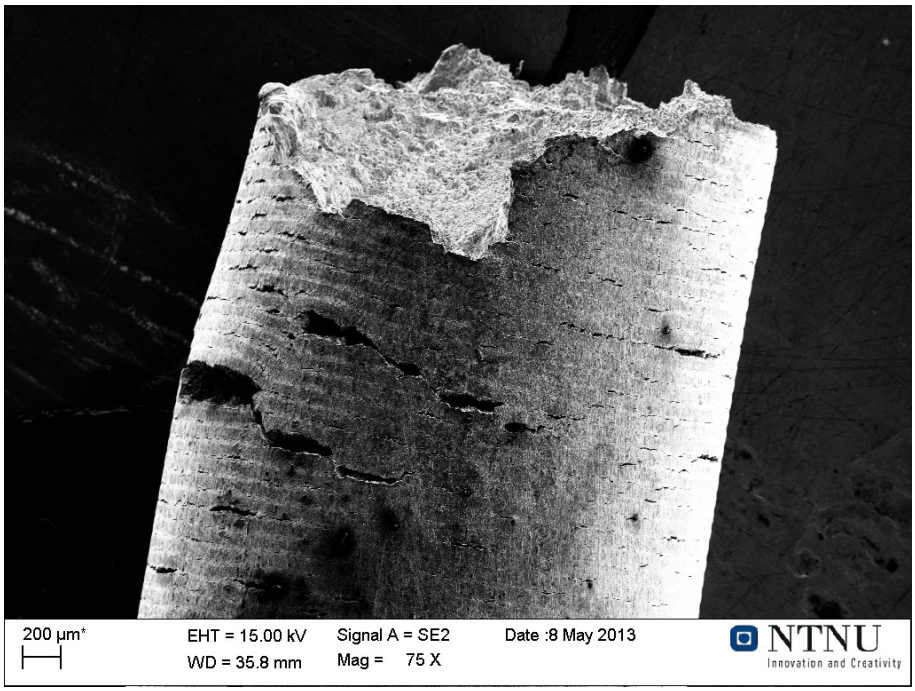


**Figure 4.3.15:** The image show cracks on the side of a smooth HIP sample after the HISC tests.

The side of a notched sample is seen in figure 4.3.16 and a section of this is seen in figure 4.3.17. The image in the figure 4.3.17 shows a small cracks in the notch which has not propagated and parts of the fracture surface partially detached during fracture.

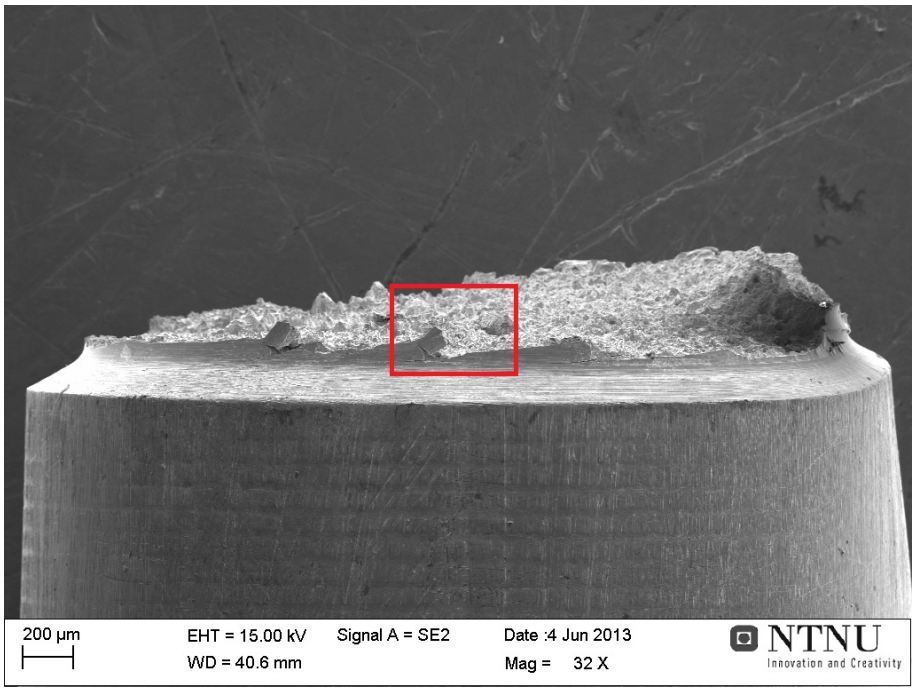


**Figure 4.3.16:** The image shows the side of a notched HIP sample after the HISC tests.

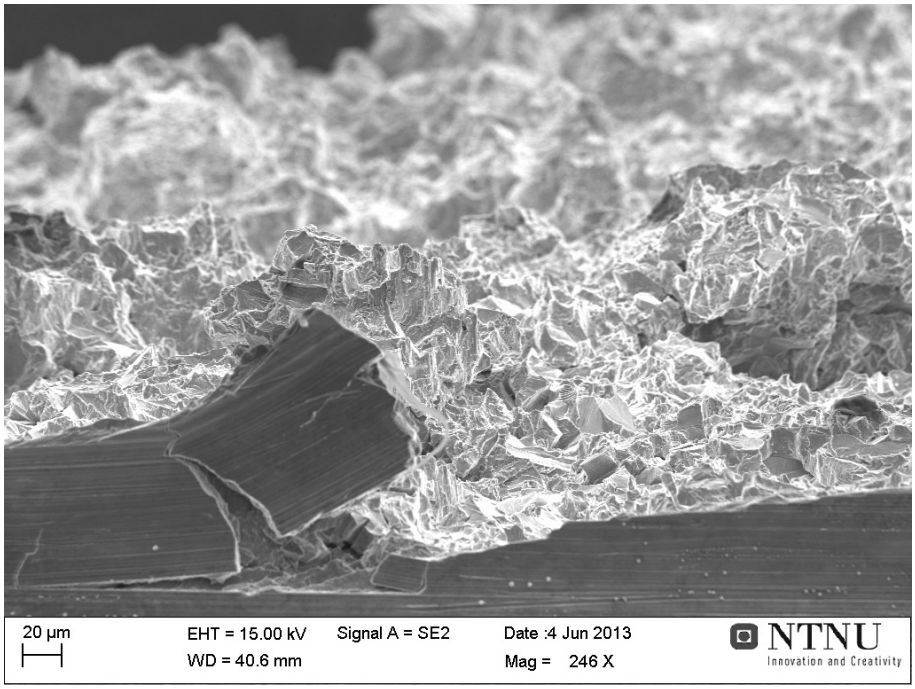


**Figure 4.3.17:** The image shows the section which is marked in 4.3.16 at higher magnification.

Images of the entire fracture surfaces of notched and smooth HIP samples are shown in figure 4.3.18 and 4.3.19, respectively. One of the notched samples was deformed on one side and not perfectly circular.

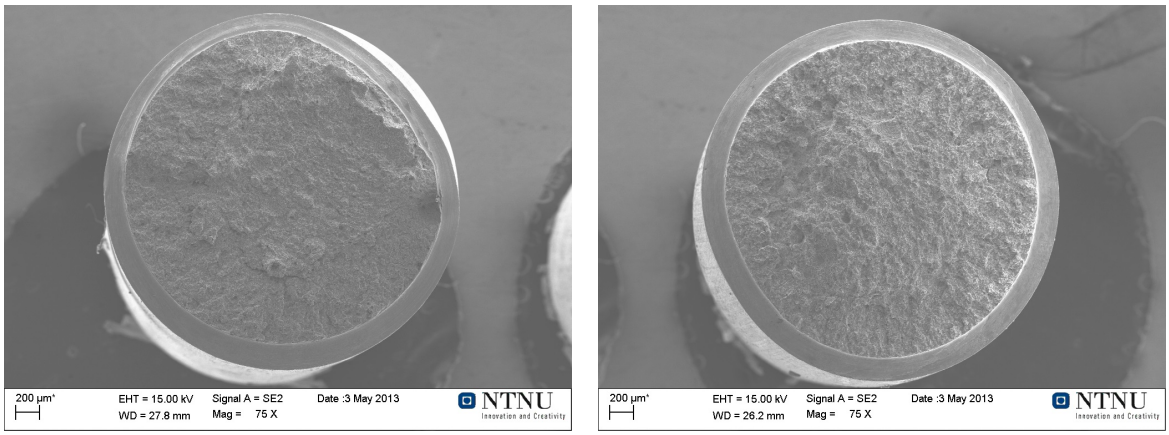


**Figure 4.3.18:** SEM images showing the fracture surface of two of the notched HISC samples of HIP material. The sample to the left is deformed along the edge.

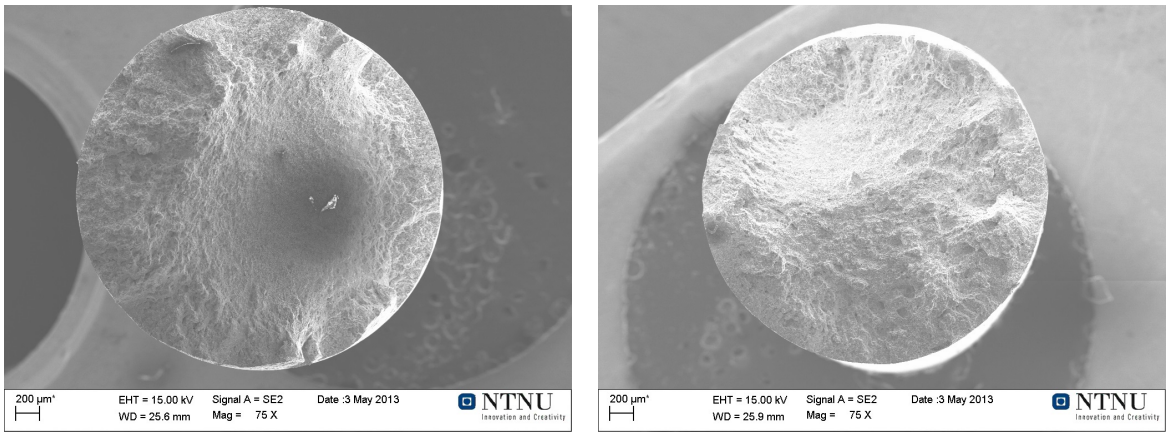


**Figure 4.3.19:** SEM images showing the fracture surface of two of the smooth HISC samples of HIP material.

### EDS analysis

The transition zone between the outer and inner area on one of the smooth HIP samples is seen in figure 4.3.20 with both smooth(flat) and dimpled areas. EDS analysis was employed on three sets of areas of dimpled and smooth structure to attempt to find the relative amount of Chromium in the different parts of the surface. The areas within each set were of approximately the same size. Two of the areas investigated, one dimpled and

one smooth, are depicted in the image in figure 4.3.20. The amount of Chromium detected in each area is given in table 4.3.1.

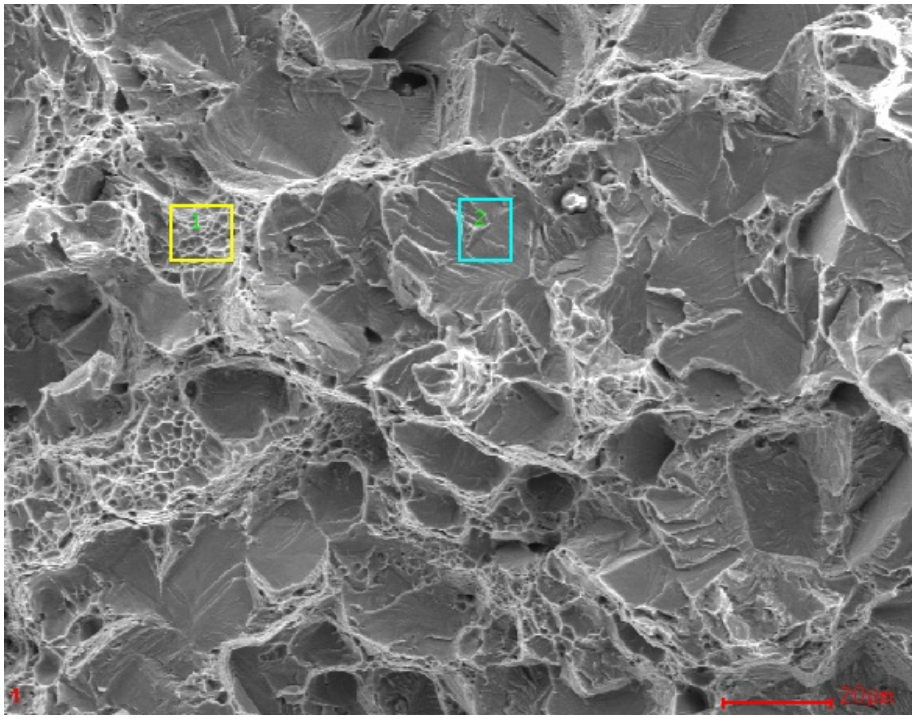


**Figure 4.3.20:** The image shows a section of a smooth HIP sample with two of the areas for EDS analysis marked.

**Table 4.3.1:** The table shows the results from the EDS analysis in wt% of Chromium in each area.

| Set | Dimpled | Smooth |
|---|---|---|
| 1 | 27.01% | 27.12% |
| 2 | 27.23% | 27.82% |
| 3 | 26.47% | 29.81% |

### 4.3.3 HISC samples - forged material

When comparing the fracture surfaces of the two materials, it was clear that the two distinct areas related to distance from sample surface seen on the samples of HIP material was not present on the samples of forged material. The fracture surfaces of forged material were more similar across the cross section. It was noted, however, that the texture on the surface of samples of forged material was coarser. This is seen when comparing in the images in figures 4.3.21 and 4.3.22 with the corresponding images from HIP material (figures 4.3.19 and 4.3.18).

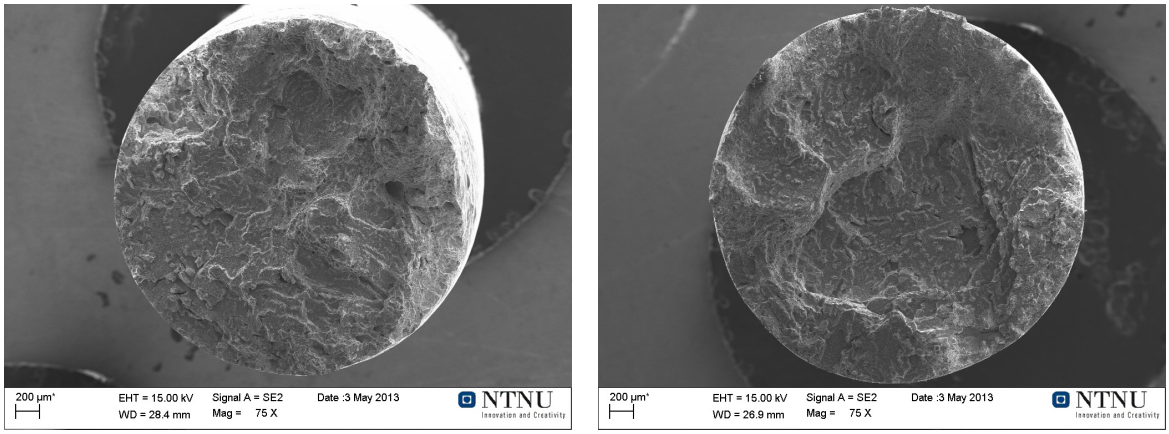


**Figure 4.3.21:** SEM images showing the fracture surface of two of the smooth HISC samples of the forged material.

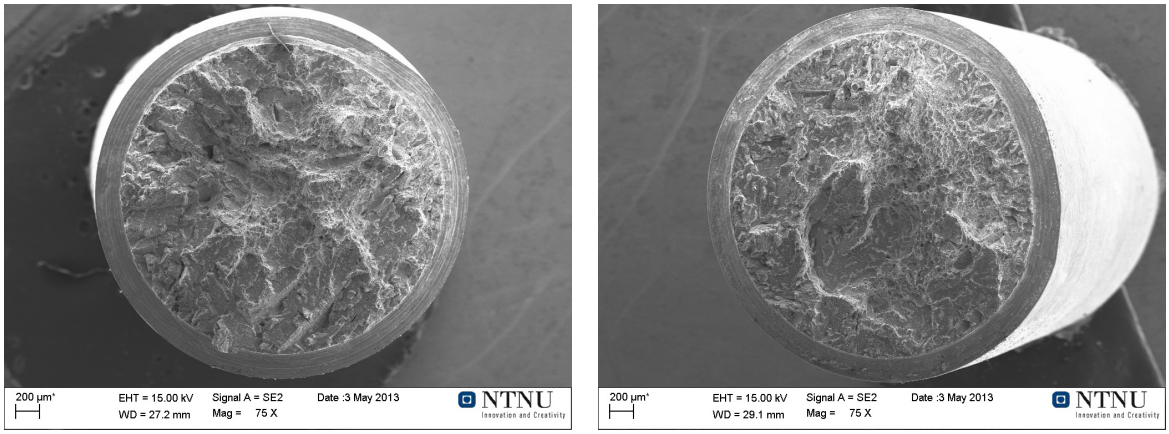


**Figure 4.3.22:** SEM images showing the fracture surface of two of the notched HISC samples of the forged material.

The majority of area on the surfaces showed multifaceted flat areas as seen in figure 4.3.23.

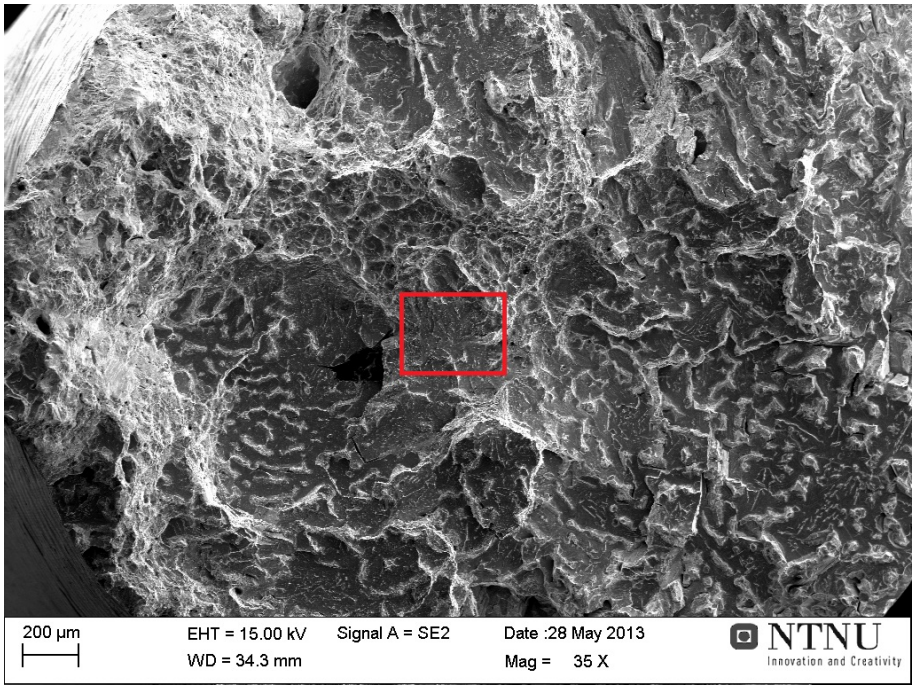


**Figure 4.3.23:** The image shows an area of a smooth forged sample.

The area marked in 4.3.23 is shown at increasing magnifications in figure 4.3.24 and figure 4.3.25.

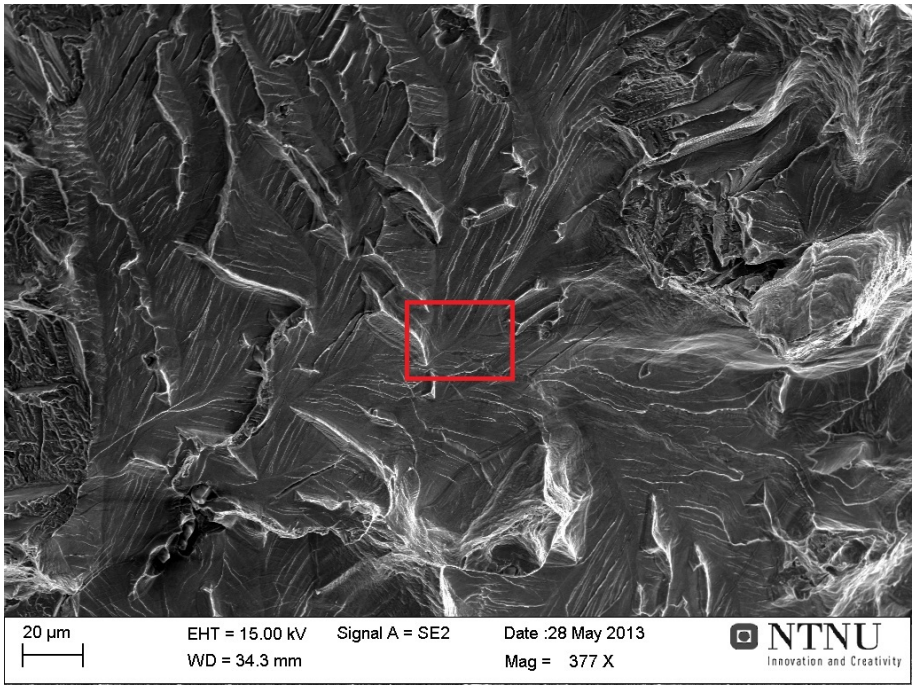


**Figure 4.3.24:** The image shows the area marked in figure 4.3.23.

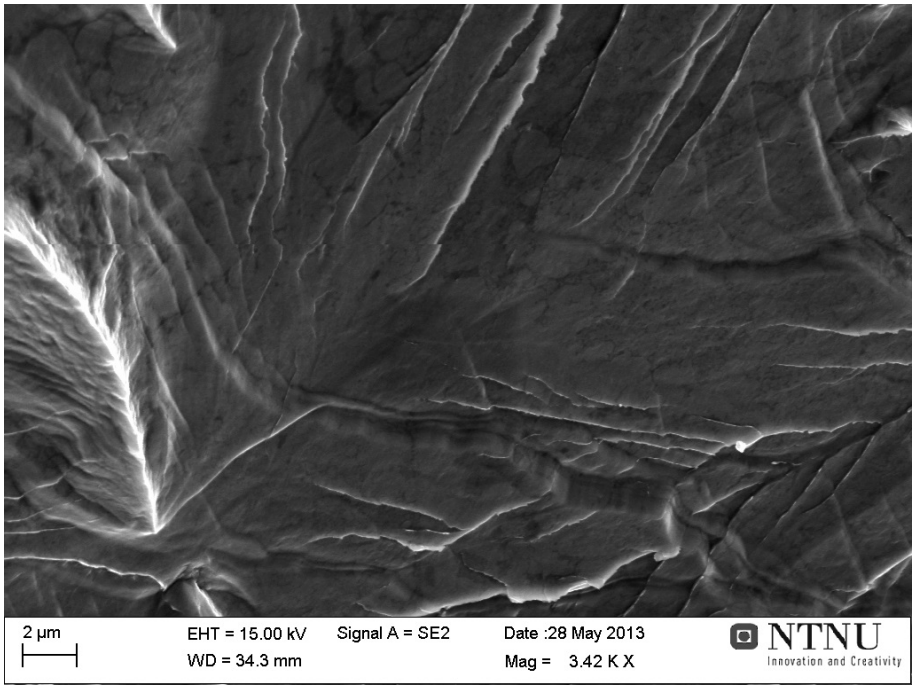


**Figure 4.3.25:** The image shows the area marked in figure 4.3.24.

Along with the multifaceted flat surfaces, there were elements of dimpled structure both as separate areas and embedded in the multifaceted areas. The image in figure 4.3.26 show how the mixture of features appeared on the fracture surfaces on the forged samples. Cracks of various sizes and shapes are also visible.

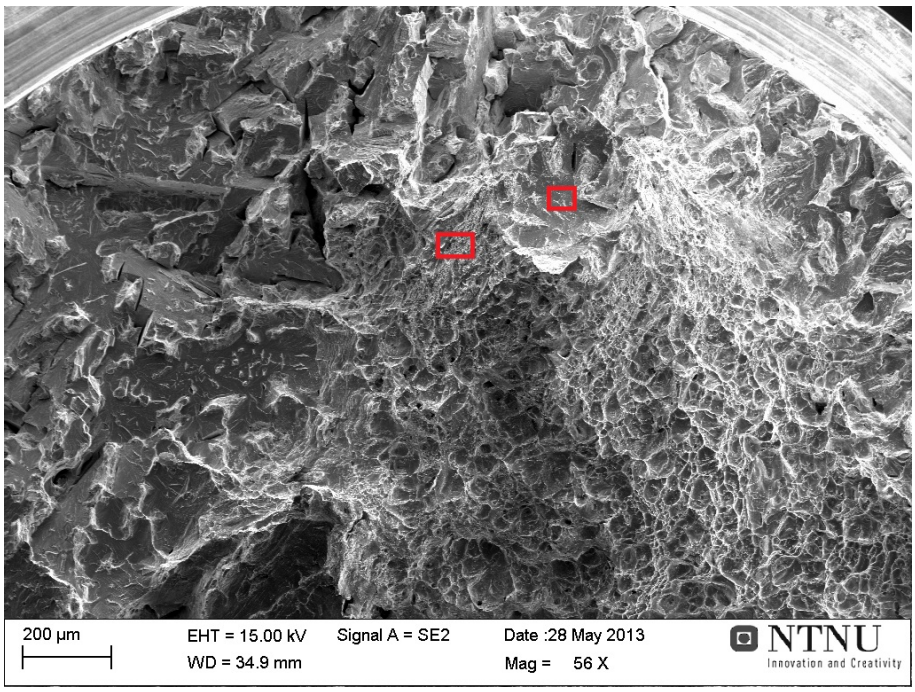


**Figure 4.3.26:** The image shows a notched forged sample from the HISC testings with a mixture of fracture modes.

The area marked to the right in figure 4.3.26 is shown in 4.3.27 and the area to the left is shown in figure 4.3.28.

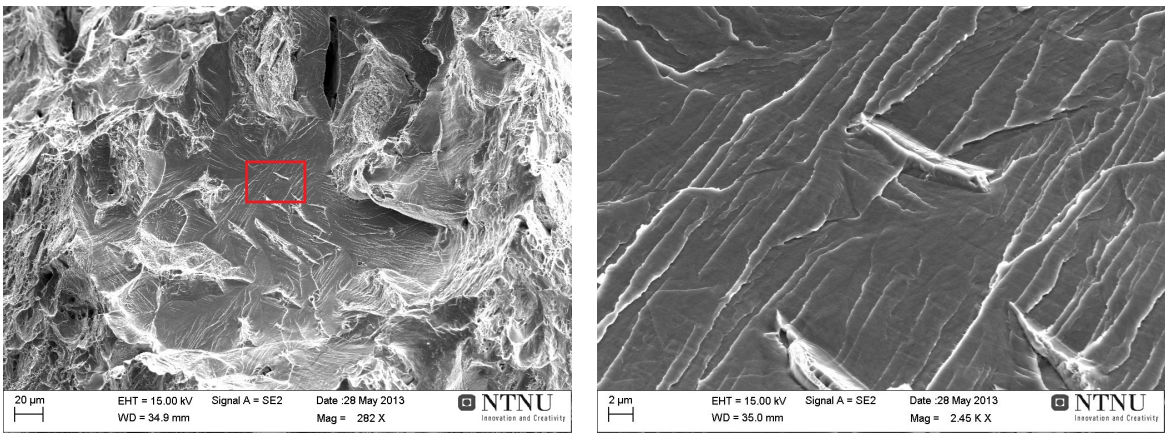


**Figure 4.3.27:** The image to the left shows the area marked to the right in figure 4.3.26, and the image to the right is the area marked in the image to the left.

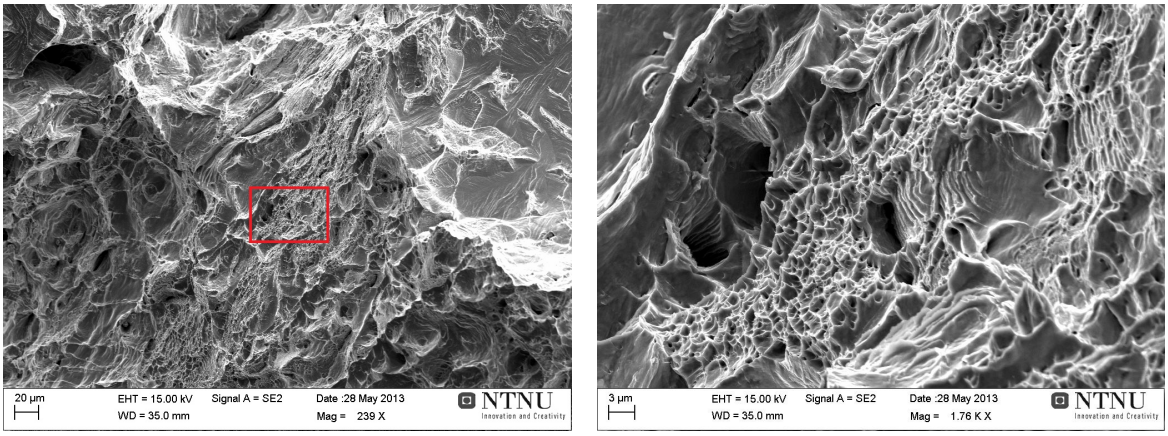


**Figure 4.3.28:** The image to the left shows the area marked to the left in figure 4.3.26, and the image to the right is the area marked in the image to the left.

The images that follow show the sides of the fractured HISC samples of forged material. Firstly, the side of a notched sample is seen in figure 4.3.29 and a section of this is seen in figure 4.3.30. The image in the figure 4.3.30 show similar cracks in the notch and parts of the fracture surface partially detached as seen on the HIP samples.

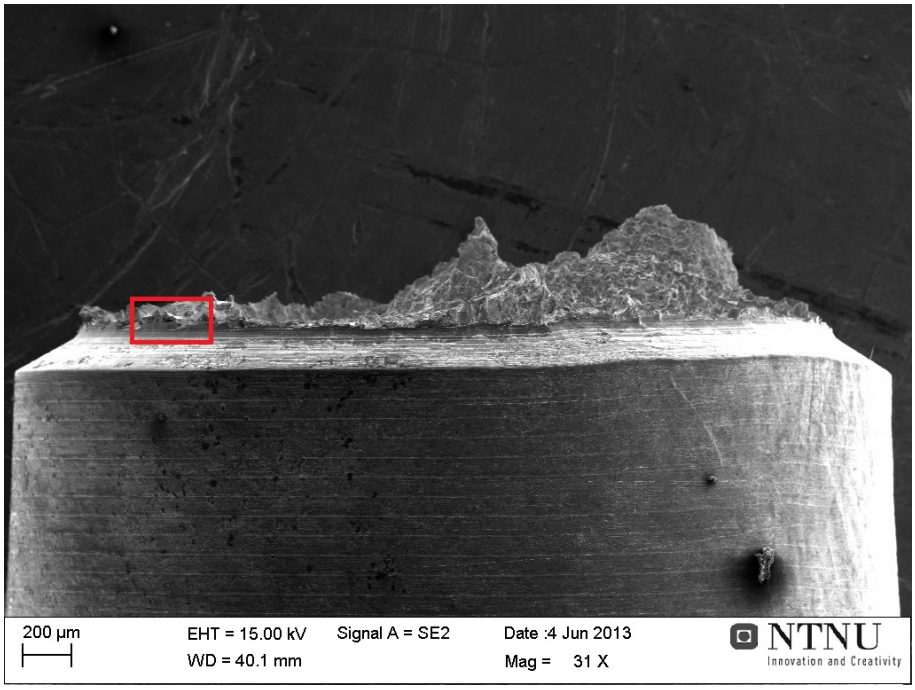


**Figure 4.3.29:** The image shows the side of a notched forged HISC sample.

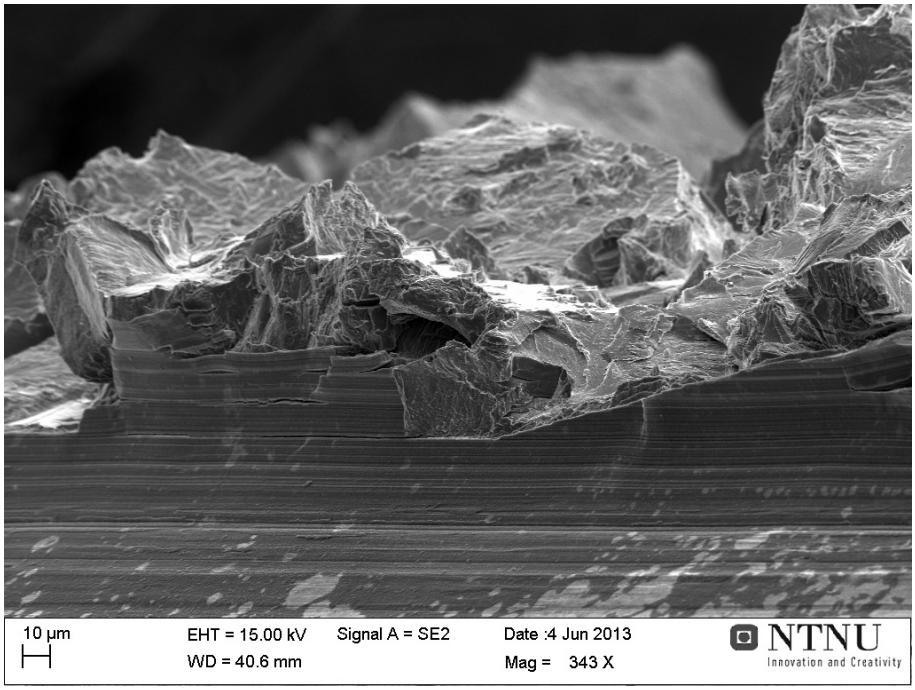


**Figure 4.3.30:** The image shows the section marked in 4.3.29 at higher magnification.

The image shown in figure 4.3.31 shows cracks along the side of a smooth sample of forged material similar to the ones seen on the HIP material. A narrowing in at one side is also observed (to the right) but not around the whole circumference like the necking observed on the tensile samples.

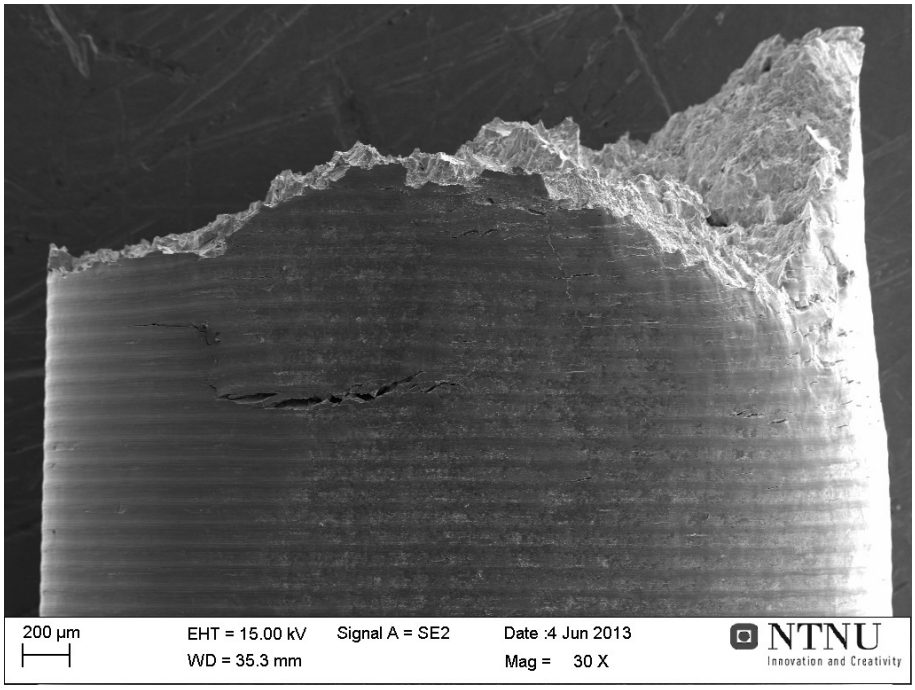


**Figure 4.3.31:** The image shows cracks along the side of a smooth forged HISC sample.

## 4.4 Microstructural analysis

EBSD images are presented for both HIP and forged material. All images presented are partitions of CI $\geq$ 0.05 after grain CI standardization.

### 4.4.1 HIP material

Scans of the HIP material of 100 $\mu$m $\times$ 100 $\mu$m and 200 $\mu$m $\times$ 200 $\mu$m areas were done. The scan quality parameters of the three most successful scans are given in table 4.4.1 with the ferrite and austenite fractions measured during analysis. Images developed from scan 2 from table 4.4.1 are presented below in order to compare with the forged material later (200 $\mu$m $\times$ 200 $\mu$m areas are smallest which are presented of the forged material). A phase map is shown in figure 4.4.1 below followed by an inverse pole figure (IPF) map of both phases in figure 4.4.2.

**Table 4.4.1:** The table lists the scan quality parameters (before clean-up) from the three most successful EBSD scans of HIP material along with ferrite and austenite fractions.

| Scan no. | Area [$\mu$m $\times$ $\mu$m] | CI | IQ | Fit | Ferrite [%] | Austenite [%] |
|---|---|---|---|---|---|---|
| 1 | 100 $\times$ 100 | 0.71 | 244 | 0.7 | 49.2 | 50.8 |
| 2 | 200 $\times$ 200 | 0.68 | 198 | 0.8 | 48.4 | 51.6 |
| 3 | 100 $\times$ 100 | 0.54 | 251 | 1.16 | 47.4 | 52.6 |
| Average | | | | | 48 | 52 |

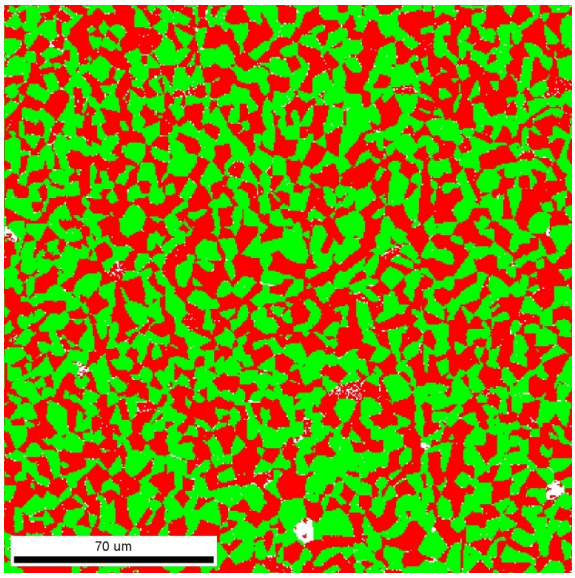


**Figure 4.4.1:** The image shows the phase map of an EBSD scan of a 200 $\mu$m $\times$ 200 $\mu$m area of the HIP material. Green is austenite and red is ferrite.

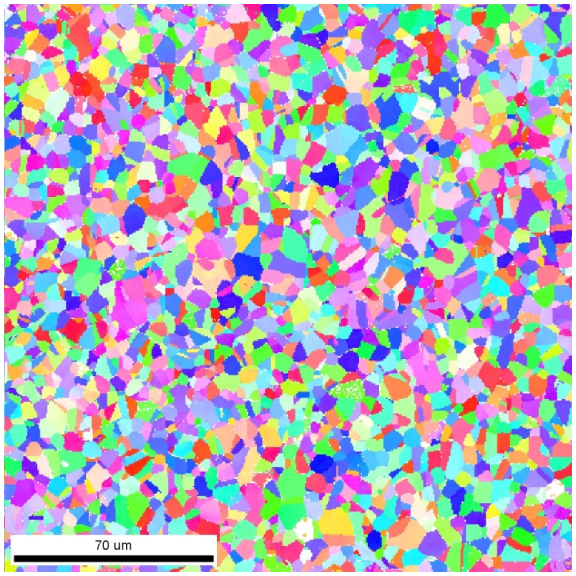


**Figure 4.4.2:** The image shows the IPF map of an EBSD scan of a 200 $\mu$m $\times$ 200 $\mu$m area of the HIP material.

The same kind of map as shown in figure 4.4.2 (IPF map) is shown in figure 4.4.3 for each phase separately.

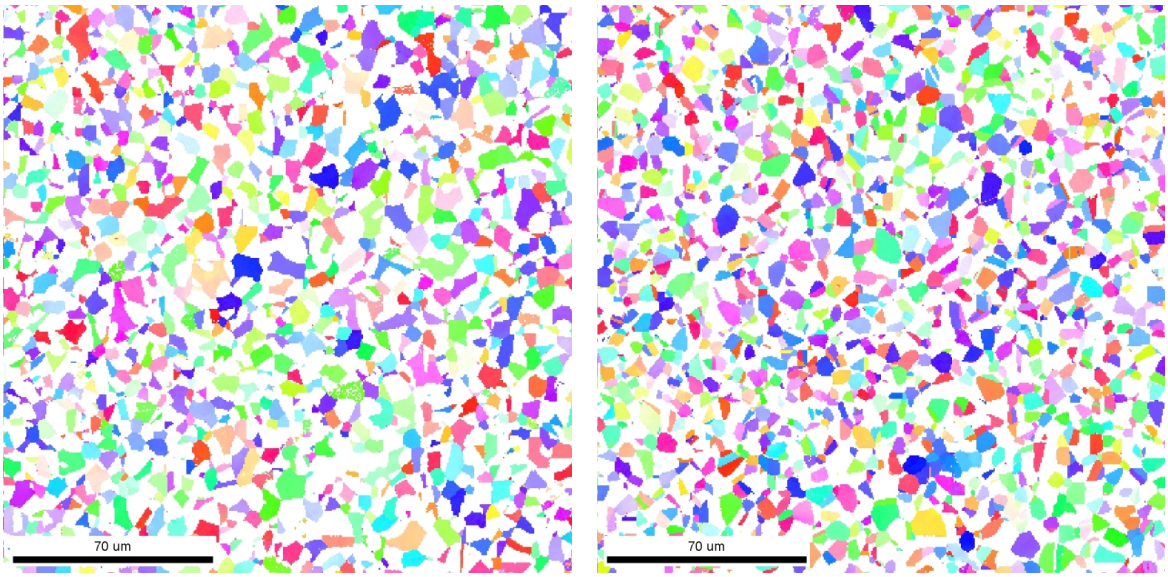


**Figure 4.4.3:** The images show the IPF maps of the EBSD scan in figure 4.4.2 above of ferrite alone to the left and austenite alone to the right.

As seen in the IPF maps of both phases in figure 4.4.3, the orientation of the grains appear random. To further investigate this observation, pole figure plots of each phase from the same scan is presented in figure 4.4.4.

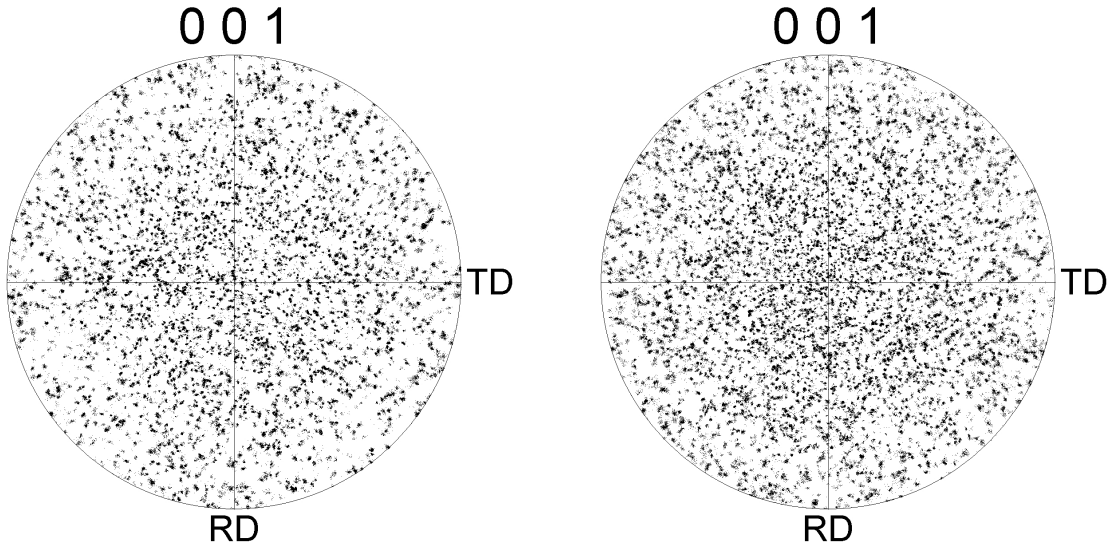


**Figure 4.4.4:** Pole figure plots from an EBSD scan of the 200 $\mu$m $\times$ 200 $\mu$m area of the HIP material. The plot of ferrite and austenite is to the left and right, respectively.

### 4.4.2 Forged material

From the forged material, scans corresponding to both cross-section and longitudinal direction are shown. Parameters for scan quality are given in table 4.4.2 along with the ferrite and austenite fractions from the larger scans. It was found that scans of 100 $\mu$m $\times$ 100 $\mu$m and 200 $\mu$m $\times$ 200 $\mu$m areas were too small to give representative images of the microstructure of the forged material. Scans of 1 mm $\times$ 1 mm areas were therefore conducted and are presented here to show the microstructure (scan no. 3 and 6 in table 4.4.2). Scans of 200 $\mu$m $\times$ 200 $\mu$m areas (scan no. 2 and 5 table 4.4.2) are shown for comparison to EBSD scans of HIP material.

**Table 4.4.2:** The table show the scan quality parameters (before clean-up) from the three most successful EBSD scans of HIP material along with ferrite and austenite fractions.

| Scan no. | Direction | Area [$\mu$m $\times$ $\mu$m] | CI | IQ | Fit | Ferrite [%] | Austenite [%] |
|---|---|---|---|---|---|---|---|
| 1 | Longitudinal | 100 $\times$ 100 | 0.51 | 254 | 1.03 | | |
| 2 | | 200 $\times$ 200 | 0.6 | 227 | 0.93 | | |
| 3 | | 1000 $\times$ 1000 | 0.5 | 82 | 1.03 | 52.0 | 48.0 |
| 4 | Cross-section | 100 $\times$ 100 | 0.77 | 231 | 0.73 | | |
| 5 | | 200 $\times$ 200 | 0.71 | 197 | 0.82 | | |
| 6 | | 1000 $\times$ 1000 | 0.57 | 78 | 1 | 54.0 | 46.0 |
| Averages | | | | | | 53.0 | 47.0 |

### Cross-sections

The images that follow are from areas corresponding to the cross-section of the HISC samples, oriented with the thickness direction of the forging horizontally and the circumferential direction vertically. This configuration also applies to the pole figure plots. Phase maps from scans of small and large areas are presented in figure 4.4.5 and figure 4.4.6, respectively.

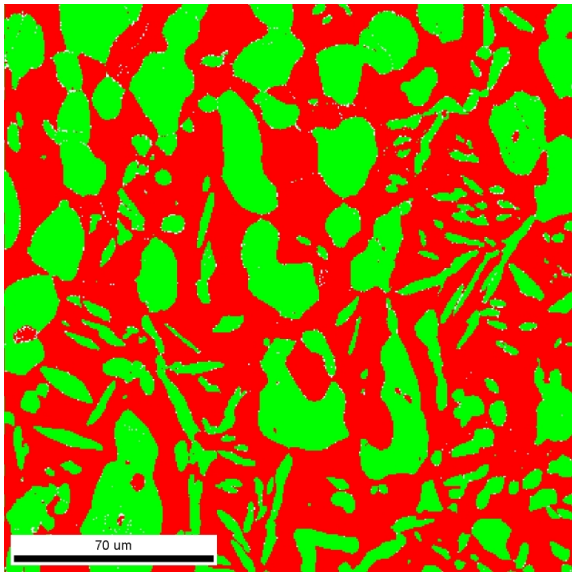


**Figure 4.4.5:** The image shows the phase map of an EBSD scan of a 200 $\mu$m $\times$ 200 $\mu$m area of the forged sample from a cross-section scan. Green is austenite and red is ferrite.

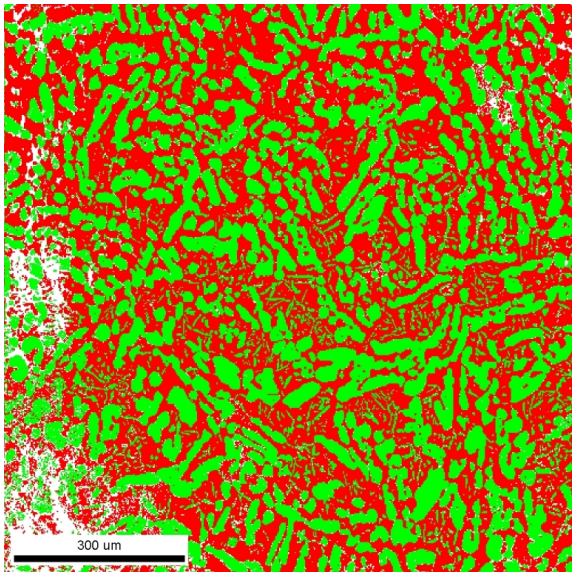


**Figure 4.4.6:** The image shows the phase map of an EBSD scan of a 1000 $\mu$m $\times$ 1000 $\mu$m area of the forged sample from a cross-section scan. Green is austenite and red is ferrite.

The inverse pole figure (IPF) maps from the same area as seen in figure 4.4.5 is given in figure 4.4.7 for both phases and for each phase separately in figure 4.4.8.

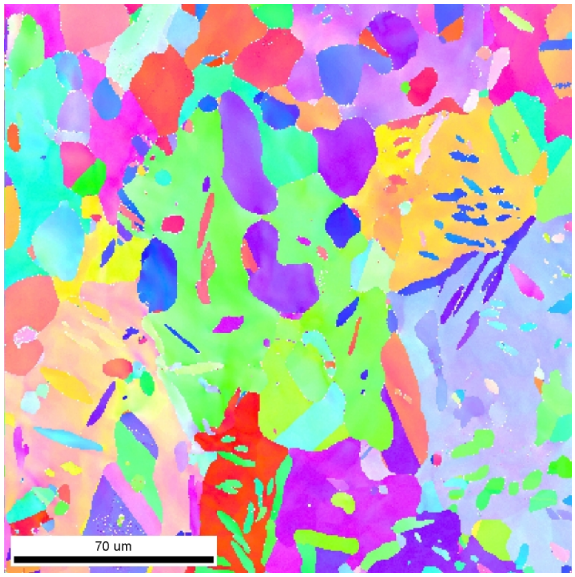


**Figure 4.4.7:** The image shows the IPF map of an EBSD scan of a 200 $\mu$m $\times$ 200 $\mu$m area of the forged sample from a cross-section scan.

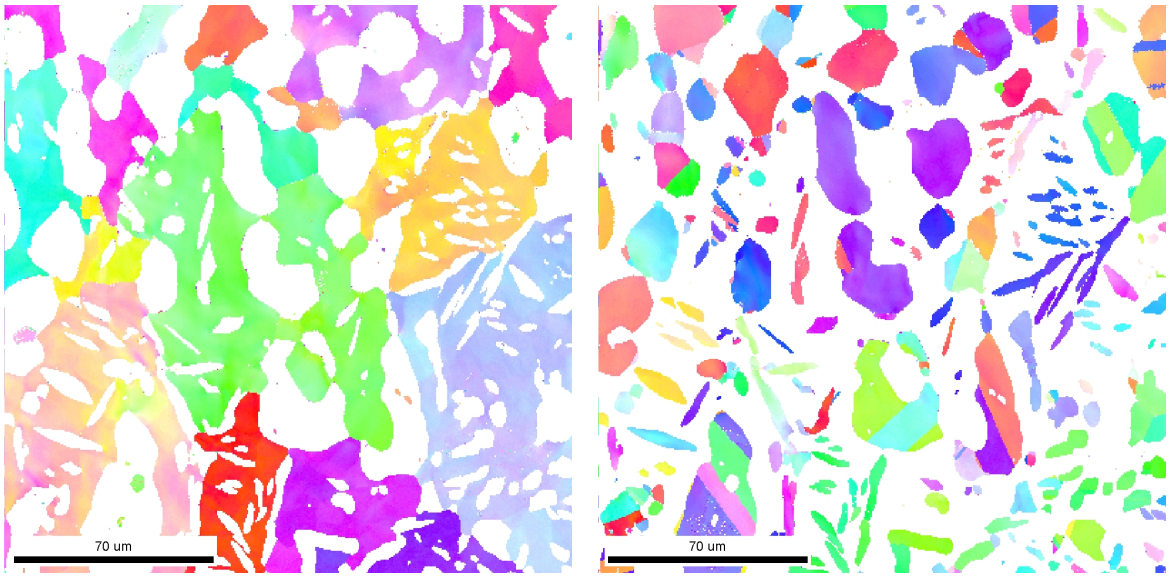


**Figure 4.4.8:** The images show the IPF maps of the EBSD scan in figure 4.4.7 for the ferrite and austenite phase separately to the left and right, respectively.

The inverse pole figure (IPF) maps from the same area as seen in figure 4.4.6 is given in figure 4.4.9 for both phases and for each phase separately in figure 4.4.10.

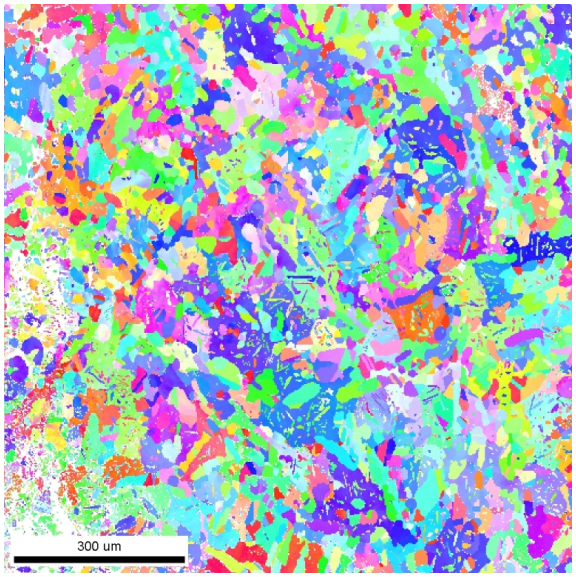


**Figure 4.4.9:** The image shows the IPF map of an EBSD scan of a 1000 $\mu$m $\times$ 1000 $\mu$m area of the forged sample from a cross-section scan.

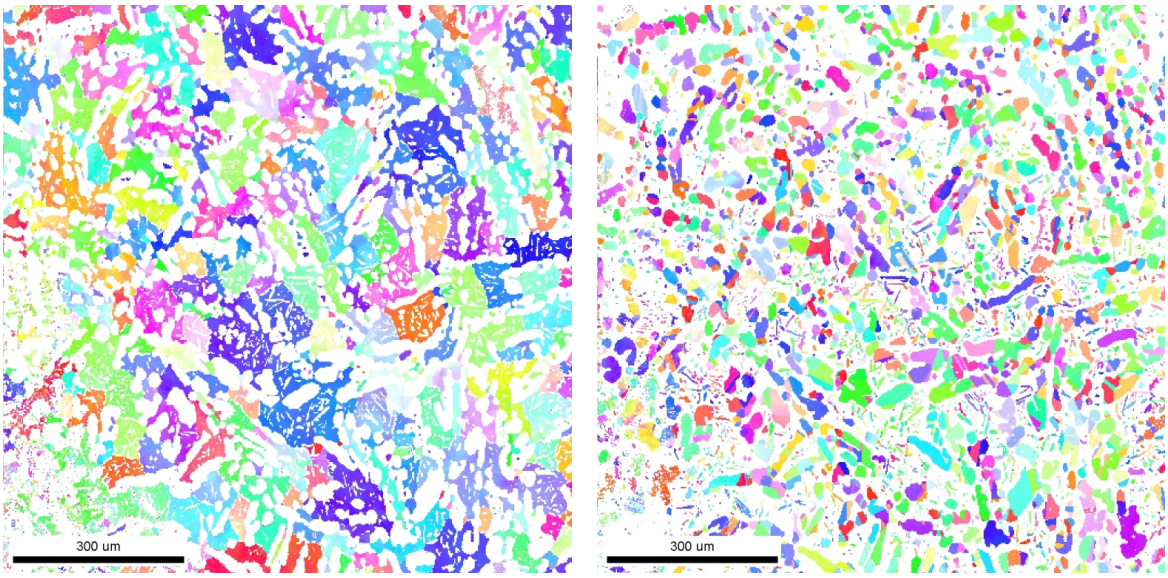


**Figure 4.4.10:** The images show the IPF maps of the EBSD scan in figure 4.4.9 for the ferrite and austenite phase separately to the left and right, respectively.

The pole figure plots from each phase of the scan of 1000 $\mu$m $\times$ 1000 $\mu$m area (same area as presented in figure 4.4.9) is shown in figure 4.4.11.

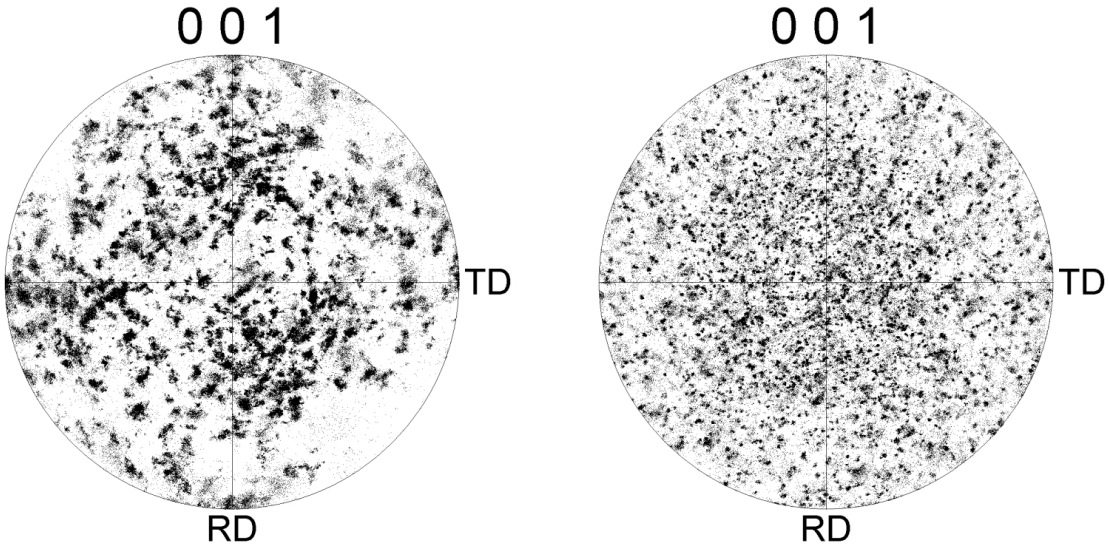


**Figure 4.4.11:** Pole figure plots from an EBSD scan of the 1000 $\mu$m $\times$ 1000 $\mu$m area given in figure 4.4.9 of the forged sample of a cross-section scan. The plot of ferrite and austenite is to the left and right, respectively.

### Longitudinal direction

The images that follow are from areas corresponding to the longitudinal direction of the HISC samples, oriented with the longitudinal direction of the forging horizontally and the thickness direction vertically. This configuration also applies to the pole figure plots. Phase maps from scans of small and large areas are presented in figure 4.4.12 and figure 4.4.13, respectively.

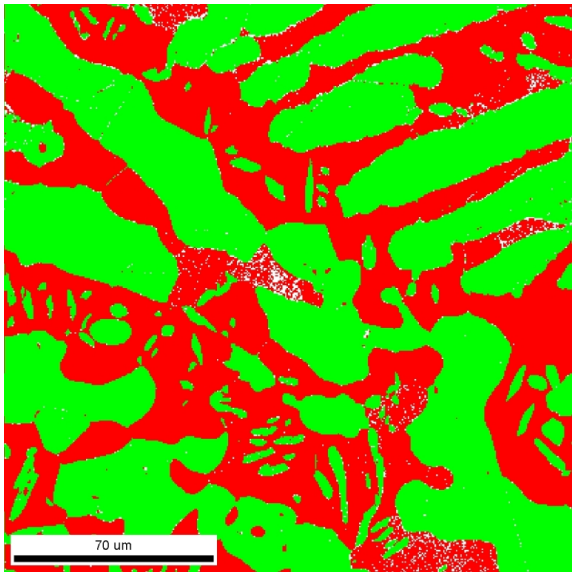


**Figure 4.4.12:** The image shows the phase map of an EBSD scan of a 200 $\mu$m $\times$ 200 $\mu$m area of the forged sample from a longitudinal scan. Green is austenite and red is ferrite.

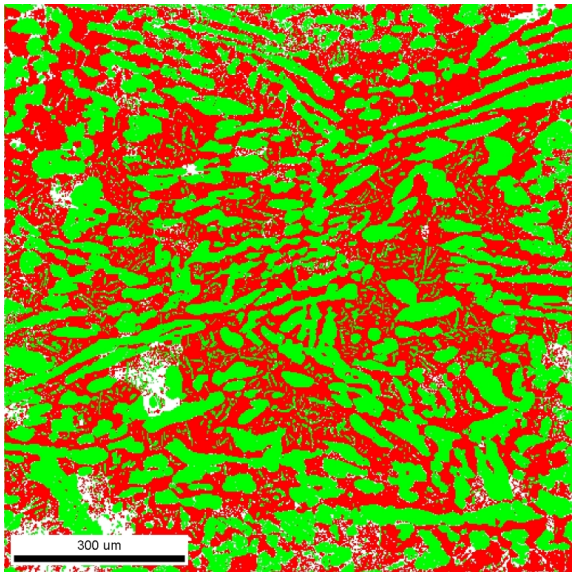


**Figure 4.4.13:** The image shows the phase map of an EBSD scan of a 1000 $\mu$m $\times$ 1000 $\mu$m area of the forged sample from a longitudinal scan. Green is austenite and red is ferrite.

The inverse pole figure (IPF) maps from the same area as seen in figure 4.4.12 is given in figure 4.4.14 for both phases and for each phase separately in figure 4.4.15.

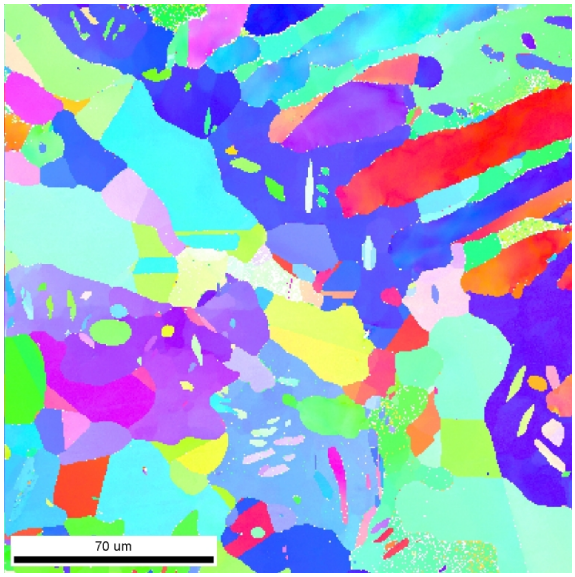


**Figure 4.4.14:** The image shows the IPF map of an EBSD scan of a 200 $\mu$m $\times$ 200 $\mu$m area of the forged sample from a longitudinal scan.

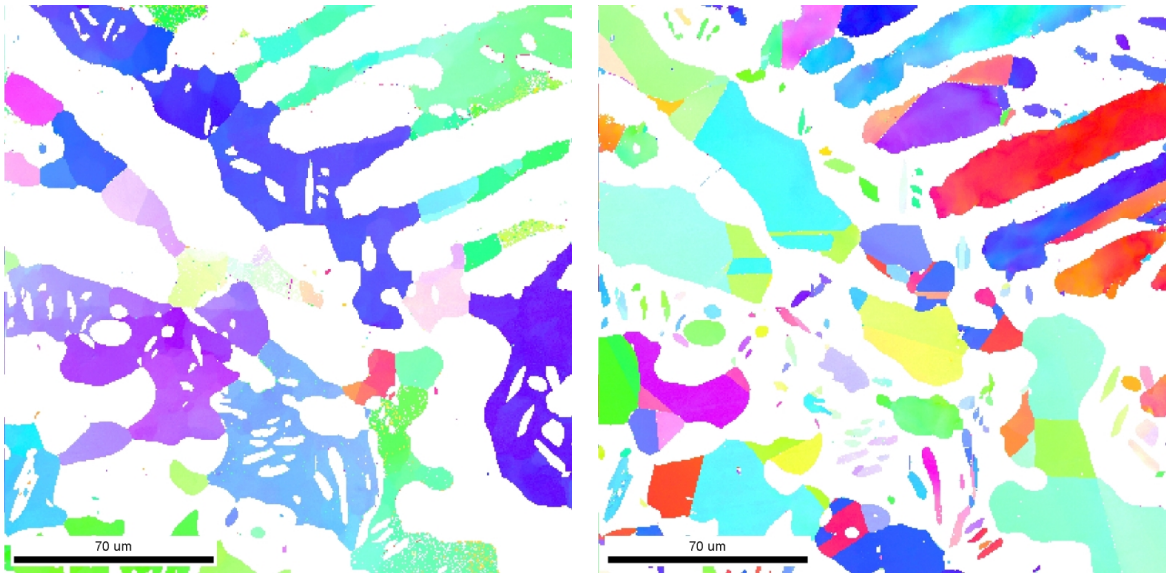


**Figure 4.4.15:** The images show the IPF maps of the EBSD scan in figure 4.4.14 for the ferrite and austenite phase separately to the left and right, respectively.

The inverse pole figure (IPF) maps from the same area as seen in figure 4.4.13 is given in figure 4.4.16 for both phases and for each phase separately in figure 4.4.17.

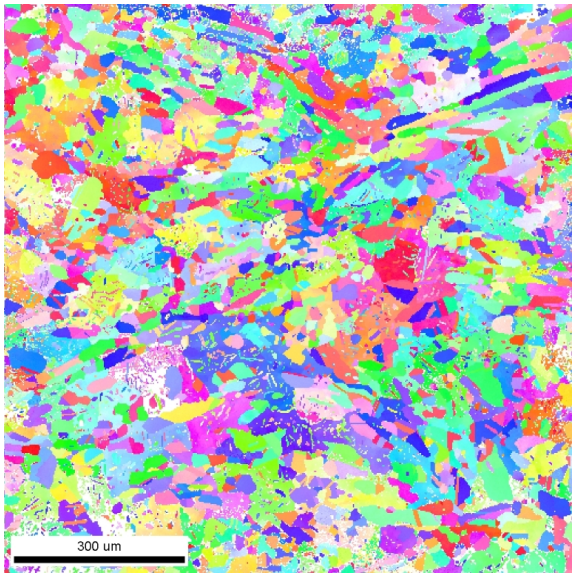


**Figure 4.4.16:** The image shows the IPF map of an EBSD scan of a 1000 $\mu$m $\times$ 1000 $\mu$m area of the forged sample from a longitudinal scan.

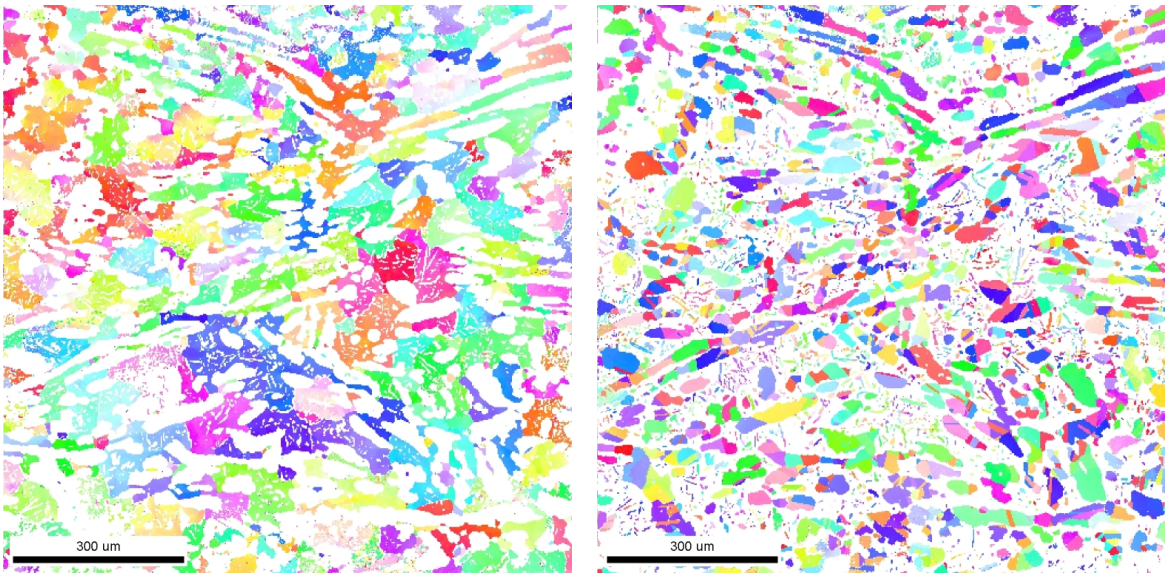


**Figure 4.4.17:** The images show the IPF maps of the EBSD scan in figure 4.4.16 for the ferrite and austenite phase separately to the left and right, respectively.

The pole figure plots from each phase of the scan of 1000 $\mu$m $\times$ 1000 $\mu$m area (same area as presented in figure 4.4.16) is shown in figure 4.4.18.

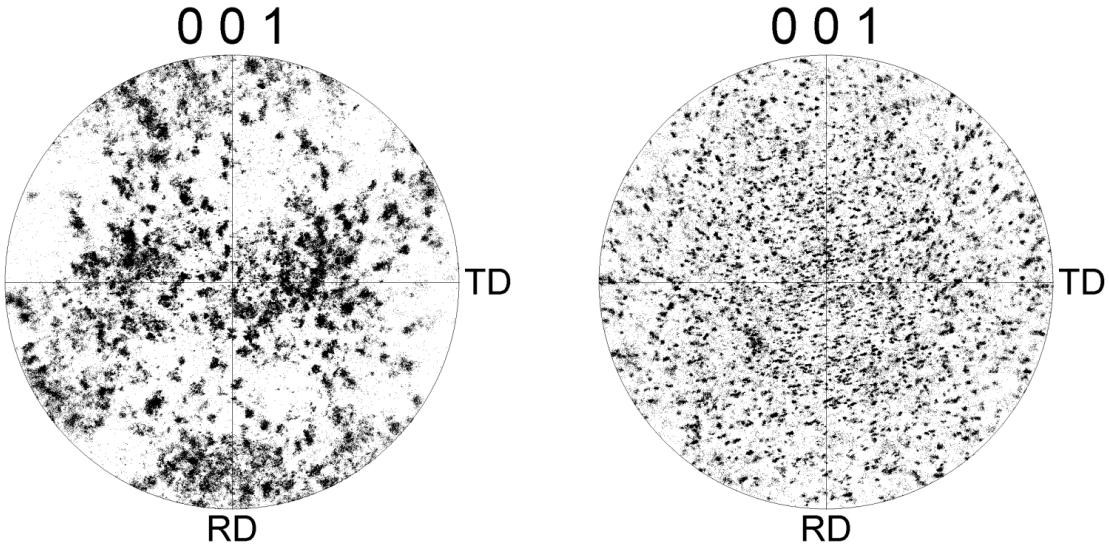


**Figure 4.4.18:** Pole figure plots from a EBSD scan of the 1000 $\mu$m $\times$ 1000 $\mu$m area given in figure 4.4.16 of the forged sample from a longitudinal scan. The plot of ferrite and austenite is to the left and right, respectively.

### Rotation of viewpoint for IPF maps

The IPF maps of ferrite phase separately for the forged material show that the grains of ferrite are in the order of 100 $\mu$m in the longer direction. To confirm that the areas of one color represent single grains, the perspective from which the area is depicted was rotated for the scans of the cross-section. The result of this analysis is shown in figure 4.4.19 and 4.4.20 for the small and large scans, respectively. The austenite phase is blacked out.

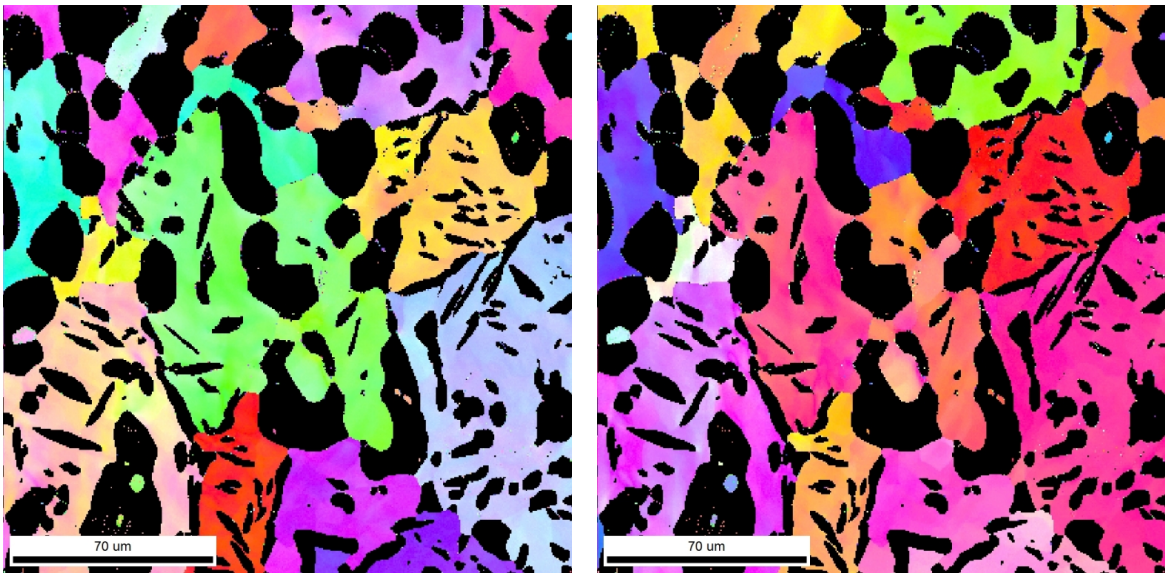


**Figure 4.4.19:** The images shows the IPF map for the ferrite phase only for the same 200 $\mu$m $\times$ 200 $\mu$m area of forged material as shown in figure 4.4.7 both as show before (to the left) and rotated (to the right). The austenite phase is black.

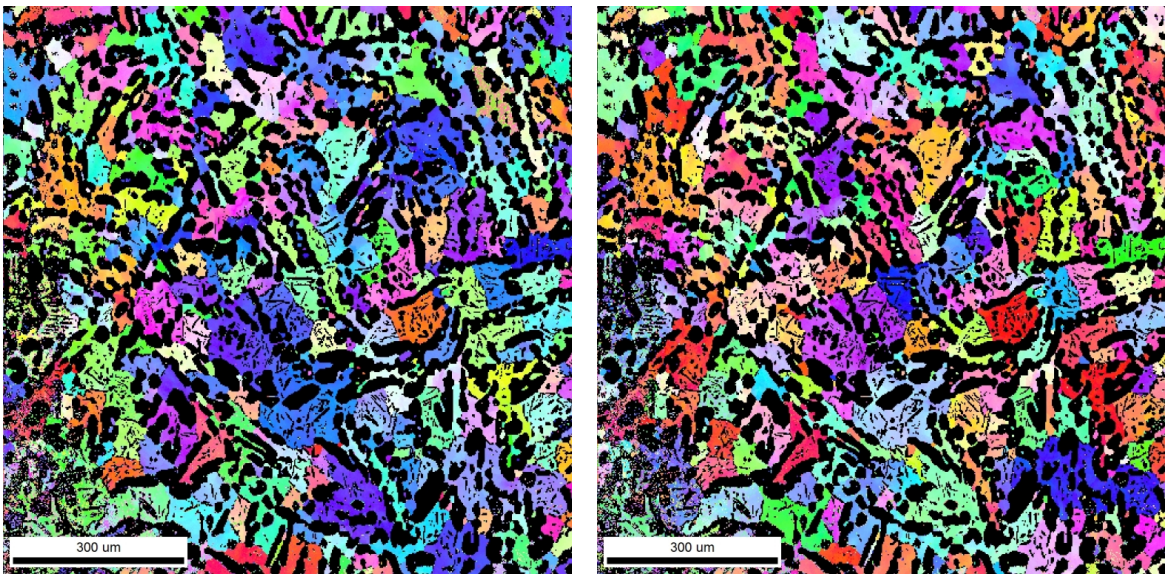


**Figure 4.4.20:** The images shows the IPF map for the ferrite phase only for the same 1000 $\mu$m $\times$ 1000 $\mu$m area of forged material as shown in figure 4.4.9 both as show before (to the left) and rotated (to the right). The austenite phase is black.

# Chapter 5

# Discussion

## 5.1 Microstructure

The results from the EBSD scans show a clear difference between the HIP material and the forged material. Based on the scans done in this work, the following observations are made. The HIP material consists of approximately equal amounts of ferrite and austenite and the phases are evenly distributed in random order. Based on both IPF maps and pole figure plots, the grain orientation of both the ferrite and austenite phase appear random for scans of 200 $\mu$m $\times$ 200 $\mu$m areas.

The forged material consists of a significantly coarser microstructure where the size of the grains varies. The forged material also consists of approximately equal amounts of ferrite and austenite where the austenite grains are embedded in a matrix of ferrite. The IPF maps of the phases separately show that the austenite grains are positioned both inside larger ferrite grains and along the grain boundaries. The larger ferrite grains appears to be on the order of 100 $\mu$m in the longer direction. These observations were verified by rotating the viewpoint of the IPF maps. The pole figure plots show that some directions are represented more than others in the ferrite phase. It is, however, difficult to evaluate the degree of texture in the material as the ferrite grains are large and each grain therefore give clusters in the pole figure plots. Comparisons of scans of the cross-section of the HISC sample and of the longitudinal direction of the forging along one axis were done. These scans showed that some of the grains were elongated in the direction of the forging, but elongated grains are seen in other directions in the scans of the cross-section as well.

Further work can be conducted on EBSD characterization on both materials. In this regard, comparison of microstructure through the thickness of the materials would be interesting. Also, scans of larger areas (or assembling of multiple scans) of the forged material could reveal texture in the material.

## 5.2 Tensile testing

The tensile tests conducted in this work gave consistent results for strength with a maximum difference in yield strength between parallels of 14 MPa (for the two HIP tests). The large elongation of both materials were demonstrated, with more than 35% elongation for the HIP material and 41% for the forged material. The tensile strength to yield ratio was more than 133% for the HIP material and more than 132% for the forged material. These ratio can be considered as baseline values against which the HISC results can be compared to.

## 5.3 Evaluation of HISC testing

Before reviewing and evaluating the HISC results, it is necessary to clarify and discuss a few subjects regarding the testing. For the most part, the test procedure was performed without interruption. The high hydrogen measurements of the HIP material indicate that the incidents involving maintenance during pre-charging had negligible effect on the overall results.

#### Low temperature creep

The only real difficulty during operation of the Cortest proof rings was the relaxation of the rings. This in turn made it difficult to distinguish between low-temperature creep and error in measurements. Because of this challenge, it was decided to use the outer ring diameter after the constant load step (2) as baseline value for further loading. The load *increments* would thereby be correct and, all though the load was less than scheduled during step 3, the actual load at fracture/no-fracture could easily be calculated with the ring diameter before and after fracture.
As explained in the "Results" chapter, the observation of apparent relaxation of ring deflection continued after step 2 and was observed from one day to the next. Because it is known from literature that SDSS material is prone to low temperature creep[2, 19], these observations made it clear that the effects seen came from low temperature creep. The deviation in outer diameter measured on the one notched HIP sample after step 2 remained constant during step 3. This deviation is therefore likely to be the result of inaccuracy in measurement before and after the 10 days of step 2. This means that low temperature creep was only seen in smooth samples when the incrementally increasing load was applied. In order to keep interpretation of the results conservative, the no-fracture values correspond to the measured ring deflection *after* one day, i.e. after low temperature creep for the relevant samples. The fracture values were derived from last measured ring

deflection before fracture, i.e. before possible low temperature creep.

### Conversion charts vs. load cell

To confirm the results derived from the conversion charts from Cortest, a load cell was employed by using the ring deflection to find the load at no-fracture and fracture. It became clear that the values derived from the conversion charts were consistently lower than the values measured with load cell. This was attributed that the conversion charts came from the supplier and must therefore have been calibrated maybe 20 years ago. This factor make them not as reliable at the time of this project (2013) as at acquisition (1995 and 1993) since the equipment can have been used (loaded and unloaded) several times since then. Another possibility is that the conversion charts are intentionally calibrated to yield conservative values. The load cell is relatively modern, and steps were taken for conservative use. The operation of it is already described, but it is pointed out that three measurements were made for each value and the *lower* measurement was presented. For these reasons, it was decided to use the values from the load cell for further analysis.

### Proof ring 3111

From the execution of the experiment, it was remarked that Cortest proof ring 3111 was significantly harder to load than the other rings. Adding extra grease before the second round of testing did not improve the situation. After reviewing the results, it was clear that the fracture and no-fracure stress on both samples that came from this proof ring were significantly lower than the other 4 notched samples of the same material. This is seen with the following numbers from the load cell measurements.

- The average fracture value for the forged notched samples without sample F8 was 117.3% with standard deviation (SD) = 2.4%. Fracture value of sample F8 was 106.0%, almost 5 $\times$ SD less than the others.

- The average fracture value for the HIP notched samples without sample H8 was 121.8% with SD = 1.3%. Fracture value of sample H8 was 101.8%, more than 15 $\times$ SD less than the others.

It is also observed that the result itself from ring 3111 contradict the overall result from the other rings. That is, the fracture and no-fracture values for the forged sample are higher than for the HIP sample. This is the opposite of the general trend, as is discussed later. For these reasons, further analysis was carried out both with and without the data from ring 3111.

## 5.4 Review of HISC results

When comparing the no-fracture and fracture values of the two materials, all average numbers are higher for the HIP material than for the forged material. It is clear from this observation that the HIP material withstood higher stresses (compared to yield stress) than the forged material during the HISC testing. Regarding the notched samples, the difference between with and without data from proof ring 3111 is significant both for average stress values and for the standard deviations.

When comparing the results from smooth with notched samples, two aspects are worth noticing. The first is the difference between the no-fracture and fracture values, which is more than 10% of yield stress for the smooth samples and about 4% for the notched samples. This is because of relaxation in ring deflection (due to low temperature creep) with the smooth samples before the no-fracture values were measured. Because no corresponding ring relaxation was observed for the notched samples, the gap from no-fracture to fracture values is smaller and deviates negligible from the scheduled load intervals. The other aspect is that the standard deviations are consistently higher for the smooth samples than for the notched samples (without data from ring 3111).

The average values at fracture and no-fracture imply higher resistance to cracking for the HIP material in terms of stress. It is, however, not clear from these numbers what the difference in resistance would correspond to in terms of strain. During the testing it was remarked that the samples of HIP material required larger motion with the fastening wrench to achieve the ring deflection for the next stress increment than the samples of forged material. This observation implies that more strain corresponded to the stress increments in the final stages of the loading for the HIP material. The relation between stress and strain for the material is seen in the curves in figure 4.1.1. From these stress-strain curves it is evident that the strain each load increment correspond to increases with increasing stress. To comment further on these observations, the stress values were converted to strain values by interpolation of the points on the stress-strain curves. When comparing all average strain values in table 4.2.4, the big difference between the materials is seen. The fracture and no-fracture values of the HIP material were from 1.8 to 2.0 (except for the smooth no-fracture value which was 2.5) times the values for the samples of forged material. However, it is also evident that the equipment is not meant for strain-adjusted load as the standard deviations are on the order of the strain values themselves. It is therefore questionable whether these data can be used quantitatively. In any regards, the strain values indicate a significantly higher resistance to cracking for the HIP material than the forged material.

## 5.5 Post-fracture analysis

### 5.5.1 Hydrogen measurements

The hydrogen measurements showed that the forged material contained more than twice the amount of hydrogen in the corresponding HIP samples. Only four measurements were done, but the accuracy of each measurement was 0.001 ppm[47]. In addition, the ratio of hydrogen content between HIP and forged material was remarkably similar with ratios of 2.191 for the smooth samples and 2.192 for the notched samples. The measurements were done on fractures samples after completed HISC testing. It is therefore not possible to determine the relative effects of pre-charging and dynamic charging. The findings of Lauvstad et. al. [6] indicated higher hydrogen uptake in forged material than HIP material during pre-charging at room temperature. The results in the present study is consistent with these findings even though the hydrogen content was much higher than in the publication[6]. This can be attributed higher hydrogen diffusion rate at the elevated temperature since diffusion increases with temperature according to Arrhenius equation (equation 2.3). The higher amount of hydrogen in the coarse grained material is also in agreement with theory regarding hydrogen diffusion in SDSS. Since the diffusion mainly takes place in the ferrite phase, the shape and size of the austenite islands are is important due to both length of ferrite "paths" and presence of hydrogen trap cites at austenite grain boundaries[27, 9]. The microstructure of the forged material in this study has larger austenite spacing than the HIP material (51.5 $\mu$m vs. 12.9 $\mu$m) and the phase maps from the EBSD scans indicate that the free diffusion paths in the ferrite phase is longer in the forged material. It can of course not be excluded that the incident of thermal shrink tubing material deposited on the surface could have an effect on hydrogen development and/or diffusion. This is, however, considered unlikely since the deposited material on the samples was removed.

The hydrogen measurements showed significantly less hydrogen in the notched samples than in the smooth samples from both materials. Again, the ratio between notched and smooth samples when comparing the HIP samples and the forged samples was very similar with a smooth/notched sample ratio of hydrogen content of 1.451 for both materials. One possible explanation for this involves diffusion rate related to stress. When a notched sample and a smooth sample is subjected to the same stress in the cross-section of the most narrow area, the entire length of the narrow region of the smooth sample is subjected to approximately the same stress level. The stress applied to the notched sample is derived from the cross-section in the notch (from a diameter of 0.5 mm less than the smooth samples), and so the narrow region outside the notch would be subjected to lower stress. It was pointed out in literature that hydrogen diffuse to the area of higher hydrostatic

stress [9]. It is therefore possible that the higher stress in the smooth samples increased the hydrogen diffusion. Since this hypothesis involves applied stress, it could be tested by hydrogen measurements on similar samples after pre-charging without applied stress. This sort of testing could also give indications to the relative effects of pre-charging and dynamic charging during HISC testing.

### 5.5.2 Fractography

The fracture surfaces were described as a part of the results. The samples from the tensile testing are recognized as ductile fracture for different reasons. Macroscopically, necking before final fracture is evident and also seen in the stress-strain curves as the graphs drop after UTS. The HIP sample shows a typical cup-and-cone fracture consistent with theory. Traces of this are also seen on the forged sample, but less pronounced. The images from the SEM showed dimpled structure on the entire fracture surface for both materials.
The fracture surfaces from the HISC testing were very different from the samples from tensile testing. The main difference between the HIP and the forged samples were the presence of a clear difference in fracture surface related to distance from sample surface during testing. The fracture surfaces on the samples from the HIP material had an outer region which were not dimpled and consisted mainly of multifaceted surfaces. It is difficult to determine whether the features on these flat surfaces can be regarded as river patterns but the absence of a unison dimpled surface indicated a more brittle fracture than from the tensile testing. The middle part on the HIP samples was dimpled and indicated ductile fracture. From these observations it is quite possible that multiple fracture mechanisms have been in action varying with distance from the surface during testing. The transition zone between the outer and inner areas was particularly interesting as a mixture of the two surface characteristics appeared. It was hypothesized that fracture of the austenitic phase in these areas was more ductile and would give dimpled structure while the ferrite was more prone to brittle cracking and gave rise to the flat areas. To comment on this possibility, EDS analysis was carried out on three of each of the characteristic areas. As was noted in the theory chapter, chromium is a ferrite stabilizing element[16]. It is therefore assumed that the concentration of chromium is higher in the ferritic phase. By this theory, areas of higher chromium content would indicate ferrite grains. The results obtained with EDS analysis in this work are not reliable for more than one reason. The EDS technique requires a flat surface with homogeneous microstructure (preferably from a single spot) to get quantitative results. The surface in this case was rough and the areas analyzed were on the order of the grain size. One can therefore not assume that the entire area is homogeneous. All though the results indicated more chromium in the flat areas than in the dimpled areas, it is assumed that the difference is within the margins of error.

It has been pointed out in previous work that the austenite grains fracture in a more ductile manner than the ferrite[27], and another procedure could give more accurate results. One way would be to use EBSD scanning to find representative areas of each phase and then do EDS analysis there. This would give a frame of reference to compare EDS on rough surface to. It would in that scenario also require more scans than the amount done here.
On the forged samples, the same features could be seen in the middle of the surface as in the outer part. This was mainly flat surfaces with similarities to the outer region on the HIP samples. There were, however, areas of dimpled structure both as large areas and in between the flat surfaces. The large areas were not consistently located in the middle of the surface but could appear near the outer surface while the middle was more flat. This indicates a mixture of fracture modes as on the HIP material, but not in the same way related to distance from surface during testing. It is also noted that the texture on the forged material is coarser than the HIP material. This could be related to the coarser microstructure of the forged material.

## 5.6 Overall HISC results

The primary goal of this project was to reveal and compare the susceptibility to HISC for the HIP and forged material. For the HIP material the UTS/YS ratio from the tensile testing and the average fracture stress/YS of smooth samples from the HISC testing were 133% and 123%, respectively. The similar comparison for the forged material is 132% and 117% from tensile and HISC tests, respectively. On the basis of this reduced fracture strength, the high hydrogen content in the fractured samples and change of fracture mechanism observed in the SEM, it is clear that the samples of both HIP and forged material has been exposed to HISC. From the comparison of materials, it is clear that the HIP samples endured higher stresses before fracture and is more resistant against HISC than forged material. The comparison of austenite spacing and fracture values in figure 4.2.3 and figure 4.2.4 showed that the material with smallest austenite spacing (HIP material) endured higher stresses prior to HISC. This is in agreement with litterature[4] as seen in figure 2.4.3.
Observations during testing gave indications of more strain in the HIP samples than in the forged samples. This was verified when the stress results were converted to strain values. The average strain at fracture for smooth samples was 6.2% and 3.3% for HIP and forged samples, respectively. Corresponding values from notched samples (without data from ring 3111) were 6.0% and 3.4% for HIP and forged samples, respectively. These values were followed by very large standard deviations due to the conversion from stress to strain and should therefore not be evaluated qualitatively. They do, however, give indications

of what amount of strain could be used for further HISC testing with strain as variable. These values also clearly show the reduced ductility when comparing with the elongation from the tensile tests of more than 35% and 41% for HIP and forged samples, respectively.

The loss of ductility was reflected on the fractured samples with both the absence of a clear necking and the change in features on the fracture surfaces. These where completely covered with dimples on the tensile samples, a feature which was reduced to smaller areas on the HISC samples. In their place, other features appeared and dominated in areas. The classification of these surfaces is less straight forward, but is characterized by flat structure with lines running over the surface. The observed lines were in some areas side by side, while in others fanned out and could be described as the river patterns indicating brittle cleavage fracture as described in literature[23]. On the HIP samples the not dimpled surface was restricted to an outer ring of the samples, while dimpled structure was dominant in the center. The forged material showed similar features on the fracture surface in the center as near the edge indicating that the fracture mechanism is not related to distance from surface. Since the change in fracture mode is attributed the presence of hydrogen, it follows that it is likely that hydrogen has diffused into the center of the forged samples. In these regards, the difference in hydrogen content is very interesting. The HIP material contained less than half the hydrogen in the forged material. As explained above, this is likely to be caused by a lower diffusion rate through the HIP material because of more tortuous paths for the hydrogen. The clear difference of features in relation to distance from surface on the fracture surface of HIP samples coincides with the hydrogen measurements. This makes it likely that the change in fracture mode is due to the depth of hydrogen diffusion. It is quite possible that the hydrogen content was high enough in this outer area to give macroscopically brittle fracture, leading to an overload of the remaining center which eventually failed by ductile fracture. These observations indicated slower diffusion in the HIP material than in the forged material, which again is related to the microstructural differences described in the beginning of this chapter.

The difference in stress at fracture between smooth samples and notched samples is negligible. The only real difference found in the fracture surface examination was the higher degree of roughness in the smooth samples. Cracks had initiated along the surface of the smooth samples, as seen in figure 4.3.15 and figure 4.3.31. This gives rise to multiple initiation points before final fracture which in turn give more texture on the fracture surface. Any difference in depth from surface of transition from outer to inner fracture zone (on HIP samples) was not measurable. The difference in hydrogen content between smooth and notched samples was discussed above, but in regards to the HISC results no corresponding difference in HISC susceptibility is seen. On the other hand, a significant upside to the use of notched samples appeared. This is in relation to the low temperature

creep experienced during testing. The relaxation of ring deflection was only experienced on smooth samples and not on the notched samples. This means that the interval between no-fracture and fracture value is far less for notched samples, giving more precise indications of threshold values for HISC susceptibility. This could be explained by the relation between elongation caused by creep and the length of the narrowest cross-section. On the smooth samples the 25.4 mm of narrow section is exposed to (quite) similar stress and is therefore equally prone to creep. The smooth area on the notched samples was exposed to lower stress and is therefore less likely to creep. Creep within the notch would result in very little elongation lengthwise, and does therefore not give the same degree of relaxation of ring deflection.

### 5.6.1 Comparison to previous testing and requirements in DNV-RP-F112

In the literature reviewed for this work, several methods for testing were used. In regards to the tests carried out in this work, the results from the JIP regarding incrementally increasing loads are important. They found that testing by stepwise loading gave similar critical loads as testing by direct loading[36].

There are two other aspects which must be kept in mind when reviewing the results from this work in context of previous testing. One is that the test equipment used here did not exert constant load completely at the higher stresses since the ring deflection relaxed when low temperature creep occurred. This happened only on smooth samples and one can therefore evaluate whether the "No-fracture" results from the notched samples can be considered representative. Similar fracture surfaces were observed on these samples as on the smooth samples with the exception of cracking along the sides. The hydrogen content was also lower in the notched than the smooth samples, but the "Fracture" results were at similar load levels. The other aspect is that this testing did not measure crack initiation load level as published by others[4]. It is, however, not clear from literature whether the presence of microcracks should be regarded as critical events as they may arrest in austenite[28]. One can therefore consider if there is a critical crack size one can use for evaluating HISC. If the crack arrests in one of the first few austenite grains it encounters, an alternative could be to relate critical crack size to austenite spacing. To comment further on such an approach, long term testing followed by analysis of surface cracks could give indications on reliability of cracks arresting in austenite. The intention of presenting the no-fracture values in this work was to give more conservative values than the fracture values regarding threshold for HISC. It is, however, not proven in this work that the material would withstand the no-fracture stresses over longer times.

The results from the present study show that both forged and HIP SDSS is prone to HISC. All though some dispute in literature[7, 29], these findings are in agreement with the majority of literature reviewed. The results also indicated a higher resistance against HISC in HIP material than forged material, as found by others [6, 5] and reflected in DNV-RP-F112[3]. The allowable stresses presented in DNV-RP-F112 relates to membrane and bending stress, but the relation of the results found in this work and the different types of stress in DNV-RP-F112 is beyond the scope of the current discussion. The membrane stress allowed in the design duideline is 80% and 68% of SMYS for HIP and forged material, respectively. The design guideline allows for different stress with and without stress raisers present for the membrane + bending stress. These requirements from the recommended practice is compared to the results obtained in this study in table 5.6.1 below. Here, the membrane + bending stress data is given with and without stress raiser along with no-fracture results achieved in this study with the load cell (without data from ring 3111 on for the notched samples). The results from the notched samples in this study are listed with the data for stress raiser present in DNV-RP-F112.

**Table 5.6.1:** The table shows the requirements is design guideline DNV-RP-F112 [3] with the results obtained in this study. The latter is the no-fracture values from the load cell without the data from ring 3111. The numbers from DNV-RP-F112 are membrane + bending stress related to SMYS while the numbers from this study relates to yield strength from the tensile testing.

| | Forged SDSS | | HIP SDSS | |
|---|---|---|---|---|
| | Notched/ stress raiser | Smooth | Notched/ stress raiser | Smooth |
| DNV-RP-F112 | 76.5 % | 90 % | 90 % | 100 % |
| Results in this study | 113.8% $\pm$ 2.2% | 104.8% $\pm$ 3.1% | 117.1% $\pm$ 2.2% | 112.6% $\pm$ 3.9% |

## 5.6.2 Further work

Suggestions to further work have been given throughout this chapter regarding the individual parts of this project. Some more general considerations are given here.

To verify the HISC results found in this work, constant load testing with longer duration can be done based on the no-fracture values presented above. The equipment used in this work can also be used for this purpose, and a possibility is to counteract low temperature creep by readjusting ring deflection (especially short after loading). The results found here also indicate high strain in the materials (especially HIP material) which can be investigated further with equipment which have strain as input parameter and/or by using extensometer during constant load testing. Furthermore, the hydrogen measurements give rise to further work on the relative effects of pre-charging and dynamic charging as ex-

plained above. Previous work [30] has shown that hydrogen content affects the degree of embrittlement. Both the fracture surface examination and the hydrogen content indicated that the HIP samples in this work were not as affected by hydrogen in the center of the sample as at the surface. In this regard, one possibility for for further HISC testing on HIP material is to explore the influence of higher hydrogen content than in this work.
Finally, only two materials have been tested in this work and other SDSS materials can be tested in a similar manner. Some interesting possibilities in these regards come with other production methods (giving material with other austenite spacing) or welded parts and HAZ. Results from materials with other austenite spacing would be very interesting to compare with figure 4.2.3 and figure 4.2.4 in this thesis.

# Chapter 6

# Concluding remarks

Testing by stepwise increasing loads to find susceptibility to HISC has been conducted with both notched and smooth samples from two SDSS materials. Afterwards, the fracture surfaces were analyzed and the hydrogen contents were measured. The microstructures were examined by the EBSD technique.

Both materials were exposed to HISC, but the HIP material showed a higher threshold in terms of stress and strain than the forged material. The EBSD analysis showed a finer and more random microstructure in the HIP material than in the forged material. This has probably influenced hydrogen diffusion as the forged material contained more than twice the amount of hydrogen found in the HIP material. These factors has likely affected the fracture mechanism as well, since the fracture surfaces on samples of HIP material indicated ductile fracture in the center while the forged samples was more brittle over the whole cross-section.

The notched samples contained less hydrogen than the smooth samples, but fractured at quite similar loads. Low temperature creep was experienced on the smooth samples, making the final load increment before fracture larger than intended. The last loads sustained without fracture were therefore 104.8% $\pm$ 3.1% and 112.6% $\pm$ 3.9% of yield strength for forged and HIP material, respectively. Since the notched samples did not creep noticeably, the corresponding loads were higher with 113.8% $\pm$ 2.2% and 117.1% $\pm$ 2.2% of the yield strength for forged and HIP material, respectively.

# List of symbols

| Symbol | Name/meaning |
|---|---|
| $\alpha$ | ferrite |
| $\gamma$ | austenite |
| I | current |
| E | electrical potential |
| $A_0$ | initial area of most narrow cross-section |
| r | radius |
| F | force |
| $\sigma$ | stress |
| $\epsilon$ | strain |
| $\Delta$D | ring deflection |
| g | gravitational acceleration constant |
| | From DNV-RP-F112 |
| $\alpha_m$ | constant for membrane stress |
| $\alpha_{m+b}$ | constant for membrane + bending stress |
| $\gamma_{HISC}$ | material quality parameter |
| $\sigma_m$ | membrane stress |
| $\sigma_{m+b}$ | membrane + bending stress |
| $L_{res}$ | length of residual strain area |
| $\epsilon_{res}$ | residual strain |
| | Diffusion related |
| $E_A$ | activation energy |
| T | temperature |
| D | diffusion rate |
| R | gas constant |

# Bibliography


[1] M-630. Technical report, NORSOK.

[2] T. Taylor, T. Pendlington, and R. Bird. Foinaven super duplex materials cracking investigation. In Offshore Technology Conference, 1999.

[3] DNV-RP-F112. Technical report, Det Norske Veritaes.

[4] P. Woollin and A. Gregori. Avoiding hydrogen embrittlement stress cracking of ferritic austenitic stainless steels under cathodic protection. ASME, 2004.

[5] G. Ø. Lauvstad, R. Johnsen, M. Bjurström, C.-G. Hjort, and B. Nyhus. Improved resistance towards hydrogen induced stress cracking (HISC) of hot isostatically pressed (HIP) duplex stainless steels under cathodic protection. In NACE International Corrosion Conference.

[6] G. Ø. Lauvstad, R. Johnsen, I. Asbjørnsen, and C.-G. Hjort. Resistance towards hydrogen-induced stress cracking of hot isostatically pressed duplex stainless steels under cathodic protection. Corrosion, 66(11):1150041–11500413, 2010.

[7] C.-G. Hjorth. HIP powder metal near-net shapes for demanding environment and applications. Journal of Iron and Steel Research, International, 14(5, Supplement 1):121 – 125, 2007.

[8] R. Johnsen. HISC of duplex stainless steel in seawater. University Lecture, 2011.

[9] V. Olden, C. Thaulow, and R. Johnsen. Modelling of hydrogen diffusion and hydrogen induced cracking in supermartensitic and duplex stainless steels. Materials & Design, 29(10):1934 – 1948, 2008.

[10] R. Johnsen, B. Nyhus, S. Wästberg, and G. Lauvstad. New improved method for HISC testing of stainless steels under cathodic protection. CORROSION 2007, 2007.

[11] K. Nisancioglu. Corrosion Basics and Engineering.

[12] DNV-RP-B401. Technical report, Det Norske Veritaes.

[13] M-503. Technical report, NORSOK.

[14] E. Lembach-Beylegaard. Hydrogen Transport in Duplex Stainless Steels. Doktor ingeniøravhandling. Universitetet i Trondheim, Norges tekniske høgskole, Institutt for maskinkonstruksjon og materialteknikk, 1996.

[15] J.K. Solberg. Teknologiske Metaller og Legeringer.

[16] H. Bhadeshia and R. Honeycombe. Steels: Microstructure and Properties. Elsevier Science, 2011.

[17] V. Olden, C. Thaulow, R. Johnsen, E. Østby, and T. Berstad. Application of hydrogen influenced cohesive laws in the prediction of hydrogen induced stress cracking in 25%Cr duplex stainless steel. Engineering Fracture Mechanics, 75(8):2333 – 2351, 2008.

[18] W.D. Callister. Materials Science And Engineering: An Introduction. John Wiley & Sons, 2007.

[19] U. Kivisäkk. Relation of room temperature creep and microhardness to microstructure and HISC. Materials Science and Engineering: A, 527(29–30):7684 – 7688, 2010.

[20] Sandvik. Company webpage, April 2013.

[21] BodyCote. Company webpage, April 2013.

[22] A. M. Elhoud, N.C. Renton, and W.F Deans. Hydrogen embrittlement of super duplex stainless steel in acid solution. International Journal of Hydrogen Energy, 35(12):6455–6464, 2010.

[23] T. L. Anderson. Fracture Mechanics: Fundamentals and Applications. Bienal de Arquitectura Española, 2005.

[24] J.E.I Metallurgical Inc. Company webpage, May 2013.

[25] Vanderbilt School of Engineering. University webpage, May 2013.

[26] Argo Tech Materials Laboratory. Company webpage, May 2013.

[27] V. Olden, C. Thaulow, R. Johnsen, E. Østby, and T. Berstad. Influence of hydrogen from cathodic protection on the fracture susceptibility of 25%Cr duplex stainless steel – constant load SENT testing and FE-modelling using hydrogen influenced cohesive zone elements. Engineering Fracture Mechanics, 76(7):827 – 844, 2009.

[28] V. Olden, C. Thaulow, R. Johnsen, and E. Østby. Cohesive zone modeling of hydrogen-induced stress cracking in 25% Cr duplex stainless steel. Scripta Materialia, 57(7):615 – 618, 2007.

[29] U. H. Kivisäkk and M. Holmquist. Influence of cathodic protection on hydrogen embrittlement on annealed and cold worked duplex stainless steels. In Corrosion/2001.

[30] T. Zakroczymski, A. Glowacka, and W. Swiatnicki. Effect of hydrogen concentration on the embrittlement of a duplex stainless steel. Corrosion Science, 47(6):1403 – 1414, 2005.

[31] R. C. Prasad, V. C. Kain, and S. R. Roychowdhury. Environmental effects on the fracture toughness of duplex stainless steel (UNS S31803). CORROSION 2006, 2006.

[32] K. C. Ou and J. K. Wu. Effect of calcareous deposits formation on the hydrogen absorption of steel. Materials Chemistry and Physics, 48(1):52 – 55, 1997.

[33] F. Zucchi, V. Grassi, C. Monticelli, and G. Trabanelli. Hydrogen embrittlement of duplex stainless steel under cathodic protection in acidic artificial sea water in the presence of sulphide ions. Corrosion Science, 48(2):522 – 530, 2006.

[34] I. Asbjørnsen. The effect of microstructure on hydrogen induced stress cracking (HISC) of stainless steels. Technical report, Department of Materials Science and Engineering, NTNU.

[35] A. Mikkelsen, S. Wästberg, R. Johnsen, B. Nyhus, and T. Rogne. Influence of ambient pressure on hydrogen induced stress cracking (HISC) of duplex stainless steels under cathodic protection. In NACE International Corrosion Conference.

[36] B. Nyhus, S. Wästberg, and R. Johnsen. Technical report, SINTEF Materials and Chemistry.

[37] M-WA-01. Technical report, NORSOK.

[38] J. Hjelen. Scanning Elekton-Mikroskopi.

[39] K.Z. Baba-Kishi. Review electron backscatter kikuchi diffraction in the scanning electron microscope for crystallographic analysis. Journal of Materials Science, 37(9):1715–1746, 2002.

[40] Newcastle University Electron Microscopy Service. University webpage.

[41] J. Hjelen. Electron backscatter diffraction (EBSD) in the SEM. University Lecture, 2012.

[42] K. Andersen. EBSD investigations of HAZ of 9% nickel steel. Technical report, Department of Materials Science and Engineering, NTNU.

[43] Technical report.

[44] Technical report.

[45] Technical report.

[46] Cortest Inc. Operation Manual - Cortest Proof Ring and Optional Equipment.

[47] A.-K. Kvernbråten. Test report - hydrogen determination. Technical report, SINTEF Materials and Chemistry.

# Appendices

# Appendix A

# Stress calculations

The calculation of stress ($\sigma$) was with use of equations A.1 and A.2 below. Here, r is radius and $A_0$ is area in most narrow cross section and F is force.

$$A_0 = \pi \times r^2 \tag{A.1}$$

$$\sigma = \frac{F}{A_0} \tag{A.2}$$

The calculations with the conversion chart was based on the a linear relation between ring deflection ($\Delta$ D) and force as given in equation A.3, where a and b are constants.

$$F = a \times \Delta D + b \tag{A.3}$$

The load cell gave load in kg and so the force was calculated with the relation given in equation A.4 where m is mass and g is the gravitational constant 9.81 $\frac{m}{s^2}$.

$$F = m \times g \tag{A.4}$$

## A.1 Example of calculation of ring deflection

The following is an example of calculation of new ring diameter ($D_1$) from initial ring diameter ($D_0$) with the conversion charts from Cortest. The linear relation between ring deflection and load is given in LBS and inches, so the example includes conversion to SI units. The following data was required for calculation of first loading of ring 2622 for sample F1 of forged material.

- Stress, $\sigma$ = 86% $\times$ YS
- YS = 581.300.000 Pa
- Actual sample diameter = 3.80 mm, actual sample radius = 1.90 $\times$ $10^{-3}$ m
- Diameter of proof ring unstressed, $D_0$ = 219.11 mm
- a = 91008.717428
- b = -95.3922842596
- 25.4 mm = 1 inch
- 4.448 N = 1 LBS

Calculation of area, force and ring deflection is given in equations A.5, A.6 and A.7 based on equations A.1, A.2 and A.3, respectively. Calculation of new ring diameter ($D_1$) is given in equation A.8.

$$A_0 = \pi \times (1.90 \times 10^{-3} m)^2 = 1.1341 \times 10^{-5} m^2 \tag{A.5}$$

$$F = \sigma \times A_0 = 86\% \times 581.300.000 Pa \times 1.1341 \times 10^{-5} m^2 = 5669.64N = \frac{5669.64N}{4.448N/LBS} = 1274.65LBS \tag{A.6}$$

$$\Delta D = \frac{F - b}{a} = \frac{1274.65LBS - (-95.3922842596)}{91008.717428} = 0.015053971inch = 0.015053971inch \times 25.4mm/inch = 0.3824mm \tag{A.7}$$

$$D_1 = D_0 - \Delta D = 219.11mm - 0.3824mm = 218.7276 \simeq 218.73mm \tag{A.8}$$

# Appendix B

# Load cell results

The measurements done with the load cell is shown in table B.0.1 for the samples of forged material and in B.0.2 for the samples of HIP material.

**Table B.0.1:** The table shows the measurements with the load cell for samples of forged material for the fracture and no-fracture values.

| | | No-fracture values [kg] | | | | Fracture values [kg] | | | |
|---|---|---|---|---|---|---|---|---|---|
| Sample | Ring | Load measurements | | | Max.-min. | Load measurements | | | Max.-min. |
| Smooth | 2622 | 732 | 725 | 714 | 18 | 802 | 809 | 813 | 11 |
| | 2623 | 719 | 719 | 707 | 12 | 807 | 798 | 793 | 14 |
| | 2628 | 679 | 680 | 690 | 11 | 805 | 818 | 803 | 15 |
| | 2629 | 725 | 721 | 717 | 8 | 757 | 751 | 751 | 6 |
| | 2630 | 747 | 752 | 754 | 7 | 834 | 828 | 848 | 20 |
| Notched | 3109 | 607 | 599 | 594 | 13 | 628 | 617 | 609 | 19 |
| | 3110 | 611 | 619 | 611 | 8 | 637 | 636 | 630 | 7 |
| | 3111 | 546 | 545 | 541 | 5 | 561 | 568 | 560 | 8 |
| | 3112 | 597 | 593 | 596 | 4 | 615 | 614 | 612 | 3 |
| | 3113 | 573 | 570 | 571 | 3 | 596 | 593 | 588 | 8 |

**Table B.0.2:** The table shows the measurements with the load cell for samples of HIP material for the fracture and no-fracture values.

| | | No-fracture values [kg] | | | | Fracture values [kg] | | | |
|---|---|---|---|---|---|---|---|---|---|
| Sample | Ring | Load measurements | | | Max.-min. | Load measurements | | | Max.-min. |
| Smooth | 2622 | 872 | 868 | 883 | 15 | 920 | 916 | 929 | 13 |
| | 2623 | 911 | 895 | 902 | 16 | 1000 | 992 | 991 | 9 |
| | 2628 | 845 | 867 | 867 | 22 | 933 | 958 | 936 | 25 |
| | 2629 | 852 | 835 | 856 | 21 | 964 | 941 | 965 | 24 |
| | 2630 | 823 | 815 | 821 | 8 | 870 | 891 | 877 | 21 |
| Notched | 3109 | 667 | 668 | 663 | 5 | 687 | 692 | 688 | 5 |
| | 3110 | 642 | 642 | 637 | 5 | 669 | 669 | 667 | 2 |
| | 3111 | 561 | 568 | 560 | 8 | 584 | 585 | 580 | 5 |
| | 3112 | 646 | 647 | 646 | 1 | 677 | 681 | 677 | 4 |
| | 3113 | 678 | 688 | 679 | 10 | 699 | 708 | 702 | 9 |

The stress was calculated by use of equations A.1, A.2 and A.4. The stress calculated from the measurements in table B.0.1 and table B.0.2 is shown in table B.0.3 and table B.0.4, respectively.

**Table B.0.3:** The table shows the stress calculations based on the measurements with the load cell for samples of forged material.

| Sample | Ring | Min. load no fracture | Min. load fracture | Actual diameter [mm] | Stress [MPa] No fracture | Stress [MPa] Fracture | % of yield stress No fracture | % of yield stress Fracture |
|---|---|---|---|---|---|---|---|---|
| Smooth | 2622 | 714 | 802 | 3.80 | 617.6 | 693.7 | 106.2 % | 119.3 % |
| | 2623 | 707 | 793 | 3.83 | 602.0 | 675.2 | 103.6 % | 116.2 % |
| | 2628 | 679 | 803 | 3.82 | 581.2 | 687.3 | 100.0 % | 118.2 % |
| | 2629 | 717 | 751 | 3.79 | 623.5 | 653.0 | 107.3 % | 112.3 % |
| | 2630 | 747 | 828 | 3.87 | 623.0 | 690.5 | 107.2 % | 118.8 % |
| Notched | 3109 | 594 | 609 | 3.37 | 653.3 | 669.8 | 112.4 % | 115.2 % |
| | 3110 | 611 | 630 | 3.35 | 680.0 | 701.2 | 117.0 % | 120.6 % |
| | 3111 | 541 | 560 | 3.37 | 595.0 | 615.9 | 102.4 % | 106.0 % |
| | 3112 | 593 | 612 | 3.35 | 660.0 | 681.2 | 113.5 % | 117.2 % |
| | 3113 | 570 | 588 | 3.30 | 653.8 | 674.4 | 112.5 % | 116.0 % |

**Table B.0.4:** The table shows the stress calculations based on the measurements with the load cell for samples of HIP material.

| Sample | Ring | Min. load no fracture | Min. load fracture | Actual diameter [mm] | Stress [MPa] No fracture | Stress [MPa] Fracture | % of yield stress No fracture | % of yield stress Fracture |
|---|---|---|---|---|---|---|---|---|
| Smooth | 2622 | 868 | 916 | 3.81 | 746.9 | 788.2 | 114.3 % | 120.6 % |
| | 2623 | 895 | 991 | 3.82 | 766.1 | 848.3 | 117.3 % | 129.8 % |
| | 2628 | 845 | 933 | 3.76 | 746.6 | 824.3 | 114.3 % | 126.2 % |
| | 2629 | 835 | 941 | 3.82 | 714.7 | 805.5 | 109.4 % | 123.3 % |
| | 2630 | 815 | 870 | 3.80 | 705.0 | 752.5 | 107.9 % | 115.2 % |
| Notched | 3109 | 663 | 687 | 3.28 | 769.7 | 797.6 | 117.8 % | 122.1 % |
| | 3110 | 637 | 667 | 3.24 | 757.9 | 793.6 | 116.0 % | 121.5 % |
| | 3111 | 560 | 580 | 3.30 | 642.3 | 665.2 | 98.3 % | 101.8 % |
| | 3112 | 646 | 677 | 3.28 | 750.0 | 786.0 | 114.8 % | 120.3 % |
| | 3113 | 678 | 699 | 3.29 | 782.4 | 806.6 | 119.8 % | 123.5 % |